Faculty of Engineering, Computing and Mathematical Sciences
SCHOOL OF MECHANICAL ENGINEERING

Performance of Alternative Propellants in an Inductive Electric Propulsion System

Doctoral Thesis

Ashley R. Chadwick

29 May 2017

This page is intentionally left blank.

Contents

Abstract

Spacecraft fitted with electric propulsion systems can achieve a greater final velocity than chemical rockets, thus facilitating a range of new trajectories and exploratory mission capabilities. However, conventional propellants for electric propulsion are largely rare noble gases such as xenon, exhibiting a low natural abundance and requiring expensive manufacturing methods to obtain the necessary quantities. In contrast, alternative propellants are those which exist in abundance both on Earth and at locations of interest within the solar system such as moons, planets, and asteroids. The ability to utilise such resources for propulsion purposes thus provides the opportunity to decrease reliance on Earth as the sole source of propellant in the solar system and execute more flexible, higher reliability operation.

As a result of these benefits, alternative propellants have been investigated in a number of conventional and novel electric propulsion systems. However, the design of these systems, as well as the dissimilarity in chemical properties of conventional and alternative propellants, have often prohibited their implementation following significant demands on increased supply power or the degradation of critical thruster components such as the electrodes. One class of electric propulsion which does not exhibit these restrictions is inductive propulsion. These systems possess the greatest flexibility in propellants, able to operate with chemically reactive species such as O_2 and CO_2 without damage to thruster components.

This thesis reports on the implementation of various alternative propellants (O_2, CO_2, and N_2) in an inductive propulsion system, measuring their thrust and exhaust velocity outputs as well as developing novel techniques to characterise their behaviour using gas-independent properties.

Thrust, specific impulse, and the thrust-to-power ratio were measured for each of the propellants, as well as propellant mixtures combining the molecular species with a

monatomic gas, argon. The purpose of this mixing was to exploit the complimentary chemical properties of the respective species to increase the performance of the system through both the electromagnetic and gasdynamic driving mechanisms. The benefit of altering propellant properties is clear, with these propellant configurations increasing almost all performance metrics of the thruster. Thrust was shown to almost triple for a mixed gas propellant in comparison to single gas propellants at the same input power level. The final thrust values increased by factors of 1.35, 2.70, and 3.86 for O_2, CO_2, and N_2, respectively. This sharp increase in performance is attributed to a transition to discharge regimes of greater coupling efficiency, occurring at lower input powers for mixed propellant conditions. In order to better observe and characterise these transitions, a number of non-intrusive measurement techniques were developed during this project. The first of these techniques was an improved method to assess the inductive coil current, obtaining temporally-resolved information on the discharge including shifts in the coil driving frequency (in response to an increased flow ionisation linked to regime transitions) and the proportion of time spent in both the capacitive and inductive regimes during a single discharge cycle. This latter result revealed information on the stability of the discharge, with mixed propellant configurations staying in the inductive regime for up to 94 % of the cycle, compared to 71 % for the single propellant condition. Additionally, a method was developed and tested to measure the discharge skin depth experimentally, which is a fundamental characteristic of inductive discharges. While measurements of the visible skin depth component were successful, observations of the true skin depth using the magnetic field strength distribution were not. This result yielded information on the axial location of the ionisation region within the discharge tube, taking place at a significant distance from the beginning of the inductive coil. This theory is supported by spatially-resolved measurements of the discharge tube wall temperature. Measurements of the visible skin depth were compared to numerical results, indicating that the two may be reconciled by considering the definition of the visible skin depth and adjusting it to account for electrons not participating in stimulating visible radiation.

These results, combined with an investigation of the impact of discharge chamber wall thickness on chemically dissimilar propellants, provide a comprehensive understanding of the performance of alternative propellants in an inductive electric propulsion system, as well as means through which future thruster designs may be improved and new techniques which can be used to characterise their performance.

Declaration

I certify that this work contains no material which has been accepted for the award of any other degree or diploma in my name in any university or other tertiary institution and, to the best of my knowledge and belief, contains no material previously published or written by another person, except where due reference has been made in the text. In addition, I certify that no part of this work will, in the future, be used in a submission in my name for any other degree or diploma in any university or other tertiary institution without the prior approval of the University of Adelaide and where applicable, any partner institution responsible for the joint award of this degree.

I give consent to this copy of my thesis when deposited in the University Library, being made available for loan and photocopying, subject to the provisions of the Copyright Act 1968.

The author acknowledges that copyright of published works contained within this thesis resides with the copyright holder(s) of those works.

I also give permission for the digital version of my thesis to be made available on the web, via the University's digital research repository, the Library Search and also through web search engines, unless permission has been granted by the University to restrict access for a period of time.

_____ _____

Ashley R. Chadwick Date

Acknowledgements

I have always read the acknowledgement sections of documents like this with some befuddlement, wondering how such a long list of names could be accrued for what at times seems to be an extended, one-way shouting match between the candidate and their computer. However, looking back upon the past few years it is almost painfully obvious how much I have benefited from the support of numerous people to produce the work contained within this thesis, and for that I would like to offer my sincerest gratitude, without reservation or even my usual slew of gibes. Mostly.

First and foremost I'd like to thank my supervisors, without whom this project could have both come to a screeching halt as well as never taking off in the first place. While Bassam Dally came late to the project, he provided the support needed to allow me to continue my studies following the sudden departure of my previous supervisor. That was a particularly worrisome point in my life and I am immeasurably grateful to have been given the opportunity to continue my work and reach this point today. Min Kwan Kim has been my most influential, if not indeed critical, supervisor throughout the project, helping me acclimatise to the world of applied plasma physics and tolerating my many theory and syntax fumbles along the way. I still remember the first time I saw, "Good job," commented in a document I'd written; I read it more than once to make sure it wasn't a spelling mistake. Last but not least is Georg Herdrich, who is the reason I ended up spending these last few years in Germany in the first place. Without Georg I would never have had the opportunities or the freedoms I've enjoyed operating my own test facility, and his particular insight into aerospace research has been invaluable. Each of my supervisors have been a fountain of information and advice, both technical and programmatic, and I can honestly say I could not have come so far without you, so thank you.

Supervisors are, however, only the tip of the iceberg when considering those people who

made this candidature possible. While undoubtedly the instrument of my education, my test setup in the lab in Stuttgart was also (for a proportionately larger period of time) the bane of my existence, and so I can't possibly omit the people who helped me in seemingly daily repairs and refurbishments. Manfred and Olaf were never too busy to help me troubleshoot an electrical problem or indulge an expedition into the depths of the circuitry, though unfortunately they were also never too busy to explain (in inescapable clarity) how a reset button worked when I'd called them with a red herring. Herr Baum, Frank, and Sebastian were also always on hand when it was time to test, and didn't make a fuss when my thruster tried to send kilograms of ice into the vacuum system pumps. Thanks also go to Herr Schneider and the rest of the workshop staff, who suffered through the language barrier with me until we were able to manufacture parts relatively painlessly, as well as my students, each of whom contributed to a particular measurement technique or large-scale overhaul of the setup.

The final group to thank are thus you, my friends and family who helped either directly or indirectly while I muddled my way through, muttering theories and griping to myself. Tomeu, who with Tom gave me my introduction to the horrors of the IPG and on his own helped me with more tests, theories, dis- and re-assemblies, and calamity scavenger hunt than I care to count; Uwe, who was my solace when I wanted to discuss plasma fundamentals, despite our speaking very different languages in every sense of the word; and Adam B, who despite our differences in work ethic put in more hours than anyone else to help me refurbish the facility and get my first experiments. To the rest of you (including but not limited to Fabs, Adam P, Francesco, Yung-An, Mattias, Connie, Tobi, Arne, Martin, Rainer, Stefan, Marcel, and Asim), who either helped me with tests, suffered my German (or tried in vain to improve it), or just generally made my years at IRS something to look back on with fondness, thank you. I can't express how much it's meant to have your support through thick and thin. The same goes for my family, who I've arguably neglected for these past few years to focus on my work. Well, they argue that; I wasn't paying attention.

I'd also be remiss not to thank the University of Adelaide and Sir Ross and Sir Keith Smith Fund for both supplying personal funding over the years, as well as the IRS who provided financial funding for the laboratory equipment and consumables.

For anyone still reading this, I'm officially out of pre-thesis sentiment, so *guten*, I suppose.

List of Nomenclature

A	Area [m^2]
A_{si}	Einstein coefficient of species s [1/s]
B	Outer plasma diameter for skin depth model [m]
b	Inductive coil diameter [m]
C_H	Gauss meter calibration factor
$c_{D,int}$	Internal thruster drag coefficient
c_p	Specific heat capacity (isobaric) [kJ/kg.K]
D	Inductive coil outer diameter [m]
d_{eff}	Tube cooling water channel diameter [m]
E_{ignit}	Discharge inductive ignition energy [kJ]
$E_{RF,\Theta}$	Inductive coil azimuthal electric field strength [V/m]
E_z	Discharge axial electric field strength [V/m]
E_Θ	Discharge azimuthal electric field strength [V/m]
e_{tot}	Discharge specific total energy [kJ/kg]
e_e	Discharge specific electron energy [kJ/kg]
F	Thrust [N]
F_L	Lorentz force [N]
F_{therm}	Force due to thermal expansion of gas [N]
f_{cap}	Characteristic capacitive driving frequency [Hz]
f_{cyc}	Discharge cycle frequency [Hz]
f_{char}	Dominant discharge frequency (at given time in cycle) [Hz]
f_{RF}	Inductive coil driving frequency [Hz]
f_S	Power supply driving frequency [Hz]
$H_{RF,z}$	Inductive coil axial magnetic field strength [T]
H_z	Discharge axial magnetic field strength [T]

H_Θ	Discharge azimuthal magnetic field strength [T]
h_{eff}	Tube cooling water channel height [m]
h_{tot}	Total flow specific enthalpy [kJ/kg]
h_δ	Skin depth specific enthalpy [kJ/kg]
I_{HOKA}	HOKA-measured current [A]
I_{pl}	Plasma current [A]
I_{RF}	Inductive coil current [A]
I_{sp}	Specific impulse [s]
$J_{B,n}$	nth order Bessel function
J_z	Axial current density [A/m^2]
J_Θ	Azimuthal current density [A/m^2]
K	Reaction rate [m^3/s]
L_{pl}	Plasma inductance [H]
L_S	Power source inductance [H]
l	Discharge tube length [m]
l_{coil}	Inductive coil length [m]
l_{eff}	Tube cooling water channel length [m]
$l_{pl,coil}$	Incident plasma-coil length [m]
M	Molecular mass [kg/mol]
m_s	Species mass [kg]
$\dot{m}$	Mass flow rate [kg/s]
$\dot{m}_{cold}$	Propellant cold input mass flow rate [kg/s]
$\dot{m}_{pl}$	Plasma mass flow rate [kg/s]
$\dot{m}_w$	Cooling water mass flow rate [kg/s]
N	Inductive coil number of turns
n_e	Electron number density [m^{-3}]
n_i	Ion number density [m^{-3}]
n_s	Arbitrary species s number density [m^{-3}]
Nu	Nusselt number
P	Electrical input power [kW]
P_A	Power supply anode power [kW]
P_{pl}	Plasma calorimetric thermal power [kW]
P_{RF}	Inductive coil power [kW]
Pr	Prandtl number

p	Pressure [Pa]
$\dot{Q}_{diff,1}$	Thermal power diffused from skin depth (towards tube centre) [kW]
$\dot{Q}_{diff,2}$	Thermal power diffused from skin depth (towards wall) [kW]
$\dot{Q}_H$	Thermal power from inductive coil [kW]
$\dot{Q}_{tube}$	Discharge tube cooling power [kW]
$\dot{Q}_{crit}$	Discharge tube cooling power at failure [kW]
R	Discharge tube inner radius [m]
R_2	Discharge tube outer radius [m]
R_{pl}	Plasma resistance [Ω]
R_S	Power supply resistance [Ω]
R_T	Discharge radius (measured from the thermal boundary layer) [m]
R_2	Discharge tube outer radius [m]
r	Discharge radial position [m]
$r_{L,e}$	Electron cyclotron radius [m]
r_{out}	HET outflow gap [m]
r_{pl}	Plasma radius [m]
Re	Reynolds number
T_e	Electron temperature [eV]
T_{el}	Electronic temperature [eV]
T_{tr}	Translational temperature [K]
T_w	Discharge tube cooling water temperature [K]
T_{wall}	Discharge tube wall temperature [K]
t	Discharge tube wall thickness [m]
t_H	Time at which shift from capacitive frequency is observed [s]
U_A	Power supply anode potential [V]
U_{DL}	Double layer potential [V]
U_{pl}	Plasma potential [V]
U_{RF}	Inductive coil potential [V]
u	Jet velocity [km/s]
$\dot{V}$	Volumetric flow rate [l_n/min]
w_{eff}	Tube cooling water channel width [m]
X_s	Species molar fraction
Z_{pl}	Plasma impedance [Ω]

Z_S	Power supply impedance [Ω]
z	Thruster axial position [m]
α_w	Tube cooling water heat transfer coefficient [W/m^2.K]
δ	Collisional skin depth [m]
δ_{mag}	Magnetic skin depth [m]
δ_T	Thermal boundary layer [m]
δ_{vis}	Visible skin depth [m]
η_F	Thrust efficiency
η_{th}	Total thermal efficiency
$\eta_{th,eff}$	Effective thermal efficiency
κ_{tube}	Discharge tube thermal conductivity [kW/m.K]
κ_w	Cooling water thermal conductivity [kW/m.K]
λ	Mean free path [m]
μ_w	Dynamic viscosity of cooling water [kg/m.s]
σ_{DC}	DC electrical conductivity [S/m]
τ_l	Time-scale of particle traversing thruster [s]
τ_{wall}	Time-scale of particle-wall interactions [s]
υ_{eff}	Effective momentum transfer frequency [Hz]

Physical Constants

g_0	Standard gravity, 9.81 [m/s^2]
m_e	Electron mass, 9.1093$\times 10^{-31}$ [kg]
$\hat{N}$	Avogadro's constant, 6.0221$\times 10^{23}$ [1/mol]
q	Electric charge, 1.6022$\times 10^{-19}$ [C]
$\hat{R}$	Universal gas constant, 8.3143$\times 10^{-3}$ [kJ/mole.K]
μ_0	Permeability of a free space vacuum, $4\pi \times 10^{-7}$ [V.s/m.A]
ϵ_0	Permittivity of a free space vacuum, 8.854$\times 10^{-12}$ [A^2.s^4/kg.m^3]

Acronyms

$ABEP$	Atmosphere-Breathing Electric Propulsion
$ABIP$	Air-Breathing Ion Engine
AC	Alternating Current

ANU	Australian National University
CEA	Chemical Equilibrium with Applications
DC	Direct Current
DL	Double Layer
$ECLSS$	Environmental Control and Life Support System
ESA	European Space Agency
EBB	Elegant Breadboard
EP	Electric propulsion
$FEEP$	Field Emission Electric Propulsion
FFT	Fast Fourier Transform
GIT	Gridded Ion Thruster
$GOCE$	Gravity Field and Ocean Circulation Explorer
$HDLT$	Helicon Double Layer Thruster
HET	Hall Effect Thruster
HHT	Helicon Hall effect Thruster
ICP	Inductively Coupled Plasma
$IEDF$	Ion Energy Distribution Function
IPG	Inductive Plasma Generator
IRS	Institute for Space Systems
$ISRU$	In-Situ Resource Utilisation
ISS	International Space Station
MAI	Moscow Aviation Institute
$MPDT$	Magnetoplasmadynamic Thruster
$NASA$	North American Space Administration
NEO	Near Earth Object
$RAM-EP$	Air-Breathing Electric Propulsion (*common synonym)*
RF	Radio Frequency
$RFEA$	Retarding Field Energy Analyser
RIT	Radio Frequency Ion Thruster
RPT	Radio frequency Plasma Thruster
SF	Self-Field
$VASIMR$	Variable Specific Impulse Magnetoplasma Rocket

List of Figures

List of Tables

This page is intentionally left blank.

Chapter 1

Introduction

Propulsion is arguably the most important subsystem in the context of space operations, not least of all for its facilitation of launching satellites and other spacecraft from Earth into orbit or transit trajectories. However, once removed from a terrestrial environment, a broader variety of propulsion options (than the large liquid or solid chemical systems used to drive launch vehicles) become available, with each suited to a given set of mission objectives or parameters. One extensively-researched, yet still very much developing, branch of propulsion is that of electric propulsion (EP), which uses electrical power (rather than chemical reactions) to produce thrust. This thrust is generated through either the acceleration of charged particles (ions) by electric or magnetic fields, or by heating both charged and neutral particles within the thruster to increase their velocity. The acceleration method depends on the type of EP system utilised, though the use of electrical energy as the driving force allows the velocity of propellant particles leaving an EP thruster to be an order of magnitude greater than those of chemical propulsion systems [1, 2]. This in turn leads to more efficient propellant utilisation and higher final velocity (ΔV) manoeuvres.

Despite such advantages, EP systems are also limited in their application, with major restrictions stemming from the power density of electric sources in space as well as scaling challenges with the propulsion systems themselves. As a result, mission planners must make clear decisions regarding the necessary propulsion system based on the desired trajectory; chemical propulsion systems are better suited towards the transport of heavy spacecraft where time is a critical factor, such as those containing crew or in situations

where a satellite must reach a given orbital altitude within a relatively small time-frame. However, when trajectories are able to be executed over longer periods of time, EP systems may utilise the gradual ejection of high-velocity particles to achieve transport of the payload with a fraction of the necessary propellant. This applies to both cargo transport as well as satellite orbit maintenance. EP is also used to great success for satellite attitude control, where the low power input requirements may be met in-situ and over a long mission lifetime through the use of solar panels.

Most EP systems operate the noble gas xenon due to its low ionisation energy, high mass (resulting in high thrust once accelerated), and inert nature [3]. This yields more thrust than other gases, for the same input energy, which may be gained through electrostatic or electromagnetic acceleration. However, xenon may only be produced by processing air to extract the minute quantities present. This leads to a high production cost (and thus higher mission cost) with relatively low propellant yield, as well as a dependency on Earth-based propellant manufacturing facilities. To address this problem and increase the flexibility of future EP missions, research has been invested into the field of alternative propellants [4–15].

Alternative propellants are broadly defined as those being naturally-occurring in greater quantities than noble gas propellants. These include O_2, N_2, and CO_2, which are widespread not only on Earth, but also at key locations within the solar system such as Mars and Titan [16, 17]. The presence of these gases within the space environment presents the unprecedented opportunity to source and collect propellant within a given mission environment through In-Situ Resource Utilisation (ISRU), removing the reliance on Earth as the central propellant supply point. This in turn grants missions a greater degree of range and flexibility, with the entirety of mission propellant no longer required to be launched from Earth. While technologies for large-scale ISRU are still under development, they remain one of the highest-priority current objectives within the global aerospace sector [18–20] and are expected to play a major part in missions within the coming few decades.

However, such propellants are not necessarily compatible with all EP systems. Many conventional EP systems have experimented with alternative propellants and been met with measured success (as discussed in detail in Chapter 2). Performance is hindered most noticeably in direct-contact EP systems, where the anode-cathode arrangement is exposed to the working fluid and thus suffers rapid and extensive damage when

operating with reactive gases such as oxygen or hydrogen [11–14]. One class of EP system which does not suffer from this limitation is that of Inductive Electric Propulsion (IEP), which utilises an inductive coil separated from the plasma by a dielectric interface to generate a discharge without the possibility of corrosion. Furthermore, IEPs are flexible with regards to propellant, able to sustain high-power discharges across a wide variety of propellants, both conventional and alternative. When combined with their ability to throttle exhaust velocity with input power, IEP systems represent excellent candidates for future propulsion applications.

Historically research into the operation and fundamental principles of inductive systems (including those now being developed for thrsuter applications) has been focused on their utilisation for planetary entry simulation. This has been motivated by the relatively pure plasma produced when removing electrode contact with the discharge, thus reducing associated flow contaminants. However, despite their extensive history, several fundamental phenomena have only been subject to cursory investigations. Chief amongst these are the conditions at which transitions in the electromagnetic (capacitive or inductive) discharge regimes occur for different gases, as well as the methods used to identify and define them. Knowledge on these regimes is critical to increasing thruster performance, which is dependent on achieving sufficient energy coupling between the power source and the resultant plasma. Furthermore, information on the discharge chamber wall temperature and temperature distribution during high-power operation is also lacking. This requires present sources to be designed using conservative assumptions and neglecting spatially-resolved interactions between materials and the plasma.

The aim of this research is to assess the performance of alternative propellants in an inductive propulsion system, providing information on their potential impact on current propellants and future space operations. This includes measuring key performance metrics (thrust, efficiency), assessing the interaction between propellant and thruster and analysing how it may be improved in future thruster designs. Interactions include the influence of discharge tube wall thickness on the plasma boundary layer and discharge mode transition point, as well as the thruster-propellant coupling mechanism, observed as the interaction between charge-carriers in the plasma and current characteristics of the thruster driving circuit.

This thesis is structured as follows: Chapter 2 reports on the state of the art of electric propulsion, including previous research into alternative propellants and gaps in current

methods used to assess the electromagnetic behaviour of inductive systems. Chapter 3 details the research aim resulting from reviewing the current technology state, including key objectives required to meet this target. Chapter 4 provides the necessary background information and underlying principles required to interpret results from the project, including condensed theory on electromagnetic behaviour in inductive plasma discharges, an explanation of the measurement techniques developed and utilised within this thesis and a summary of the propellants selected for investigation. Chapter 5 presents the results and analysis of the research conducted. Results include values of thrust and specific impulse for the various propellants (including how the net system output may be improved by preferentially combining certain gas species) and assessments of discharge transient behaviour using measurements of the inductive coil current and discharge skin depth (optical and magnetic). This chapter also includes an assessment of the impact of discharge tube wall thickness on the plasma and the distribution of wall temperature during operation. Chapter 6 lists future work which may be performed to build on findings from this project and Chapter 7 summarises the findings of the research. Supporting material including a description of the numerical tool developed to simulate discharges within the chamber is given in the appendices of this thesis.

Chapter 2

Literature Review

The following chapter reports on the present state of the art of alternative propellants in electric propulsion. This includes the availability of alternative propellants, an overview of electric propulsion (and their respective acceleration mechanisms), factors influencing alternative propellant implementation and examples of past investigations, and an assessment of previous techniques used to analyse propellant-thruster interaction.

2.1 Propellant Availability for Propulsion

While the vacuum of space is itself, by definition, void of any significant quantity of atoms or molecules, certain resource-rich environments do exist within the solar system. These environments are the targets of contemporary and future exploration missions.
Planets and moons present the greatest concentrations of compounds which may be used as alternative propellants. These include vast quantities of hydrogen, oxygen, and nitrogen which occur naturally on the surface as well as in a surrounding gaseous atmosphere. Most large celestial bodies of interest have either already been or are intended to be mapped to some degree [16, 17, 21–30] in order to provide estimates of their chemical compositions. This provides an indication of the local resources which may be utilised for prolonged operations. An example of such a study is given in the case of Mars, where large-scale ISRU ground operations have been proposed. This

combines surface water and CO_2 from the Martian environment to produce O_2 and CH_4 as chemical propellant as well as consumables for sustained crew habitation missions [31]. Similar operations may be performed at other resource-rich locations such as Titan, which features an icy surface with considerable quantities of liquid CH_4 [32]. The major criteria for such ground-based operations is a sufficient resource density to allow launch from the planet or moon surface following propellant collection. While the thrust levels of electric propulsion are too low to facilitate such a transfer, chemical rockets could feasibly provide the function of couriering propellant back to orbit for a vehicle equipped with an EP system. However, with the majority of celestial bodies of interest possessing significantly weaker gravitational fields than that of Earth, launching propellant from these locations may still represent a reduction in effort to resupply spacecraft. This is further illustrated when considering interactions with icy asteroids or other Near Earth Objects (NEO) which exhibit gravity several orders of magnitude lower than that of Earth, thus requiring minimal chemical assistance to depart once propellants have been collected.

ISRU operations without contact with the moon or planet surface have also been proposed, collecting atmospheric gases while in orbit around the body. EP devices designed for such manoeuvres are termed Atmosphere-Breathing Electric Propulsion (ABEP), collecting and accelerating incident gas flow which would otherwise stagnate against the satellite surface to produce drag [5, 33, 34]. This may be used to significantly mitigate orbit degradation. While not able to collect sufficient quantities to fully resupply a vehicle (due to the species densities at orbits compatible with EP drive systems), designers of such systems have proposed the possibility of prolonging a given observation mission beyond its unassisted lifetime. Depending on the celestial body in question and its associated atmospheric density and gravitational field, this technique of ISRU may provide significant additional scientific return on a mission which would otherwise have already come to a close.

In addition to these remote planets and moons, several propellant sources are available in much greater proximity to present human operations. All crewed spacecraft, such as the International Space Station (ISS), produce a certain volume of waste in

solid, liquid, and gaseous form. Significant effort is exerted the reclaim this waste as reusable consumables, such as air and water, by means of the Environmental Control and Life Support System (ECLSS). However, certain by-products of the closed loop system lend themselves towards application as alternative propellants.

As the reclamation processes for liquid and solid waste produce largely dense solid by-products, the best candidate for use in EP systems are found in the gas reclamation cycle. One such process converts CO_2 back into O_2 for respiration. This involves the utilisation of a Sabatier reactor [35] which uses a given mixture ratio of hydrogen and CO_2 to produce O_2 and CH_4. The mixture ratio dictates the conversion efficiency of the system, though some proportion of the CO_2 remains unchanged and is subsequently ejected from the spacecraft environment as waste. In the case of the ISS, this is accompanied by the ejection of CH_4 as it presently serves no functional purpose aboard the station [36]. A similar method with similar results may be assumed in the case of long-duration missions such as those to Mars. Each of these ejected gases has potential as useful propellant and thus represents a presently un-tapped source for potential exploitation.

Earth-based manufacturing facilities are also able to produce these alternative propellants and at lower costs than classical propellants due to their abundance in the local environment. This allows gases identified at remote locations or obtainable through ECLSS analyses to be produced for laboratory research as well as application in a given mission. Vehicles utilising these propellants may thus resupply at their target destination, or launch with a baseline propellant composition which can be supplemented with resources collected once in the space environment.

It is clear from the above that the opportunities and sources of alternative propellants are many, found both on Earth, at locations of interest within the solar system, or even produced in-situ as a result of the vehicle ECLSS. However, in order to utilise such gases in an EP system, their compatibility and performance must be understood and measured against conventional propellants and their output.

2.2 Electric Propulsion Overview

Electric propulsion can be divided into three distinct categories; electrostatic, electromagnetic, and electrothermal. Each of these catagories exhibits its own acceleration mechanism and preferred propellant characteristics.

The first documented electric propulsion system, developed by Goddard in 1917 [37], utilised the electrostatic principle; a method which is still in use today and represents the most popular form of EP in the current space market (due largely to this legacy). A diagram of the electrostatic operating principle is shown in Figure 2.1.

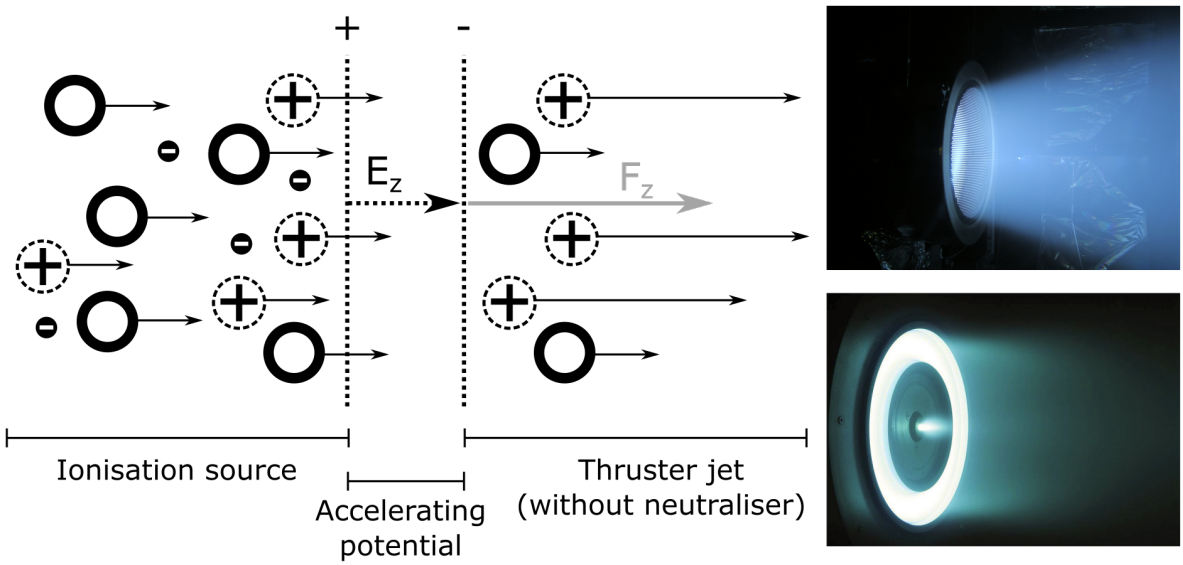

Figure 2.1: Electrostatic thruster operating principle and operational examples: JPL NEXIS ion thruster (top) [38] and University of Michigan 6 kW Hall effect thruster (bottom) [39]

Electrostatic thrusters utilise a potential difference in order to accelerate ions and generate thrust. This potential difference may be achieved by applied or self-induced electric fields, as seen in gridded ion thrusters (GIT) or Hall Effect Thrusters (HET), respectively. Field Emission Electric Propulsion (FEEP) thrusters also use applied electric fields, though with liquid rather than gaseous propellants [40]. Through these electric fields, electrostatic thrusters can produce exhaust velocities $>$ 100,000 m/s (with xenon acting as the propellant [3]) for sufficiently high voltages (and hence field strengths). It

should be noted that due to the bias of positively charged species leaving the thruster, a neutralising cathode is also required in order to balance the flux of ions with an equivalent population of electrons.

The source of ions for acceleration within the thruster may vary, though many contemporary models achieve flow ionisation either through a standard anode-cathode arrangement or a microwave/radio-frequency excitation stage before the accelerating potential [3, 6]. Due to the dependency of the electrostatic acceleration mechanism on charged heavy species, thrusters of this design prefer propellants which exhibit a low ionisation energy such that a high number of heavy species passing through the ionisation chamber may be accelerated. All non-ionised heavy species passing through the potential difference will be unaffected and be expelled at low velocities generated by the pressure difference. Propellants which do not contain corrosive species are also preferred due to the direct contact between the electrode components and the plasma [3]. For these reasons, electrostatic thrusters typically operate with noble gases, most commonly xenon due its low ionisation energy.

As their name denotes, electromagnetic thrusters make use of electromagnetic rather than electrostatic interactions in order to accelerate their flow. As shown in Figure 2.2, electromagnetic thrusters rely on the interaction between electric and magnetic fields in order to accelerate ions by means of the Lorentz force [3].

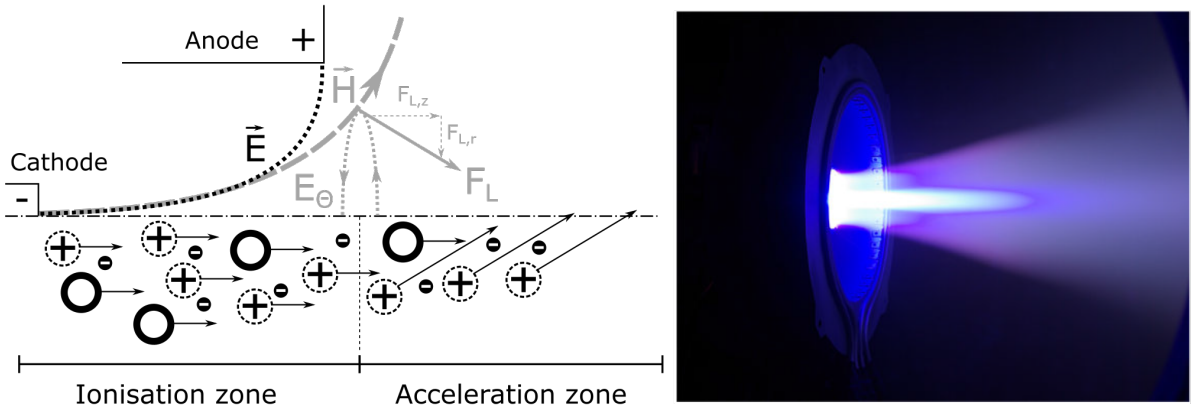

Figure 2.2: Electromagnetic thruster operating principle (for applied field case) and operational example of the IRS SX3 AF-MPD thruster [41]

In the case displayed, the applied field (AF) Magnetoplasmadynamic thruster (MPDT), interaction takes place between the expanding magnetic field (H, generated by an externally-applied magnetic coil) and the flow induced azimuthal electric field (E_Θ). Due to the orientation of these fields, the resultant acceleration vector of the charged heavy species (F_L) contains both a radial (or "pinching") and axial component ($F_{L,r}$ and $F_{L,z}$, respectively), with the latter of the two responsible for accelerating particles to velocities in the order of 20,000 - 50,000 m/s [2]. While also relying on charged heavy species as electrostatic thrusters do, electromagnetic thrusters utilise propellants with a lower molar mass than xenon in order to increase the impact of Lorentz force acceleration hence the exit velocity of the ions. However, due to the direct contact between the gas and the electrodes, the use of chemically reactive (corrosive) propellants is restricted. As a result, commonly utilised propellants include argon and hydrogen [41, 42]; Ar propellant can be used to produce a larger ion population for acceleration, compared to hydrogen, per unit of input energy due to the difference in ionisation energy and additional molecular losses associated with hydrogen. However, hydrogen ions may be accelerated to greater final velocities due to their low mass compare to argon. The choice of propellant is hence dependent on the objective of the thruster, being optimised towards either thrust or I_{sp}.

Pulsed Plasma Thrusters (PPT) are also included in the electromagnetic class. However, as these operate non-continuously and at lower power scales, they are not discussed further within this thesis.

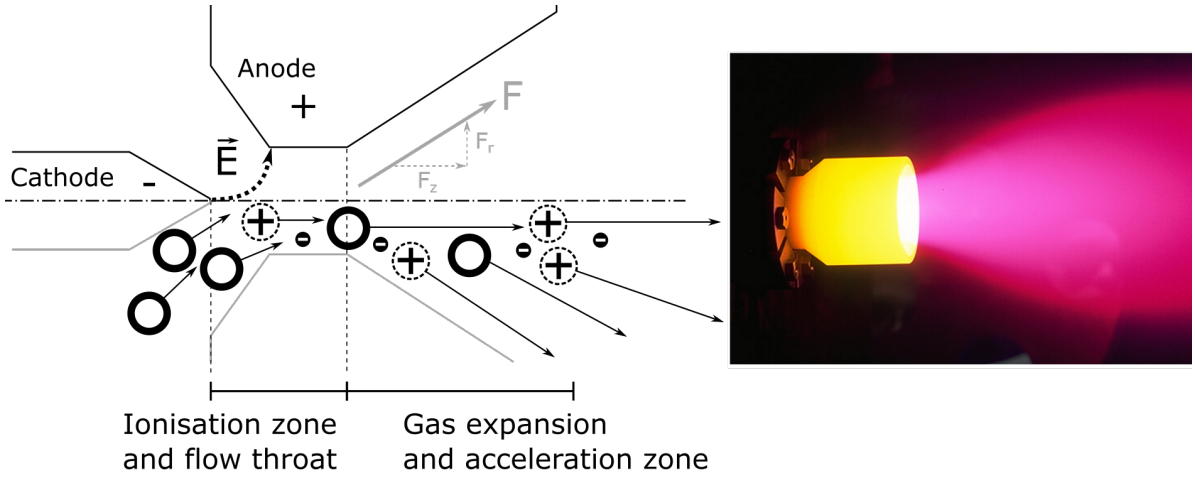

Figure 2.3: Direct contact electrothermal operating principle and operational example of the IRS HIPARC-R [43] system

Finally, electrothermal thrusters use electric current to heat a propellant flow and accelerate it using only gasdynamic mechanisms. As seen in Figure 2.3, the arcjet class of electrothermal thruster relies on contact between the working fluid and the electrodes to generate the discharge and ionise the gas. Another class of electrothermal thruster, the resistojet, uses a heated structure or filament to heat the gas. These systems are suited to low I_{sp} applications due to the low temperatures reached compared to other EP devices.

Also seen in Figure 2.3 is the similarity between arcjet and MPDT systems. The major difference between the two is the pressure of the discharge, with arcjets using substantially higher chamber pressures (approximately 1-2 orders of magnitude [44]) to generate choked flow at the nozzle throat and hence supersonic flow at the thruster nozzle exit. This increase in pressure also acts to dampen the Lorentz force effects by reducing the mean free path between all species and thus restricting motion ions may otherwise have as a result of the electric field orientation. Due to the utilisation of all heavy species rather than only those carrying charge, net thrust for electrothermal thrusters is typically higher than that of their electrostatic or electromagnetic counterparts, though their operation also leads to a significantly lower exit velocity. Typical arcjets exit velocities do not exceed 10,000 m/s [2], due partially to the dissociation and frozen flow losses associated with the high propellant flow rates (compared to other EP systems) used. The reduced reliance on total flow ionisation degree, as well as the direct contact between electrode arrangement and propellant, result in electrothermal thrusters utilising similar propellants to electromagnetic systems; chiefly argon and hydrogen. Despite the frozen flow losses associated with hydrogen, it is often preferred to maximise I_{sp} as a result of its low atomic and molecular mass.

Inductive and helicon propulsion systems represent a separate branch of electrothermal EP to that shown in Figure 2.3. One of the major restrictions removed by the design of these systems is that of material incompatibility and degradation, shown as a limiting factor throughout the previous examples. Inductive and helicon sources operate without direct contact between the plasma and electrode arrangement, separating the two via a dielectric medium which forms the physical structure of the discharge chamber (or tube), as seen in Figure 2.4.

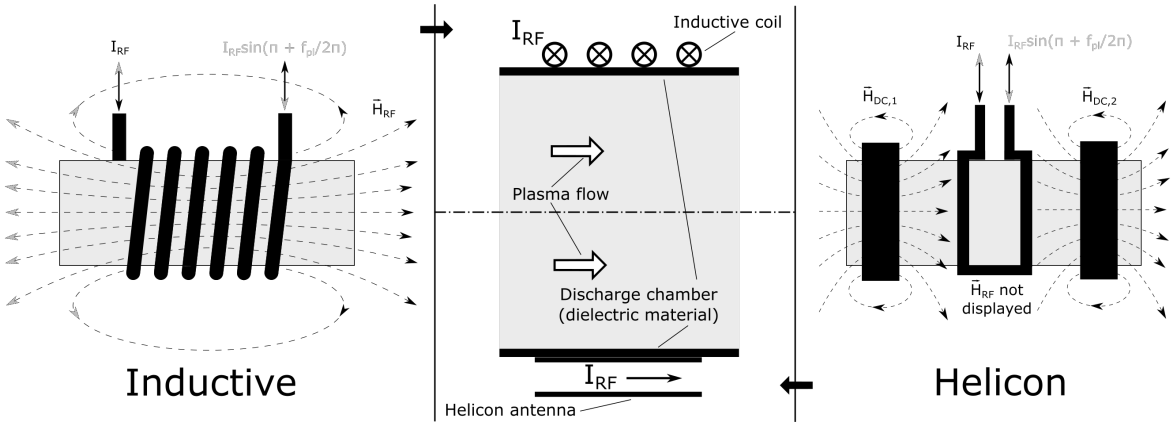

Figure 2.4: Inductive and helicon discharge chamber arrangements

Rather than a cathode-anode electrode arrangement, these systems utilise a coil (or antenna) driven with an alternating current (AC) to transfer energy to the propellant and generate the plasma discharge. A more thorough description of the fundamental principles of this behaviour is given in Section 4.2.2. As seen in Figure 2.4, inductive and helicon systems are almost identical in their assembly, with the distinction being the antenna arrangement and hence primary method through which they transfer energy to charged species within the flow, specifically electrons. Inductive systems are so named for the dominance of their magnetic field component, inducing an azimuthal current within the flow which in turn transfers energy to the heavy particles [45]. Helicon sources, on the other hand, are characterised as using helicon waves (a form of very low frequency Whistler waves [46]) to stimulate electron motion [47]. The distinction between these two discharge modes is somewhat controversial, with their behaviour usually observed through indirect methods [48–50] thus making the presence of helicon waves or a high-inductive characteristics (such as a theta-pinch form [51]) during experiments largely conjecture. Many developing electrodeless thrusters are named after one of these two phenomena and will thus be discussed with reference to their proposed characteristic behaviour.

A summary of the three classes of EP and their respective conventional propellants are shown in Table 2.1. Alternative propellants are thus those not contained within this table, selected due to greater availability or lower associated costs as discussed in Section 2.1.

Table 2.1: Classes of electric propulsion and their respective conventional propellants

	Criteria	Primary	Secondary
Electrostatic	• Low ionisation energy • Low gas reactivity/corrosivity	Xe	Ar, Kr
Electromagnetic	• Low ionisation energy • Low molar mass • Low gas reactivity/corrosivity	Ar, H_2	-
Electrothermal (direct contact)	• Low molar mass • Low gas reactivity/corrosivity • High thermal conductivity	H_2	Ar, N_2H_4
Electrothermal (electrodeless)	• Low molar mass • High thermal conductivity	Flexible	

A number of other propellants which meet the thruster-specific criteria have not been included in Table 2.1 due to practical considerations. For example, alkali metals such as lithium and caesium have been tested in MPD [52] and ion thrusters [53], though issues of spacecraft compatibility [2] have resulted in a discontinuation of these propellants. Mercury was also once of key interest for ion thrusters [54, 55], though its toxicity put it at a distinct disadvantage to other propellants for thruster testing and ultimately ended its use for EP applications. Table 2.1 hence represents conventional propellants as they are in the present EP field.

2.3 Key Factors Influencing Electric Propulsion with Alternative Propellants

As seen in Table 2.1, each class of EP is suited to certain propellants and restricted from others, depending on their individual traits. Over the course of several decades, alternative propellants have been investigated in a number of EP systems, with motivations ranging from continual ABEP operation in orbit [5,6,8,9] to long-duration cis-lunar trajectories [7]. The class of EP tested or assessed in each of these studies has been influenced by the state

of technology at the time, the legacy of the given device, and its ability to be adapted to new propellants. While thrusters from each of the three branches of EP have been tested with alternative propellants, clear trends as to their compatibility may be identified. Table 2.2 provides an overview these tests.

Table 2.2: Overview of past studies of alternative propellants for electric propulsion

EP class	Study & Application	Propellant(s)
Electrostatic		
Ion thruster	Dressler et. al (2000) [4], *low-cost EP*	Iodine
	Nishiyama (2003) [5], *ABEP, Earth*	Ar, O_2, N_2, CO_2
	Cifali et. al (2011) [6], *ABEP, Earth*	O_2, N_2
Hall effect thruster	Frisbee et. al (1998) [7], *cis-lunar transport*	O_2
	Cifali et. al (2011) [6], *ABEP, Earth*	N_2, air
	Pekker and Keidar (2012) [8], *ABEP, Earth*	Air
	Hohman (2012) [9], *ABEP, Mars*	CO_2
	Shabshelowitz (2013) [10], *ABEP, Earth*	Ar, N_2
Electromagnetic		
MPDT	Uematsu et. al (1984) [11], *storage/supply*	Ar, O_2, H_2, NH_3
Electrothermal		
Arcjet	Hou et. al (2011) [12], *low-cost EP*	Water
	Shiraki et. al (2015) [13], *low-cost EP*	Water
	Yanagida et. al (2015) [14], *low-cost EP*	Water
Helicon	Charles (2008) [15], *low-cost EP*	N_2, CH_4, NH_3, N_2O
	Shabshelowitz (2013) [10], *ABEP, Earth*	Ar, N_2, air

The first and most fundamental restriction to operation with alternative propellants is that of chemical compatibility. During operation, EP systems are required to maintain nominal performance for periods in excess of 10,000 hr [56, 57]. Any degradation to

critical components which would jeopardise this performance, such as decreased electrical conductivity between the electrodes (due to erosion) or a reduction of potential on the accelerating grid (resulting from surface oxide formation), is considered severe and would restrict the implementation of certain propellants. Ion thrusters, arcjets, and Magnetoplasmadynamic Thrusters (MPDT) showed significant electrode erosion when operated with chemically reactive alternative propellants [6, 11–14]. Thruster degradation was particularly observable when utilising oxygen, where each of these thruster classes suffered substantial damage to the electrodes over relatively short test times. For alternative propellants to be considered in these systems, significant improvements to the chemical resilience of thruster materials (particularly the tungsten electrodes) would be required. These improvements may come in the form of additional resistive coatings or a complete reselection of electrode material, though these changes will also heavily impact on the discharge conditions. Hall Effect Thrusters (HET) also showed significant degradation in some studies [6]. HET investigations in which no degradation was observed were also recorded [9, 10], though authors of these studies note that testing times were significantly lower than the thruster lifetime and that further testing would provide more substantial indicators of potential damage. Due to the direct contact between electrodes and plasma within these systems, it is likely they will also require significant material modifications. The most compatible systems tested were the helicon thrusters, which displayed no material degradation despite the presence of reactive species such oxygen and hydrogen.

The second critical issue is the compatibility of the alternative propellant with the thruster accelerations mechanism, being either electrostatic, electromagnetic, or electrothermal. Alternative propellants must be comparable to their conventional counterparts with respect to the total propulsion system mass and input power requirements. Studies of ion thrusters showed theoretically superior exit velocities with alternative propellants owing to their lower molar mass [5]. However, in practice these systems suffered severe reductions in thrust efficiency due to the necessary increase in input power [6]. HET, MPDT, and arcjets showed performance within the same order of magnitude at that achievable using conventional propellants [6, 11–14]. However, the aforementioned material limitations act to limit the potential of such systems. Performance for the helicon sources was mixed. The Helicon Double Layer Thruster (HDLT [15]) achieved specific impulses comparable to conventional electrostatic devices (1400 - 2700 s) using alternative propellants, while conventional helicon source

(discussed in [10]) noted negligible improvement over cold gas specific impulse when operating with N_2. This shows certain helicon sources may require additional acceleration mechanisms to make full use of their capabilities.

The third major consideration is scalability of the system with respect to power. While majority of the thrusters tested were small-scale (< 2 kW), the theoretical mission analyses indicate the need for high-power EP systems to undertake the necessary trajectories and manoeuvres. This is supported by the missions currently being planned, some of which feature EP systems in excess of 10 kW [57, 58] or 100 kW [58].

These considerations of material compatibility, comparable performance, and power/scaling are inherent to the design of the thruster. In addition to these, a number of considerations in test procedure can be identified from the studies assessing alternative propellants.

The first of these is the necessity to consider propellant particle flux as well as mass flow rates during comparison. Flows measured in terms of kg/s are useful for mission analyses and when determining thruster performance metrics such as the specific impulse. However, consideration must also be given to the thruster discharge behaviour. The degree of ionisation within the discharge dictates its interaction with the thruster excitation mechanism, whether electrode or coil. This degree of ionisation is dependent on the electron number density and hence the number of cold propellant particles entering the discharge volume. It is therefore important to consider particle flux and the mass flow rate of a propellant, depending on the performance metric being assessed.

Once the flux of particles entering the control volume has been considered, differences in the propellant chemical compositions may be analysed and accounted for. These include considerations of the propellant structure (such as atomic, molecular, or polyatomic), the associated modes of energy, the ionisation energy of the neutral species, and gasdynamic effects resulting from the discharge. Gasdynamic effects, in particular heat from the discharge, are particularly important given their impact on mechanical components of the thruster. This includes components which may not be in direct contact with the plasma. A fixed propellant flux also allows the geometry and distribution of the discharge to be assessed, assisting in geometrical developments to the thruster.

These factors highlight the procedural considerations required during the investigation of alternative propellants for electric propulsion.

2.4 Electromagnetic Transition Characterisation

From the review of alternative propulsion research presented in Section 2.3, electrodeless thrusters present some of the most promising candidates for future development, due largely to their flexibility of propellant and compatibility with reactive gases. While the studies investigated focus only on helicon rather than inductive designs, the latter has an extensive history of development for planetary entry simulation and has previously been implemented in thruster research campaigns [59]. The two are also inherently linked, with the inductive and helicon modes representing two of the discharge regimes inherent to electrodeless plasma sources [60, 61].
Also highlighted through the helicon studies ([10, 15]) is the discrepancy in performance of different electrodeless thrusters. As stated, this is largely attributable to the acceleration mechanism associated with the particular thruster design. Electrodeless thrusters have previously been enhanced with mechanical and magnetic nozzles depending on their discharge conditions.

Mechanical nozzles are primarily suited towards flows with a low degree of ionisation, where gasdaynamic expansion (and compression) may be used to accelerated the neutral and charged heavy particles. The implementation of this nozzle type is well recorded at the University of Stuttgart's Institute for Space Systems (IRS), where convergent [62, 63] and Laval nozzles [50] have been used to recreate planetary entry conditions for Earth, Mars, and Venus. The limitations of these nozzles are however noticeable in the final thruster exhaust velocities (which are lower than those achieved through electrostatic or electromagnetic acceleration) and the possibility of nozzle damage after being in prolonged contact with the plasma.
Magnetic nozzles are more effective for flows with a higher degree of ionisation, as neutral particles are unaffected by the induced Lorentz force acceleration. Charged particles, however, may be accelerated to similar exit velocities (depending on the magnetic field strength) seen in MPDT. This is the operating principle behind the Variable Specific Impulse Magnetoplasma Rocket (VASIMR®) [64], developed by NASA for long-duration EP missions with alternative propellants. These nozzles do not risk degradation as mechanical nozzles do (having no direct contact with the flow), though require a significant degree of flow ionisation in order to warrant the additional input power required.

Double layers such as those seen in the HDLT [15] are an inherent feature to the particular discharge mode and are not subject to a design process. They do however require set discharge conditions to be reached, necessitating a detailed understanding of the mechanisms behind double layer formation.

Each of these acceleration mechanisms requires a detailed understanding of the discharge within the thruster, with mechanical and magnetic nozzles requiring additional knowledge of their impact on the discharge such that optimal performance may be achieved. This presents some difficulty when testing a number of chemically dissimilar alternative propellants, as each propellant behaves in a unique manner, producing a particular set of gasdynamic (viscosity, chemical composition) and electromagnetic (ionisation degree and distribution) characteristics. It is thus preferable to perform analyses of alternative propellant discharges without additional acceleration mechanisms such that their individual characteristics may be identified for subsequent thruster improvement.

The discharge chamber (tube) wall thickness may also be adapted to significantly alter performance. In contrast to nozzle implementation, which may lead to changes in the distribution of species within the discharge, variations of the tube wall thickness tend only to influence the coupling efficiency between coil and plasma by changing the dielectric separation between the two (for small variations which do not significantly alter the discharge volume or pressure). This behaviour has been confirmed by Nawaz and Herdrich [65], who investigated variations in wall thickness from 1.25 to 2.3 mm for air in an Inductive Plasma Generator (IPG). Their findings revealed a significant increase in coupled power with reductions in the tube wall thickness, implying greater coupling (and hence thruster efficiency) may be achieved through more careful selection of the discharge chamber components. Such an investigation would benefit alternative propellant analyses by assessing the sensitivity of propellants to such factors and allowing better categorisation with respect to the resultant discharge.

Whether assessing the impact of geometrical modifications or comparing different propellants, the ability to accurately assess the thruster discharge is critical. This has been a drawback of previous works, where gasdynamic metrics have been the dominant

focus. The prioritisation of these metrics is understandable, with the primary focus of thruster development being achievable performance through the plasma exhaust. However, in the case of IEP, thrust is strongly linked to the discharge regime and the subsequent coupling of propellant with the coil/antenna. The ability to quantify electromagnetic metrics would therefore greatly enhance the understanding of these systems.

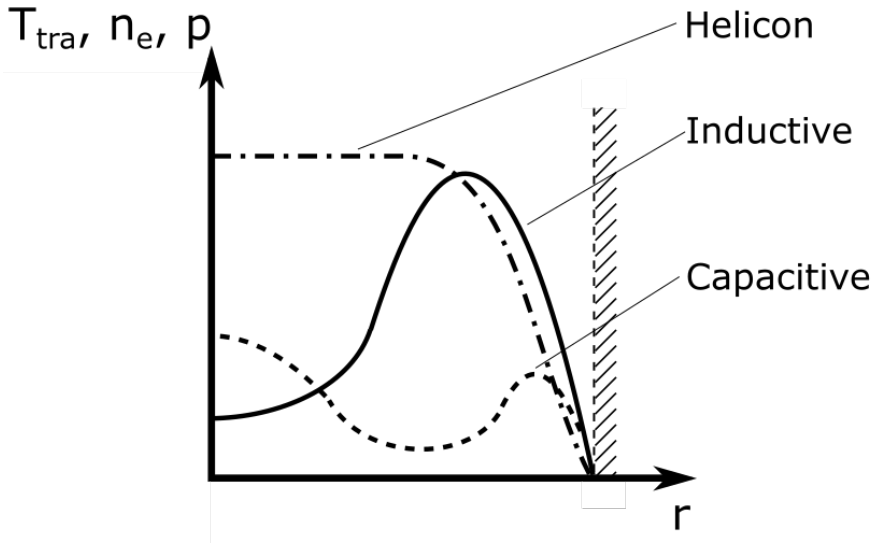

Figure 2.5: Qualitative comparison of temperature, electron number density, and pressure distributions for the respective discharge regimes

The inductive and helicon discharge regimes represent two of the three defined operational modes of electrodeless plasma sources. An additional capacitive mode completes the set, defined as a discharge in which the axial electric field (owing to the potential difference between each end of the coil or antenna) is dominant. While a more comprehensive description of the discharge regimes is available in Section 4.2.2, Figure 2.5 describes their behaviour in sufficient detail for the assessment of previous characterisation techniques.

Common gasdynamic metrics used to assess and characterise discharge states are heat flux and pressure [50, 66]. Such measurements may be performed either in the exhaust (jet) of the thruster or in the discharge chamber itself, subject to access and associated disturbances to the flow. Since large-scale (>100 kW) laboratory models for planetary entry simulation often require water cooling to sustain the necessary flow

conditions, calorimetric heat flux measurements may be performed on the discharge chamber itself. It should be noted that across the radial profile of the discharge tube, the steep thermal gradients translate to significant local deviations in the species thermal velocity and resultant collision cross-section. These factors are important when spatially-resolved reaction analyses, though to date such investigations have not been performed experimentally on the system due to a greater emphasis on jet diagnostics. Herdrich (2004) [50] notes the nominally low heat flux conveyed to the chamber cooling water during capacitive operation with the significant increase observed after transitioning to the inductive mode. It should be noted that the magnitude of the measured heat flux varies with propellant. Gases with low thermal conductivity are therefore being difficult to assess using this method. Since the generator used for this study was a purely inductive system (without the DC magnets used to instigate helicon operation [49, 67]), no heat flux trend associated with helicon operation was recorded. However, a distinction between so-called low and high inductive modes was noted in the study. The high inductive mode is associated with a significant decrease of the tube heat flux and an increase in the measured jet thermal power. A visible compression of the plasma to the centre of the discharge volume is also associate with this mode [50]. This compression is confirmed by radial profile measurements of the jet pressure, with the behaviour attributed to a theta-pinch phenomenon [51] caused by the Lorentz force of the induced plasma. An image of this phenomenon is seen in Figure 2.6 [1].

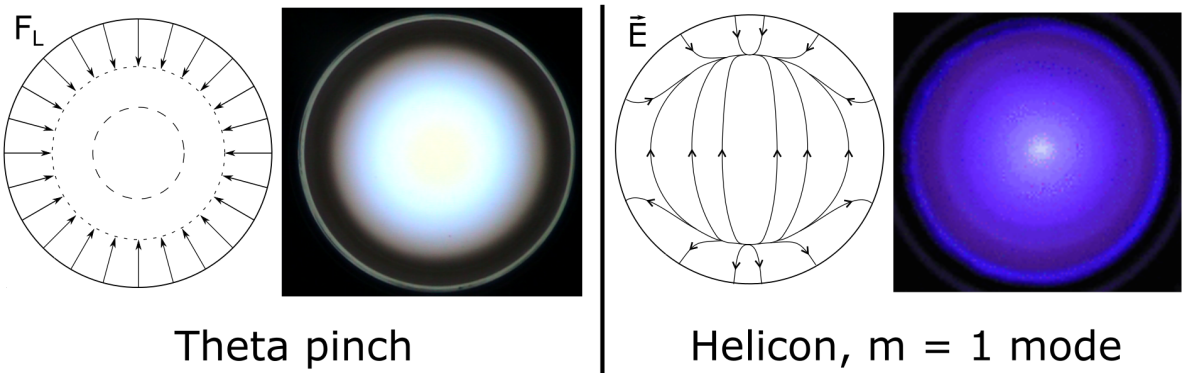

Figure 2.6: Comparisons of characteristic plasma densities in the theta pinch (left) and helicon (right) [67, 68] regimes, generated by the Lorentz force (F_L) or the distribution of the electric fields (E), respectively

[1] While a number of helicon modes have been documented, the m = 1 mode is the most common and in the field of propulsion is synonymous with the 'helicon' regime. A more detailed description of the various modes may be found in [67]

As shown in Figure 2.6, the plasma distribution associated with the theta-pinch mode shares similarities with distribution measurements in helicon sources [66], specifically a concentration of plasma about the chamber axis. The distinction between these two modes is still highly contentious, and as the driving forces behind theta-pinch and helicon operation are electromagnetic compression and wave excitation, respectively, information on the gasdynamics of the discharge does not provide sufficient evidence to differentiate between the two.

Discharges are also often assessed through the emission of visible radiation, with the intensity and spectrum of light emitted correlated to a particular discharge regime [10, 69–71]. The most common consensus is for low radiation intensity in the capacitive mode, moderate (and annular) in the inductive mode, and highest for the helicon mode [69], with a centralisation around the discharge chamber axis in agreement with the plasma distribution discussed previously. However, such distinct characteristics are often defined for a single gas (with a particular radiation intensity behaviour), with correlations to other, dissimilar gases not necessarily possible. Furthermore, transitions based on radiation intensity assume distinct changes between operational modes; a characteristic which depends heavily on the thruster antenna design and geometry and resultant interactions with the gas. In addition to measurements of intensity, certain wavelengths are also used to mark transitions to a particular regime. One of the most commonly referenced characteristics is the blue core said to be associated with helicon discharges [69]. This visual marker is defined as a concentration of radiation intensity about the tube axis (associated with the characteristic energy distribution of helicon discharges [67]) with the radiation spectra of a common operating gas, Ar. While many researchers attempt to utilise this marker to confirm the operation of their thruster in the helicon regime, many do not account for discrepancies in gas-specific radiation. An example of this is Shabshelowitz 2013 [10], where the absence of a blue core was noted as a failure to reach the helicon mode during nitrogen operation.

Figure 2.7 shows the emission spectra for Ar, O, and N atoms as taken from the National Institute of Standards and Technology, NIST, database. While the dominance of ion radiation is clear for each of the species, the wavelength at which it is emitted varies significantly. Ar and N ions show particular dissimilarity, with the difference in emitted wavelength detectable by the naked eye. In addition to this, the presence of molecular

radiation is not applicable in the Ar case, whereas it is substantial in discharges involving either oxygen or nitrogen. For these reasons, indicators relying on the wavelength of a particular species, and therefore colour visible to the naked eye, are not applicable when comparing chemically dissimilar discharges.

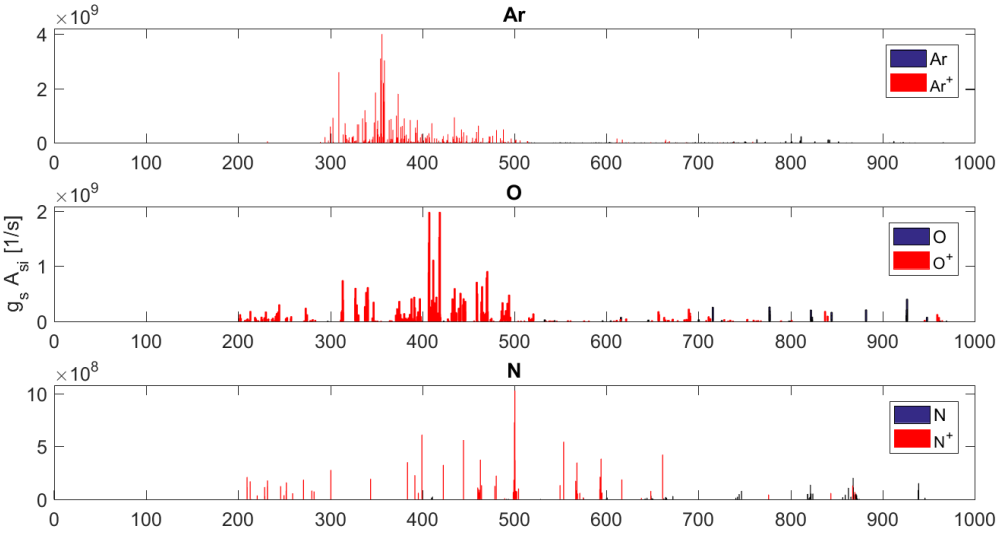

Figure 2.7: NIST emission lines for Ar, Ar^+, N, N^+, O, and O^+ [72–76]

Techniques previously used to assess electromagnetic properties of the discharge (electron number density or magnetic field distribution) have typically only investigated a single condition (with fixed pressure, input power, propellant, etc), with limited applicability to other thruster configurations [77].

Table 2.3: Electron number density before and after capacitive-inductive transition for Amorim et. al setup using argon [77]

p [Pa]	$P_{cap,max}$ [kW]	n_e [m^{-3}]	$P_{ind,min}$ [kW]	n_e [m^{-3}]
8.5	0.330	3.284×10^{13}	0.403	4.428×10^{15}
17.3	0.257	3.831×10^{13}	0.301	2.504×10^{15}

A study by Amorim et. al recorded the electron number densities within the discharge zone of an argon plasma using a Langmuir probe setup. Measurements were taken before and after transitions (between the capacitive and inductive modes) for different chamber

pressures (8.5 and 17.3 Pa) [77]. The results of these measurements are listed in Table 2.3. While changes in the electron number density are useful in identifying the presence of the azimuthal ring current (and hence transition to inductive operation [45]), studies such as this do not mention influences from the thruster configuration or coil geometry. Furthermore, current in the coil is significantly altered from that in the power supply due to the presence of the capacitor array (discussed in Section 4.2.1). As it is coil current which directly influences the discharge, total input power (as listed in Table 2.3) is of limited use as a transition metric. A theoretical study by Kortshagen et. al investigated the coil current required to sustain the inductive discharge [70], though again only for a limited number of argon conditions and neglecting critical inductive factors such as the skin effect. The differences in chemical properties of alternative propellants have a significant impact on the electromagnetic behaviour of inductive plasma discharges, thus requiring comprehensive analyses to accommodate these differences as well as focus on the appropriate component of input electrical power. As there is not presently a comprehensive study to exemplify this impact, collecting such data will be of great value to this thesis.

As can be seen from the techniques analysed in this section, a reliance on heat flux, pressure, and visible radiation can lead to uncertainties in the evaluation of electrodeless thrusters in an experimental environment. Characterisations using pressure distribution and heat flux measurements require high thermal conductivity from the propellant. Furthermore, these measurements are only useful when assessing the gasdynamic behaviour of the thruster jet, with the discharge itself driven by charged species within the volume. Optical techniques also face limitations, relying on strongly radiating heavy particle species to identify discharge regimes. The measurement of electromagnetic metrics (electron number density, magnetic field distribution) presents a more accurate method to describe the discharge regimes. However, these measurements should be performed for multiple, dissimilar species and address electrical input power components in direct interaction with the discharge. These factors form the key considerations when assessing discharge regimes in an electrodeless thruster system.

2.5 Review Summary

After reviewing the associated literature on the implementation of alternative propellants for space operation, a number of conclusions may be drawn. Firstly, use of chemically reactive species, such as O_2 or H_2, requires the chosen propulsion platform to be chemically compatible with the propellant. Significant reductions in the operational lifetime of the thruster as a result of chemical incompatibility negates any potential increase in thruster performance or propellant availability. Of the EP classes investigated, electrodeless designs (helicon and inductive) display a clear advantage in their ability to utilise a range of chemically dissimilar propellants and their throttleable design. These systems may also be fitted with additional acceleration mechanisms such as mechanical or magnetic nozzles. However, in order to assess fundamentals of the discharge, it is preferable to analyse discharge behaviour without additional acceleration systems in place. These may be investigated in subsequent campaigns, with the focus of this work being the coupling between the various propellants and the excitation mechanism rather than the acceleration process. Finally, the methods to analyse thruster performance using alternative propellants have typically either focused on gasdynamic behaviour or over a very narrow range of flow conditions (often for a single gas) using electromagnetic techniques. Electromagnetic techniques provide the most accurate information on the thruster discharge and can be used to assess the behaviour of chemically dissimilar propellants. These techniques may also be used to gain a greater understanding of the electromagnetic discharge regimes present in electrodeless thruster systems.

Chapter 3

Gap, Aim, and Objectives

As detailed in Chapter 2, attempts to implement alternative propellants in conventional propulsion systems have been met with measured success. Electrodeless thrusters showed good compatibility for a wide range of propellants, without corrosion issues suffered by the other EP systems. These systems typically operated at low powers and propellant flow rates. There is therefore a gap in knowledge regarding the performance of alternative propellants in a high-power electrodeless thruster.There is also a lack of characterisation techniques which may be used to assess propellant utilisation in electrodeless EP systems, particularly with respect to electromagnetic discharge regimes. These regimes are of critical importance, determining the coupling efficiency between the coil and propellant. Hence the development of techniques which can be applied to chemically dissimilar propellants, focusing on electromagnetic behaviour, would represent a significant improvement in the state of discharge characterisation and thruster analysis.

The aim of this research is thus to address the aforementioned gaps in knowledge, implementing and comparing the performance of a number of alternative propellants in an electrodeless propulsion system, with particular focus on the electromagnetic discharge regimes.

In order to realise this aim, the research objectives of this project are identified as follows:

- Measure critical thruster parameters (thrust, I_{sp}, thrust-to-power) for the chosen propellants; Ar, O_2, N_2, and CO_2.
- Develop techniques to analyse the interaction between the RF coupling mechanism (coil) and propellant, with particular focus on the electromagnetic discharge regimes and their impact on net thruster performance.
- Investigate the influence of the discharge tube wall thickness on different propellants to assist in future IEP designs.

Chapter 4

Methodology

This chapter presents the methodology used in this research. The chapter includes a list of propellants assessed, a description of the experimental setup and thruster platform, and the measurement techniques used to assess thruster performance and to characterise the discharge regimes.

4.1 Alternative Propellant Selection

Following an assessment of celestial bodies within the solar system (and their chemical compositions/phases) as well by-products from spacecraft ECLSS, four candidate propellants were identified; these are argon, oxygen, nitrogen, and CO_2.

Argon was selected due to its similarity to the conventional propellant xenon, as both enter the discharge volume as an atomic gas. This reduces the frozen flow losses to excitation and ionisation and allows monatomic experiments to be conducted with relatively low cost (compared to Xe). Argon has also been extensively researched in plasma physics, providing the necessary information to conduct discharge simulations (see Section 4.4).

Oxygen and nitrogen were selected in order to provide two candidate propellants exhibiting a diatomic structure. This allows comparisons to the monatomic argon as well to each other, given their respective dissociation and ionisation energies (yet similar

ion molar mass). These two gases are abundant within the solar system, constituting the primary atmospheric components of several large bodies such as Earth [21] and Titan [17]. In addition, oxygen may be extracted in significant quantities by processing stores of water found on asteroids and other icy bodies [23, 25] [1].
Finally, CO_2 was chosen as the polyatomic propellant candidate, allowing knowledge gained from oxygen experiments to be built upon. CO_2 also represents an attractive propellant choice; it is both a significant waste component in spacecraft ECLSS [35] and is the primary atmospheric component on Mars [16].

As may be seen in Table 2.2, the choice of propellants discussed here agrees well with those investigated in previous campaigns, allowing good comparisons of their performance in various EP systems.

4.2 Experimental Facility

Experiments for this thesis were conducted at the IRS Tank 3 facility in Stuttgart, Germany. Figure 4.1 shows photographic and schematic depictions of the experimental setup, including the vacuum chamber within which experiments were conducted. The length and diameter of the tank are 3 m and 2 m, respectively, leading to an internal test volume of approximately 9.4 m^3. This chamber is attached to the main building vacuum system, capable of extracting 150,000 m^3/hr of air at atmospheric conditions and 250,000 m^3/hr at lower pressures (<10 Pa). The minimum tank pressure (without propellant flow) is measured to be between 1 and 3 Pa [2], though the scale of propellant flow rates utilised during operation (in the order of g/s) leads to ambient test pressures of 10-30 Pa and thruster discharge pressures of 500-2000 Pa. While this is a relatively high ambient pressure range for electric propulsion applications, the facility's purpose as a test platform for high-power thruster development requires such flow rates in order to match the geometry scale (exit diameter $\approx$ 0.1 m) of electrothermal thrusters installed.

[1] Note that restrictions in time prevented the other component reclaimed from water processing, hydrogen, from being tested.

[2] This variation is due to leakages resulting from sealings both on Tank 3 itself and in other sections of the vacuum facility. The central vacuum facility is connected to several test platforms, with leakages at one site observed to have an effect on the remaining sites.

For these mass flow rates, an ambient tank pressure of absolute zero would only increase the pressure-based thrust by 0.5-6.4 %. It should also be noted that this pressure is too high to ignite a conventional helicon source, further motivating the use of inductive propulsion.

Propellant flow at this facility is controlled using two Bronkhorst mass flow controllers (F-202AV and F-203AV), capable of delivering a maximum of 4.31 g/s and 6.47 g/s, respectively, with minimum accuracy of ±2 % at the flow rates tested (accuracy dependent on flow rate) [78, 79]. The facility ambient pressure during operation was measured using a Pfeiffer PKR 251 FullRange gauge at a pressure tap on the tank wall 0.4 m from the thruster outlet. This position is upstream of the plume expansion and is hence minimally affected during operation. The accuracy of this gauge is ± 30 % [80]. However, it has been repeatedly cross-checked with an MKS Baratron 622 pressure gauge with an accuracy of 0.25 % [81]. The two have consistently shown good agreement in the ambient tank pressure range and hence tank measurements are deemed reliable.

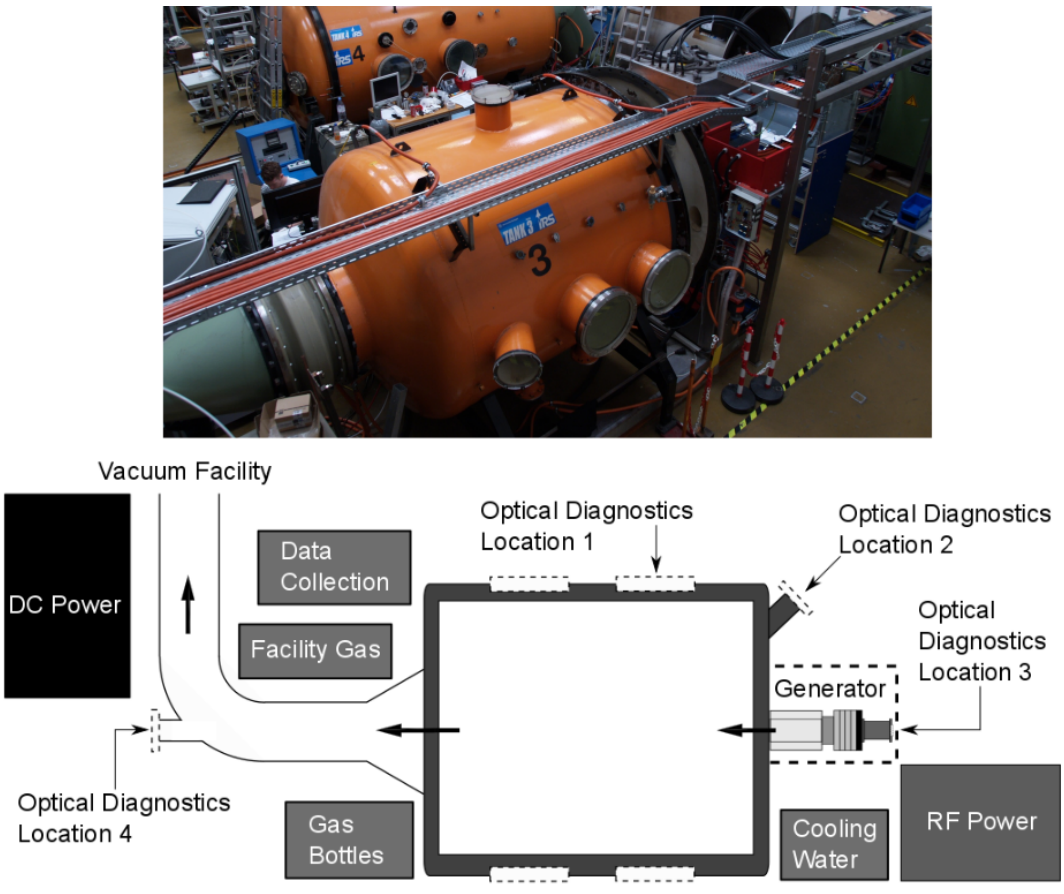

Figure 4.1: Tank 3 test facility in the Institute for Space Systems at the University of Stuttgart

Previous experimental campaigns conducted in Tank 3 have featured both RF and DC thrusters as well as hybrid systems representing a combination of the two [59]. As such, the experimental setup is equipped with both DC and RF power connections, delivering a maximum input power of 100 kW and 180 kW, respectively. The available DC power may also be increased with the implementation of additional cables, with the high-current facility capable of delivering a maximum of 6 MW sustained power. The facility is also equipped with gas regulation systems for certain gases (Ar, N_2, O_2) as well as bottled gases (CO_2, H_2). Furthermore, the vacuum facility has recently been fitted with a nitrogen injection system to dilute gases at risk of undergoing explosive recombination from their dissociated state. This removes the previous practice of requiring explosive gases to be diluted with nitrogen while still in the test chamber, thus allowing undisturbed testing to be conducted. A high-pressure (1.6 MPa) water cooling system allows thrusters to maintain continual high-power operation for test times in excess of 30 minutes.
Furthermore, the facility is fitted with a number of measurement devices, both active and passive, at a variety of locations inside and outside the test volume. These devices enable characterisation of the thruster performance, discharge behaviour, and critical component integrity during operation. A number of access points for optical diagnostic equipment have also been installed, allowing non-intrusive measurements to be performed. A summary of the thruster operating conditions presented in this thesis are listed in Table 4.1. In this table, P_A is the power measured at the laboratory power supply anode [82]. Due to inherent losses in the power supply triode arrangement, later references to input power are given in terms of the effective coil power, $P_{RF} = 0.75P_A$.

Table 4.1: Summary of thruster operating conditions

P_A [kW]	0 - 180
$\dot{m}$ [g/s]	0.75 - 3-86
p_{Tank} [Pa]	1- 30

4.2.1 Thruster Platform - IPG7

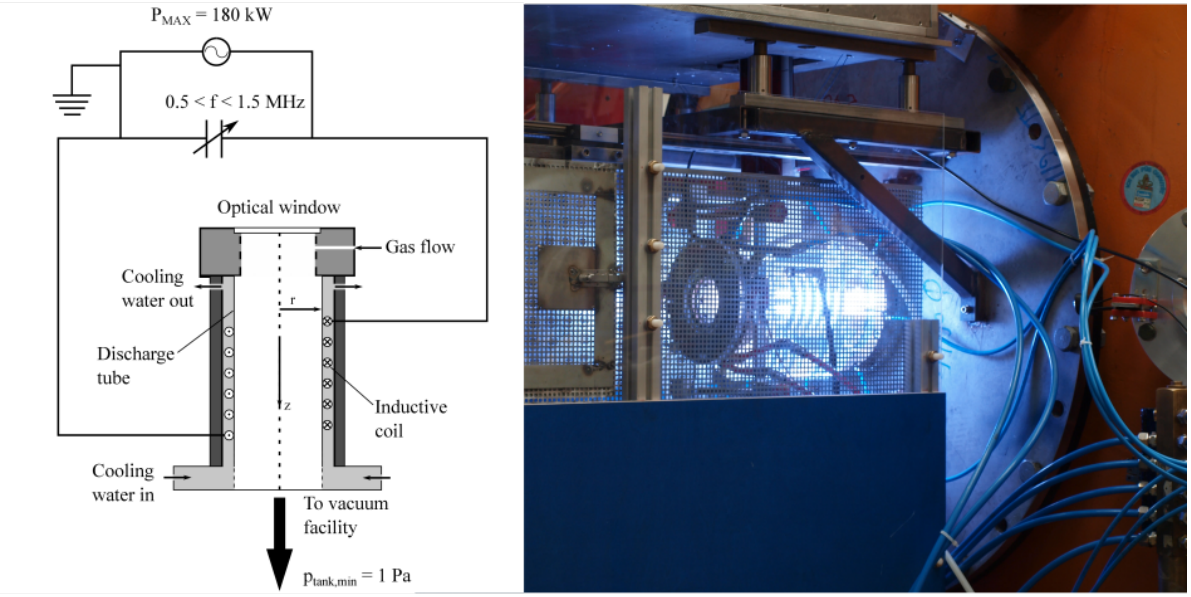

Figure 4.2: IPG7 schematic layout (left) and during operation with argon (right)

In this investigation, the Inductive Plasma Generator model 7 (IPG7) is used to compare the performance of the various propellants.

The IPG7 is the seventh iteration of IPG developed at IRS, with the primary application of the IPG family being planetary entry simulation. However, recently work has begun on a separate development branch into thruster applications in order to take advantage of their already established high-power capabilities [83–85]. The IPG7, as seen in Figure 4.2, is comprised of a quartz discharge tube surrounded by a 5.5 turn water-cooled inductive coil. This coil is connected to a resonant circuit in order to minimise power reflected from the plasma, with a set of seven 6 nF ($\pm$ 20 %) capacitors used to set the coil driving frequency (f_{RF}) between 0.5 and 1.5 MHz [50]. The number of coil turns also has a significant impact in the final value of f_{RF} [50, 59] and may be used to alter operational conditions. During the course of this work, both the coil geometry and capacitor configuration was kept constant, resulting in a coil driving frequency of 586 kHz. IPG7 is capable of operating at a maximum input power of 180 kW, though gas-specific behaviour often limits the true final value (see Section 4.2.3).

The discharge chamber of this thruster is 285 mm long with an outer diameter of 90 $\pm$0.2 mm. This tolerance ensures the roundness of the tube and an even distribution of stresses during operation. Using different wall thicknesses, the dielectric separation

between coil and gas can be altered without the need to modify the coil geometry. Propellant flow rates for this system are in the order of several g/s of air, translating to 50 - 200 ln/min on a volumetric basis. This thruster is mounted on the exterior of the tank due to the high applied coil voltages (> 7000 V [50]) presenting the risk of stray discharges. Placing the thruster inside the tank would also significantly decrease the coil driving frequency as a result of an increased current path.

The interaction between inductive coil and plasma can be modelled as an equivalent transformer system, shown in Figure 4.3. As discussed in Section 4.2.2, the plasma discharge exhibits its own electric and magnetic fields which react to (and interact with) those of the coil. The full system must therefore be considered when assessing thruster performance and interaction with the various propellants.

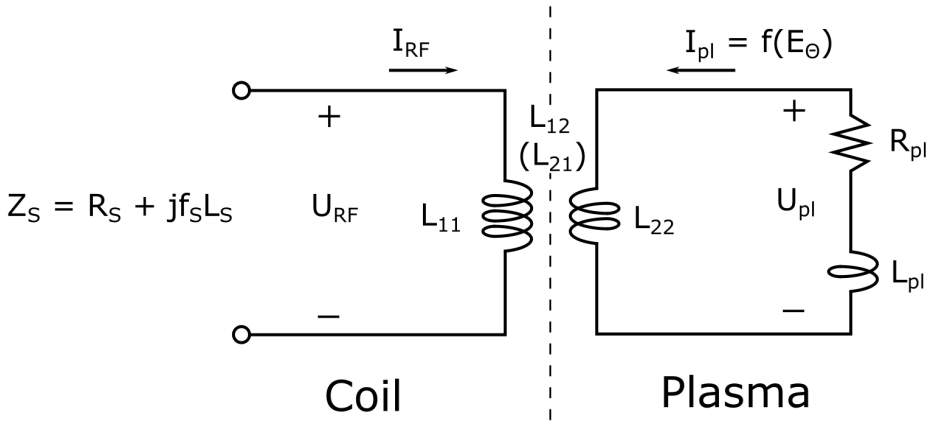

Figure 4.3: Coil and plasma modelled as equivalent transformer (adapted from [45])

The inductive coil in Figure 4.3, operating under potential U_{RF}, current I_{RF}, and impedance Z_S, is coupled to the discharge which itself displays a potential, current, and impedance of U_{pl}, I_{pl}, and Z_{pl}, respectively. Z_S is controlled by the matching circuit, with values for L_S (source inductance) and R_S (source resistance) modified during operation to match the impedance of the discharge. The complex descriptions of potential within the two circuits may be related by [86]:

$$\tilde{U}_{RF} = jf_{RF}\ L_{11}\tilde{I}_{RF} + jf_{RF}\ L_{12}\tilde{I}_{pl} \tag{4.1}$$

$$\tilde{U}_{pl} = jf_{RF}\ L_{21}\tilde{I}_{RF} + jf_{RF}\ L_{22}\tilde{I}_{pl} \tag{4.2}$$

where L_{11}, L_{12} $(= L_{21})$, and L_{22} are the coil-specific, coupling, and plasma-specific inductances, given by:

$$L_{11} = \frac{\mu_0 \pi \ b^2 N^2}{l_{pl,coil}} \tag{4.3}$$

$$L_{12} = L_{21} = \frac{\mu_0 \pi \ R^2 N^2}{l_{pl,coil}} \tag{4.4}$$

$$L_{22} = \frac{\mu_0 \pi \ b^2}{l_{pl,coil}} \tag{4.5}$$

where μ_0 is the permeability of a free space vacuum, b is the effective coil radius, N is the number of coil turns, $l_{pl,coil}$ is the incident coil-discharge length, and R is the effective discharge diameter (where R < b and b - R represents the dielectric separation between the coil surface and plasma volume, hereafter referred to as the tube wall thickness, t). As can be seen, the current within the two systems (as well as the resultant potential in the discharge and coil) are inherently linked, with one able to influence the other during operation. This coupling may only be achieved once the necessary azimuthal electric field (E_θ, see Section 4.2.2) strength has been established, related to the plasma current by:

$$I_{pl} = E_\theta l_{pl,coil} \sqrt{\frac{2\sigma_{DC}}{\mu_0 f_{RF}}} \tag{4.6}$$

where σ_{DC} is the DC electrical conductivity (used for high pressure discharges where the particle collision frequency is significantly greater than the plasma driving frequency [45]). Values for E_θ and σ_{DC} are directly related to the discharge regime displayed by the plasma volume, with negligible values indicating the presence of a capacitive discharge due to the dominance of the axial rather than azimuthal electric field [45]. Variations in these parameters can also be used to denote variations in the discharge ionisation degree and hence transitions between further inductive modes. It should be noted that Equation 4.6 is valid only for the inductive regime and for discharges in which the skin depth (δ, see Section 4.2.2) is significantly smaller than the discharge radius [45].

Due to the strong interaction between plasma and coil, discharge analyses must consider the impact of both equivalent circuits on one another. For example, the same coupling which allows electrical energy to be applied to the plasma (from the power supply via the coil) can also cause an overdraw of current and damage to the power supply unit. Electrons on the surface of the coil exert a force on electrons within the plasma volume, and are similarly influenced by the opposing force. As a result, large increases in the discharge electron number density (often linked to a transition between

discharge regimes [50]) cause an increase in coil current and hence and increase in applied electrical power [50]. While this interaction reaches an equilibrium quickly, such reactions occurring near the maximum input power of the supply system risk exceeding the safe operating boundaries and damaging the power unit. The force generated by electrons in the discharge depends on the initially applied power and the composition of the propellant and hence this effect can be instigated by varying propellant composition. It is thus necessary to understand interaction between the discharge and coil, as well as their influence on one another, in order to identify the limits in alternative propellant use.

4.2.2 Electromagnetic Discharge Characteristics

As discussed briefly in Section 2.4, electrodeless thrusters exhibit a number of electromagnetic discharge modes.

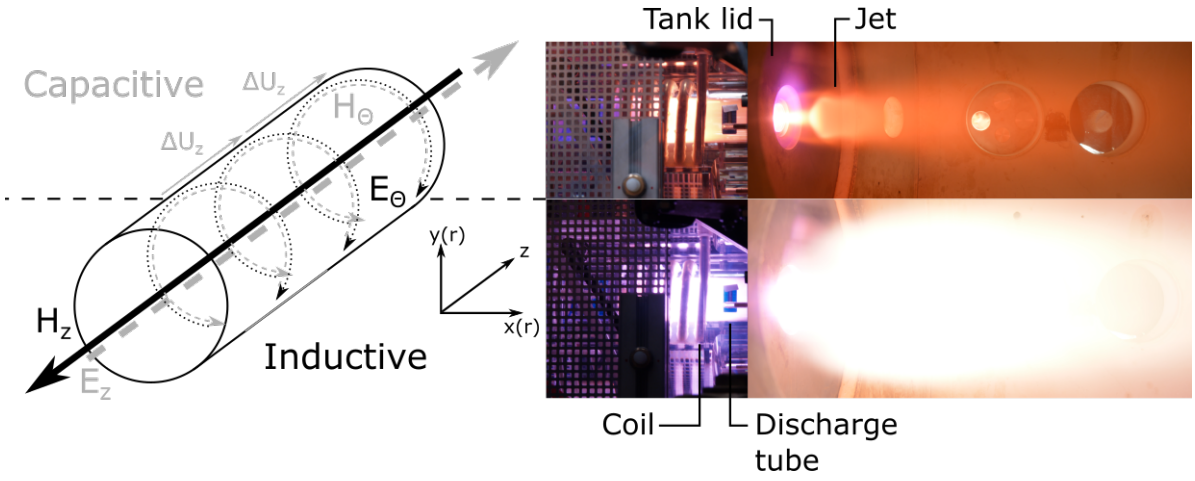

Figure 4.4: Electromagnetic field behaviour in inductive plasma generators and resultant flow characteristics with nitrogen (capacitive discharge, top; inductive discharge, bottom)

Figure 4.4 displays the capacitive and inductive mode field dominance as well as visible representations of the two regimes during nitrogen operation. Helicon modes are omitted at this stage due to their dependence on a particular waveform propagation rather than an adherence to a particular electromagnetic behaviour. The capacitive mode, commonly associated with low discharge pressures and input

powers [50, 70, 71, 87], is dominated by the axial electric field (E_z) produced by the potential difference between coil turns. An azimuthal magnetic field, H_Θ, accompanies this mode. This behaviour is most prominent in traditional coil designs, with other antenna geometries such as those seen in helicon sources [67] exhibiting a different potential distribution. A visible example of this discharge mode is seen in Figure 4.4. As the propellant passes through the discharge volume, it accumulates energy from the potential difference between coil turns, ΔU. This in turn increases the radiation intensity. While certain gases prove useful in displaying strong visual indications of this discharge, a comparison between argon and nitrogen shows that the intensity of these visible characteristics cannot be assumed universal amongst all gases.

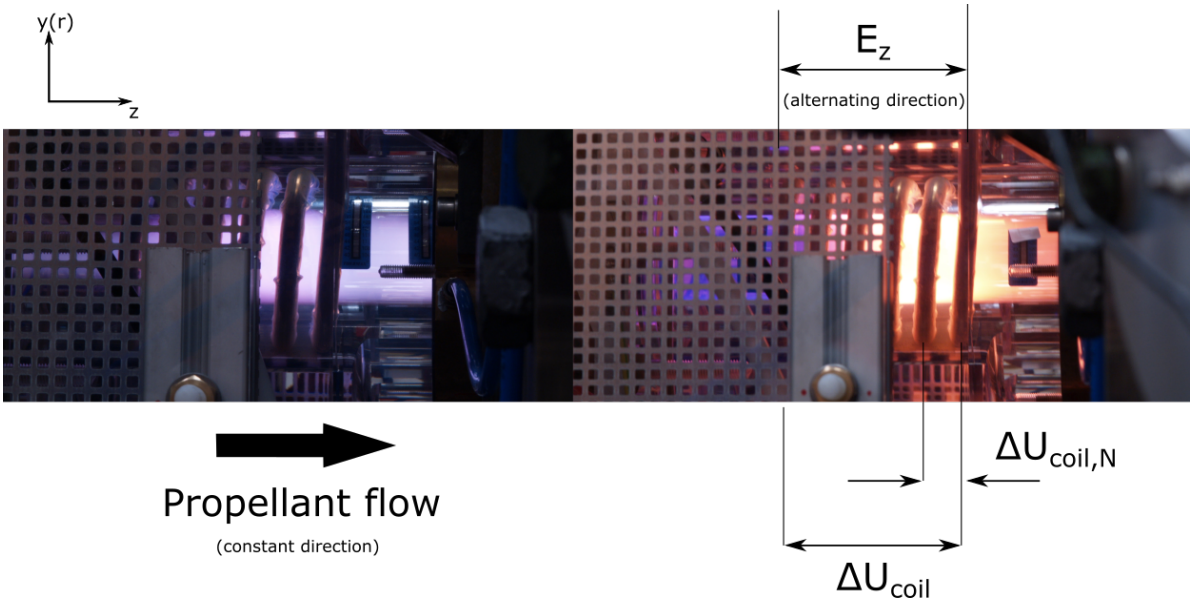

Figure 4.5: Comparison of visible radiation emitted by argon (left) and nitrogen (right) flows in the capacitive regime

The inductive mode is associated with higher discharge pressures and powers [50, 65, 87], dominated by an axial magnetic field (H_z) and an azimuthal electric field (E_Θ). It is this mode which is of significant interest for thruster applications, given its greater coupling efficiency between coil and plasma. The inductive mode has also been strongly linked to the helicon mode [67, 88], theorised as being responsible for the increased plasma density necessary to sustain helicon wave propagation. As seen in Figure 4.4, the increased energy in the inductive compared to the capacitive mode is evident (though again, such visible traits are not common amongst all gas species).

The electric and magnetic fields depicted in Figure 4.4 are those present within the plasma itself. The inductive coil exhibits similar field structures during the respective regimes, albeit with differing distributions. During inductive operation, the current flowing through the coil (which is restricted to an azimuthal path due to the coil geometry) generates an azimuthal electric field, $E_{RF,\Theta}$, and axial magnetic field, $H_{RF,z}$, exhibiting a maximum strength at the (internal) surface of the coil. The fields generated within the plasma are thus orientated in the opposite direction to the coil fields and display a different radial distribution due to the location of electrons within the flow. The relations between plasma and coil fields can be described through the Maxwell equations:

$$\nabla \times \vec{E} = -\mu_0 \frac{\partial \vec{H}}{\partial t} \tag{4.7}$$

and

$$\nabla \times \vec{H} = -\left(\epsilon_0 \frac{\partial \vec{E}}{\partial t} + \vec{J}\right) \tag{4.8}$$

where ϵ_0 is the permittivity of a free space vacuum and $\vec{J}$ is the current density. Separating the electric and magnetic field vectors into axial and azimuthal components yields [50]

$$\frac{\partial E_z}{\partial r} = -\mu_0 \frac{\partial H_\Theta}{\partial t} \tag{4.9}$$

$$\frac{\partial H_\Theta}{\partial r} = -\left(\epsilon_0 \frac{\partial E_z}{\partial t} + J_z\right) \tag{4.10}$$

for the capacitive mode and

$$\frac{\partial E_\Theta}{\partial r} = -\mu_0 \frac{\partial H_z}{\partial t} \tag{4.11}$$

$$\frac{\partial H_z}{\partial r} = -\left(\epsilon_0 \frac{\partial E_\Theta}{\partial t} + J_\Theta\right) \tag{4.12}$$

for the inductive mode. These equations provide the mathematical description of the coupling between axial and azimuthal components shown in Figure 4.4. The full derivations for the field equations are lengthy and well-covered in literature [50]. Using the coil magnetic field as the source of energy deposition (no heat transfer from other external sources [50]) and implementing the generalised form of Ohm's law for high-pressure plasma discharges ($\vec{E} = \sigma_{DC}.\vec{J}$) [45], Equations 4.11 and 4.12 may be

reformulated as [50]:

$$E_{\Theta}(r_0) = H_{RF,zMAX}\left(\frac{\sqrt{-2j}}{\delta\sigma_{DC}}\right)\left\{J_{B,0}^{-1}\left(\sqrt{\frac{-j}{4}}\frac{r_0}{\delta}\right)J_{B,1}\left(\sqrt{-2j}\frac{r_0}{\delta}\right)\right\} \tag{4.13}$$

$$H_z(r_0) = H_{RF,zMAX}\left\{J_{B,0}^{-1}\left(\sqrt{\frac{-j}{4}}\frac{r_0}{\delta}\right)J_{B,0}\left(\sqrt{-2j}\frac{r_0}{\delta}\right)\right\} \tag{4.14}$$

where $H_{RF,zMAX}$ is the maximum inductive coil magnetic field, δ is the inductive discharge collisional skin depth, $J_{B,0}$ and $J_{B,1}$ are the zeroth and first order Bessel functions, respectively, and r_0 is the radial position (taken as zero at the surface of the inductive coil [3]). As the capacitive regime displays poorer energy coupling and hence reduced thruster performance compared to the inductive regime, more detailed forms of Equations 4.9 and 4.10 are not required.

The coil magnetic field strength may be calculated as

$$H_{RF,z} = I_{RF}\frac{N}{l_{coil}} \tag{4.15}$$

where l_{coil} is the coil length (distinguished from the discharge length, $l_{pl,coil}$, in Section 4.2.1). The skin depth and DC electrical conductivity are given as

$$\delta = \sqrt{\frac{2}{\mu_0 f_{RF}\sigma_{DC}}} \tag{4.16}$$

and

$$\sigma_{DC} = \frac{|q^2|n_e}{\upsilon_{eff}m_e} \tag{4.17}$$

respectively, where q is the individual electron charge, n_e is the electron number density of the discharge, υ_{eff} is the effective collision frequency for momentum transfer between the electrons neutrals, and m_e is the individual electron mass. Therefore, for a fixed thruster coil geometry (ie N and l_{coil} constant), the strength of the inductive field components are dependent on parameters in both the coil and the discharge itself, yielding:

$$E_{\Theta}(r) = g_1(r, I_{RF}, f_{RF}, n_e, \upsilon_{eff})$$

$$H_z(r) = g_2(r, I_{RF}, f_{RF}, n_e, \upsilon_{eff})$$

These are the most important parameters when considering transitions between the capacitive and inductive discharge regimes, rather than the previous reliance on

[3] The change in coordinate orientation for r_0 as opposed to r (which has its zero-point defined at the tube axis centre) is due to r_0 being focused about the coil surface rather than the discharge tube

secondary parameters such as pressure and input power. The above relations will be applied to a single thruster coil geometry within the scope of this work.

Equations 4.15 and 4.17 quantify behaviour in the coil and plasma, respectively. Equation 4.16 therefore represents the interface between the two, with the skin depth acting as the coupling mechanism between coil and propellant. Figure 4.6 shows the discharge cross-section characteristic of the inductive regime. In this figure, H_z (being the coil component and acting in the opposing direction to $H_{RF,z}$) has been omitted for legibility purposes.

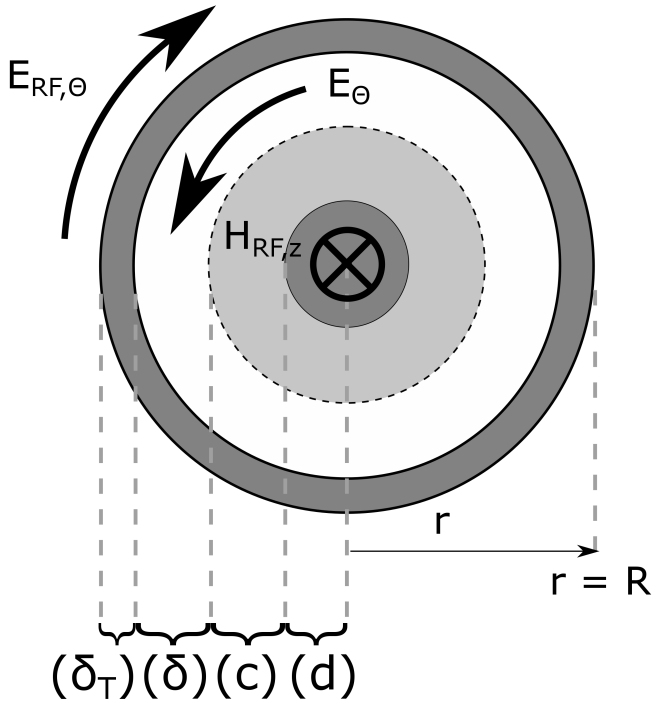

Figure 4.6: Discharge cross-section of an inductive discharge: δ_T, thermal boundary layer; δ, skin depth zone; c, thermal diffusion zone; d, cold core

The outermost region of the discharge is the thermal boundary layer, δ_T, which is the interaction zone between the discharge tube boundary walls and the plasma flow. This region is characterised by significantly lower temperatures and ionisation degrees due to the loss of particle energy to the cooled wall. It is also the zone through which convective heat flux from the plasma is transferred to the wall and recorded as the tube cooling power (see Section 4.2.3).

Adjacent to the thermal boundary layer is the skin depth zone which is of primary interest when assessing the discharge behaviour. The skin depth zone is where the vast majority of energy is coupled into the flow from the inductive coil. As the current in the coil is increased, so is the coil axial magnetic field strength, causing it to exert greater force on the charged particles as they traverse the thruster. Due to the alternating frequency (and polarisation) of the coil, electrons are rapidly accelerated with alternative azimuthal direction, colliding with heavy particles. This interaction drives the ionisation process, local plasma heating, and the formation of the plasma's azimuthal electric field, oriented in the opposing direction to the coil's field. The radially decaying strength of the coil axial magnetic field, combined with the aforementioned energy losses to the tube wall, generates a distinct zone in which this collisional (or Ohmic) heating can occur. This this is the major interaction zone between propellant and the coil, exhibiting the highest temperatures and degree of ionisation.
Heating past the skin depth zone occurs only through diffusion. Zone c represents this diffusion towards the discharge cold core, zone d.

As energy is coupled into the skin depth zone and subsequently transferred across the discharge cross-section my means of thermal diffusion, the size of these zones depend heavily on the thermal conductivity, specific heat capacity, and chemical composition of the propellant, as well as the local thermal energy. As the degree of ionisation (and hence electrical conductivity) of the discharge increases, the skin depth width decreases relative to the thermal boundary layer [45]:

$$n_e \uparrow, \quad \sigma_{DC} \uparrow, \quad \delta/R \downarrow$$

The optimal ratio between skin depth and total discharge radius (for collisional plasmas) is often cited as $\delta/\mathrm{R} = 0.57$ [45,50]. No such values are quoted for the other layers, though given they each represent zones of losses rather than of energy coupling (particular the thermal boundary layer), they should be minimised as best possible. As a result, it is not only the behaviour of the skin depth which is of interest in inductive discharges, but that of the thermal boundary layer as well. To better understand the discharge and its impact on thrust and specific impulse, both of these zones should be assessed. This includes their interactions with the coil and the discharge chamber wall.

4.2.3 Plasma-Wall Interactions

While the thruster discharge chamber is water-cooled, certain discharge conditions produce sufficient heat flux to exceed material limitations during operation. This was well-documented by Herdrich [50], who investigated the tube cooling power to failure for a series of discharge tubes wall thicknesses. Results from this investigation are shown in Figure 4.7.

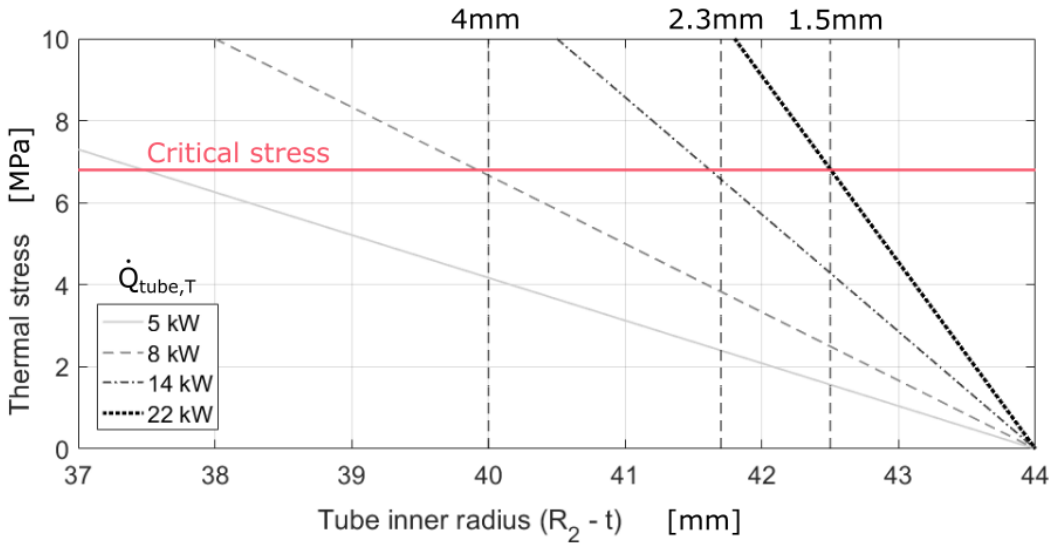

Figure 4.7: Tube cooling power at material failure point for various discharge chamber wall thicknesses (adapted from [50])

This study, which focused on oxygen, highlights the importance of tube wall thickness considerations. This drives the interest for investigating the impact of wall thickness on alternative propellants, particularly given their differing thermal conductivities. Tube cooling power ($\dot{Q}_{tube}$) is measured calorimetrically using temperatures of the tube cooling water flow and the water flow rate ($\dot{m}_w$) to give an integral value of the total thermal load:

$$\dot{Q}_{tube,T} = c_{p,w}\dot{m}_w\Delta T_w = \int_0^z \dot{Q}_{tube}(z)dl \tag{4.18}$$

where $c_{p,w}$ is the isobaric specific heat capacity of the cooling water, ΔT_w is the temperature difference of the cooling water before and after interaction with the discharge tube, and l is the length of the discharge tube. In the case of tube failure, the critical cooling power, $\dot{Q}_{crit}$, is assumed to be equal to that of heat flux passing through the discharge tube wall (with no additional coupling losses between tube wall and

cooling water). It should also be noted that due to the substantial variation in local heat flux with axial position, mechanical failure often occurs at a distinct axial position such that [89]:

$$\dot{Q}_{tube}(z) = \dot{Q}_{crit} = 2\pi\Delta l\kappa_{tube}\frac{\Delta T_{wall}}{ln(\frac{R_2}{R_2-t})} \tag{4.19}$$

where Δl is the finite tube section over which the breakage occurs, κ_{tube} is the thermal conductivity of the quartz discharge tube, ΔT_{wall} is the temperature difference between the inner and outer tube walls ($T_{wall,in}$ and $T_{wall,out}$, respectively), R_2 is the outer tube radius, and t is the discharge tube wall thickness. A graphical representation of the heat transfer between plasma and cooling water is shown in Figure 4.8.

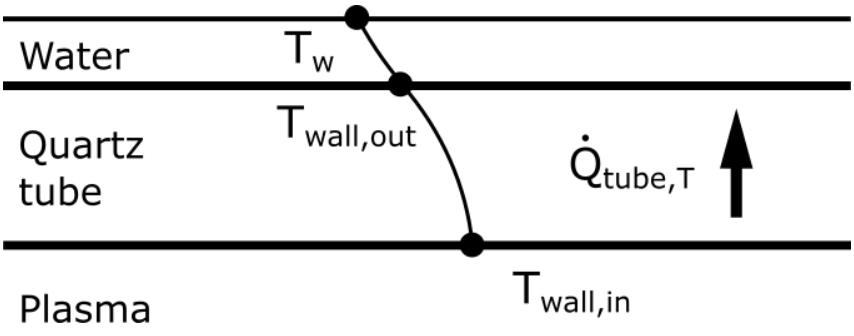

Figure 4.8: Heat transfer between plasma and cooling water

Tubes used within IPG7 share a common outer diameter, varying only in wall thickness as do previous IPG iterations such as those investigated by Herdrich [50]. As the tube thickness is increased, the temperature difference required to reach the critical tube stress decreases, causing breakages to occur at lower tube cooling powers.

$$t \uparrow, \quad \Delta T_{wall,crit} \downarrow, \quad \dot{Q}_{crit} \downarrow$$

Furthermore, increasing the tube thickness allows less thermal energy to be convected away from the walls by means of the water flow, increasing the inner tube wall temperature whilst decreasing the outer wall temperature. This in turn results in breakages occurring at lower thruster input powers and in potentially lower discharge regimes for particular gases.

$$t \uparrow, \quad T_{wall,in} \uparrow, \quad \Delta T_{wall} \uparrow, \quad \frac{\dot{Q}_{crit}}{P_{RF}} \downarrow$$

The primary difficulty in predicting local tube failures is the lack of knowledge regarding tube wall temperatures and the finite length, Δl, over which the critical cooling power is

exceeded. Of particular difficulty are estimates of the inner wall temperature, which is the result of convective interaction with the plasma:

$$T_{wall,in} = f_1(\dot{m}_{pl}, \bar{c}_{p,pl}, \bar{T}_{tra,pl})$$

where $\dot{m}_{pl}$ is the plasma mass flow rate and $\bar{c}_{p,pl}$ and $\bar{T}_{tra,pl}$ are the mean plasma specific heat capacity and translational temperature, respectively. The plasma mass flow rate considers all species within the flow, as both heavy particles and electrons can contribution significantly to wall heating. However, to date, no information as to the proportional contribution of the species is available.

Assuming heavy particles within the discharge volume are accelerated from heating only (thus neglecting magnetic acceleration), the mass flow rate of the plasma can be described in terms of the particle-specific flow density ($\rho = Mn/\hat{N}$) and the discharge area ($A = \pi(R_2 - t)^2$)) as:

$$\dot{m}_{pl} = \frac{Mn}{\hat{N}}\pi(R_2 - t)^2 u \tag{4.20}$$

where M, n, and u are the plasma molecular mass, number density, and bulk flow velocity, respectively, and $\hat{N}$ is Avogadro's number. Values of M and n vary significantly depending on the plasma composition. Hence the species-specific values, denoted by the subscript s, are used. All heavy particle and electron species are considered in this formulation. Expanding the terms of Equation 4.20 to consider all relevant chemical species within the flow gives

$$\dot{m}_{pl} = \frac{n\sum_s X_s M_s}{\hat{N}}\pi(R_2 - t)^2 u \tag{4.21}$$

where s is the species molar fraction. The mean specific heat capacity can be expanded to:

$$\bar{c}_{p,pl} = \sum_s X_s c_{p,s} \tag{4.22}$$

Thus taking the refined forms of $\dot{m}_{pl}$ and $\bar{c}_{p,pl}$ from Equations 4.21 and 4.22, the inner wall temperature may be described as:

$$T_{wall,in} = f_2(X_s, n, M_s, c_{p,s}, T_{tra,s})$$

Hence the inner wall temperature is dependent on the local chemistry of the plasma. The above formulae highlight the importance of the plasma composition on the wall heat flux. Furthermore, the translational temperature and thermal conductivity of each species

within the flow has a significant impact on the wall temperature and hence the tube cooling power recorded through the calorimetric method. This highlights the need for refined techniques to investigate the interaction between plasma and the discharge chamber wall. Once obtained, this information can be used to improve the heat management of future thruster designs.

Wall Thickness Variation

In addition to the gasdynamic interaction discussed above, the discharge tube wall also influences the electromagnetic behaviour of the discharge.

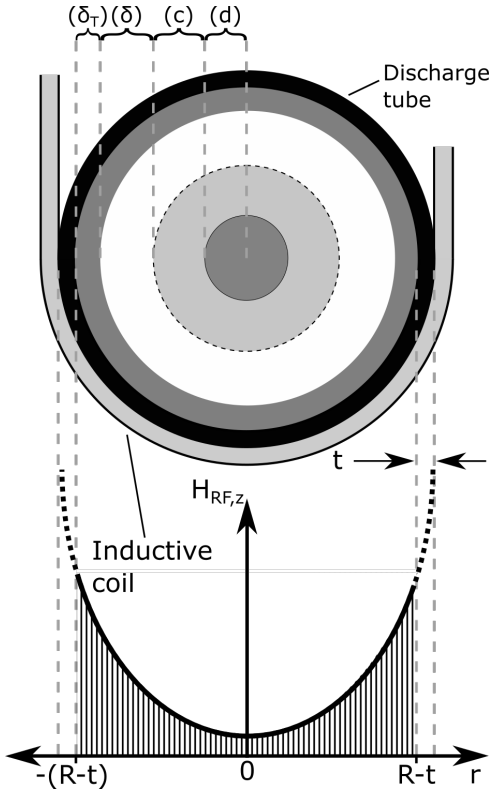

Figure 4.9: Influence of dielectric tube wall thickness on incident coil magnetic field strength (adapted from [90])

As seen in Figure 4.9, the dielectric material of the discharge tube wall acts to reduce the incident magnetic field strength of the coil on the plasma simply by occupying space displaying the greatest field intensity and confining the plasma to areas of lesser intensity. The net magnetic field to which the plasma is exposed is described as:

$$H_{RF,z} = 2\int_0^{R-t} H_{RF,z}(r)dr \tag{4.23}$$

with the significant decay of field strength with increasing distance from the coil surface resulting in a high sensitivity for small variations in the wall thickness.
Previous investigations into discharge sensitivity to variations in wall thickness have been conducted by Herdrich [50] and Nawaz and Herdrich [65]. These studies indicated better coupling with thinner tubes due to the increased net magnetic field strength applied to the plasma. However, these investigations assessed only oxygen and air, respectively. In this project, both monatomic and diatomic gases were tested with different wall thicknesses. During these tests, particular attention was given to the input power required for regime transitions and the energy coupling efficiency (see Section 4.3.2).

Discharge Tube Wall Temperature Distribution

Although wall temperature measurements are important in understanding the interaction between the plasma and discharge chamber, their measurement is challenging.

Direct measurements of the tube inner wall temperature present difficulties in accessibility and reliability. Any mechanical methods must first gain access to the wall within the discharge volume itself, a difficult task as the tube is a single component without breaks or connections, sealed at one end by the injector head. Furthermore, any intrusive methods would disrupt the flow and distribution of the plasma, with metallic probes presenting the further disadvantage of changing the interaction between coil-generated fields and charged particles within the discharge. Finally, the high temperatures exhibited by the plasma within the chamber require most materials to utilise dedicated cooling systems, resulting in prohibitively large structures for use within the volume.
Optical methods also suffer from limited accessibility, with only the quartz window embedded in the injector head offering unobstructed view and the high transmission of the quartz discharge tube itself offering no radiating surface for equipment such as thermocameras to take temperature readings from.

The environment surrounding the tube outer surface is significantly less hazardous than that in contact with the plasma, though is still subject to restrictions. The use of metallic objects near the coil is still prohibited due to their risk of interaction with the electric and magnetic fields. Furthermore, the pressure of the cooling water (0.6 MPa) surrounding the tube and coil can result in reasonable wear to equipment in sustained contact with it. Access to the tube from externally-mounted equipment is also difficult without significant modifications to the acrylic housing of the thruster.

Considering these factors, three investigative tools have been identified to provide complimentary assessments of the discharge tube wall temperatures; analytical calculations from integral heat flux measurement, adhesive thermometers attached to points on the tube outer surface, and investigations using thermally-reactive paint on the tube inner wall.

Analytical Heat Flux

The analytical calculation of the discharge tube outer wall temperature (using values of integral heat flux measured from the tube cooling circuit) involved simplifying the cooling water path around the discharge tube, seen in Figure 4.10, as well as the cross-section of the channel itself, seen in Figure 4.11.

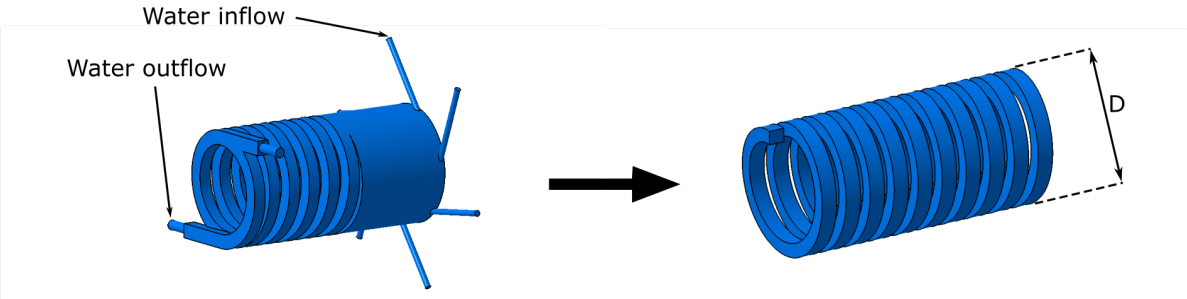

Figure 4.10: IPG laboratory cooling water volume (left) and simplification (right) (adapted from [91])

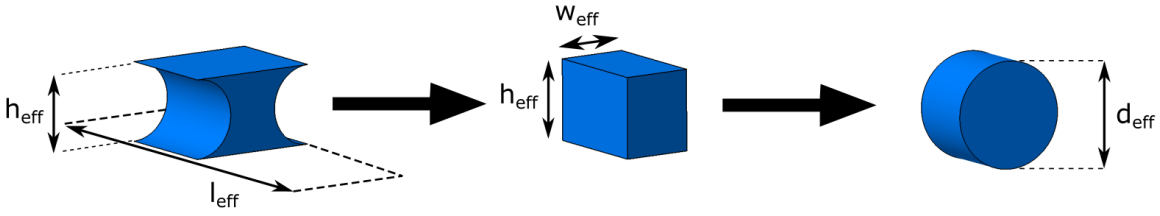

Figure 4.11: IPG cooling flow cross section simplification (adapted from [91])

The left-hand image in Figure 4.10 represents the flow of cooling water in the laboratory thruster. As the maximum tube heating occurs in the vicinity of the coil, the total cooling water volume was simplified to represent the helical path caused by the coil geometry. The central image in Figure 4.11 was used to calculate the interaction surface area between tube and cooling water ($A_{eff} = l_{eff} \times w_{eff}$), and the right-hand image was used for the flow field calculations (due to the equations' requirement for circular flow geometry [89]).

While a more detailed explanation of the numerical process is available in [91], the major component may be summarised as an iterative process of calculating the tube outer wall temperature using measured values of the tube cooling power and water temperature (T_w) at a given experimental condition. The outer wall temperature is calculated as

$$T_{wall,out} = \frac{\dot{Q}_{tube,T}}{A_{eff}\alpha_w} + T_w \tag{4.24}$$

where α_w is the heat transfer coefficient of the cooling water, given as

$$\alpha_w = \frac{\kappa_w Nu}{d_{eff}} \tag{4.25}$$

where κ_w is the thermal conductivity of the water, Nu is the flow Nusselt number, and d_{eff} is the cooling water channel diameter from the circular cross-section approximation. This model neglects radiative heat flux from the plasma due to a lack of data on the plasma temperature and emissivity, including the variation of these parameters along the tube axis. Future work on this model would benefit from the inclusion of radiative heat transfer, however it is out of the scope of this present work.

Calculating the cooling water Reynolds number (Re) for the various conditions tested, the flow was found to be consistently turbulent. Hence the Nusselt number for such helical, internally forced convection is given as [89]

$$Nu = \frac{\left(\frac{\zeta}{8}\right) RePr f_1}{1 + 12.7\sqrt{\frac{\zeta}{8}}\left(Pr^{2/3} - 1\right)} \tag{4.26}$$

$$\zeta = \frac{0.3164}{Re^{1/4}} + 0.03\left(\frac{d_{eff}}{D}\right)^{1/2} \quad , \quad f_1 = \left(\frac{Pr}{Pr_{wall}}\right)^{(7/50)} \quad , \quad Pr = \frac{c_{p,w}\mu_w}{\kappa_w}$$

where D is the inductive coil outer diameter (and hence cooling channel outer diameter), Pr and Pr_w are the flow Prandtl numbers calculated using the water and wall temperatures, respectively, and μ_w is the dynamic viscosity of the cooling water. The term f_1 is used to account for the wall temperature's influence on the cooling flow, with values of $\mathrm{Pr_{wall}}$ updated during each iterative cycle until a converged solution to Equation 4.24 is reached. A graphical representation of this process is displayed in Figure 4.12.

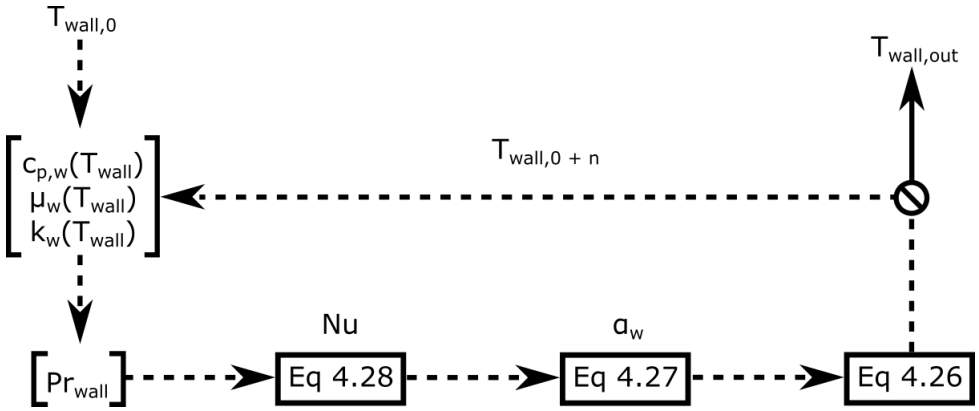

Figure 4.12: Iteration process to determine integral outer tube wall temperature

Using the calculated wall temperature, as well as material properties of the discharge tube, the inner wall temperature may also be calculated using

$$T_{wall,in} = \left(\frac{\dot{Q}_{tube,T}}{2\pi\kappa_{tube}l}\right) ln\left(\frac{R}{R-t}\right) + T_{wall,out} \tag{4.27}$$

where κ_{tube} is the thermal conductivity of the quartz discharge tube.

With the discharge tube heat flux and outgoing cooling water temperature acting as inputs to this method, potential errors within stem from measurements of the water mass flow rate and inflow/outflow temperatures, as seen in Equation 4.18. Since $\delta T_w < 6$ K (in order to remain below the critical heat flux), variations in the water specific heat capacity are less than 0.08 %. Hence $\mathrm{c_{p,w}}$ is treated as a constant. Measurements of $\dot{m}_\mathrm{w}$ were recorded using a Siemens MAG 5000 electromagnetic mass flow meter, with an accuracy of ± 0.4 % of the total flow rate. The main source of measurement error is that resulting from the Omega Pt100 thermometers, with a resolution of ± 0.15 K for the

temperature range investigated. The magnitude of Pt100 errors increase with temperature according to $(1/3)(0.3 + 0.005T_w)$, where T_w is given in K [92]. These errors result in heat flux variations of $\pm$ 0.286 kW, assuming steady discharge conditions. However, the stability of the discharge varies greatly depending on the propellant and input power. Some conditions exhibit instabilities on the same time scale of the Pt100s (3 s) and may significantly increase the range of errors.

This integral method is limited in its accuracy for particular discharge conditions. However, when combined with additional, spatially-resolved measurement techniques, these calculations may assist in providing a more detailed understanding of the tube wall temperature during operation.

Adhesive Thermometers

To provide improved resolution of the variation of tube outer wall temperature, adhesive thermometers were applied as seen in Figure 4.13. These thermometers, made from non-metallic materials, are designed so as not to interact with the electric or magnetic fields surrounding the thruster. Despite these design considerations, some degree of interaction between thermometers and the inductive coil is still observed. This is discussed in the results of this project (Section 5.5). When the tube surface temperature exceeds a given threshold, the organic fluid within the display cells changes colour to indicate the surface temperature.

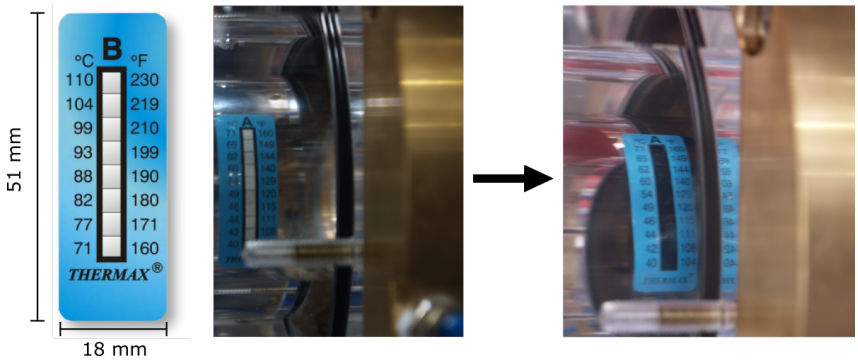

Figure 4.13: Adhesive thermometers on the IPG7 discharge tube prior to (centre) and following (right) experiments

The accuracy of the display cell fluid with respect to its indicated temperature is dependent on the temperature range. Combined with the difference between adjacent cell activation, associated errors of the different thermometer classes are listed in Table 4.2.

Table 4.2: Adhesive thermometer ranges and accuracies [93]

Class	T_{min} [K]	T_{max} [K]	ΔT [K]
A	313	344	$\pm$ 7
B	350	400	$\pm$ 7.5
C	405	455	$\pm$ 10
D	461	522	$\pm$ 12

As these thermometers are resistant to moderate pressure water flows, placement on the tube exterior (and hence in direct contact with the cooling water flow) has not been observed to compromise the measurement. However, the maximum endurance temperature of these thermometers ($\approx$ 600 K [94]) is significantly below the expected plasma temperature within the discharge. This prevents thermometers from being applied to measure the inner wall temperature directly. While both reversible and irreversible variants of these adhesive thermometers are available, the irreversible design was chosen for these experiments. This allows more detailed post analysis of a given maximum heat flux and removes hazards of monitoring strips at close proximity during operation. Altered convection over the surface of the tube (and hence measured heat flux) due to the thermometer's presence may be neglected due to its thin-layer construction. Materials used in the various layers of the thermometer (polyester, Kaladex, acrylic, and paper [93]) are constructed as thin layers in the order of 10^{-5} m, making their heat transfer coefficients negligible in comparison to the quartz surface. Secondary electron emission is considered negligible due to the separation of the thermometer from both the coil and plasma by Teflon insulation and the dielectric tube material, respectively.

The application of these thermometers allows spatially-resolved temperature measurements to be performed, representing an improvement over the integral approach. However, the resolution of this technique is restricted in that the surface temperature displayed is the maximum under the adhesive area of the thermometer (51 mm $\times$ 18 mm). Furthermore, thermometers in positions where access to cooling water is restricted (ie too close to point of contact between coil insulation and discharge tube) are exposed to excessive temperatures and causing significant damage (as will be discussed in Section 5.5). As such, there are limits on the number of thermometers

which may be applied. The measurement positions used in experiments are shown in Figure 4.14.

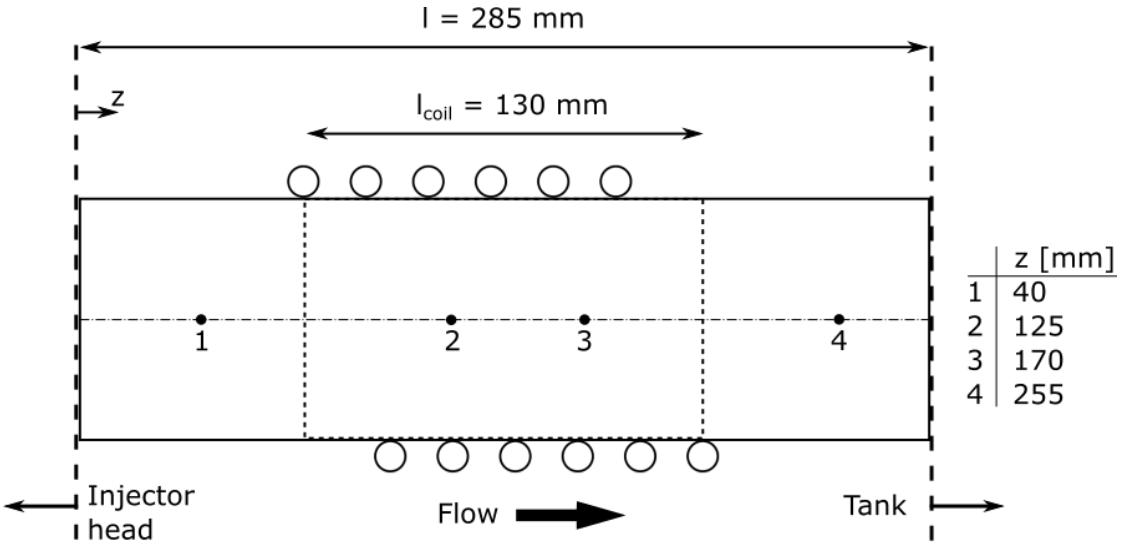

Figure 4.14: Adhesive thermometer placement

Thermal Paint

In order to increase spatial resolution and obtain direct information on the inner wall temperature, a thermally-reactive paint suited to high-temperature gas flows [94] was applied to the inner surface of a 3 mm discharge tube. This application process must be performed by qualified personnel using specialist facilities due to the high toxicity of the paint thinning agent. Following exposure to the plasma, discreet, irreversible colour bands allow post-test analysis of the tube wall temperature in a similar fashion to the adhesive thermometers. An image of the tube prior to testing is shown in Figure 4.15. Due to limitations on the availability of this paint, other tube thicknesses were not tested.

Figure 4.15: Discharge tube (3 mm) coated internally with thermally-reactive paint and covered externally with adhesive thermometers (adapted from [91])

While estimates of the expected transition temperatures are provided with the paint upon acquisition, in-house calibration is preferable in order to increase the accuracy of interpretation. In this way, the appearance of the paint may be documented at temperature intervals more suited to the particular application. Given the temperature range of the paint ($<$ 1100 K), 50 K was selected as an appropriate resolution for temperature zones in the paint to be identified following testing. Finer scales are also possible, though would make image dicretisation more difficult and time-intensive due to the similarity between colour bands. To produce reference paint colouration cells, a series of quartz tubes were treated with the paint and heated to the desired temperature in a Nabertherm HT16/16 furnace. By increasing the temperature gradually in the furnace, the desired temperatures could be reached to $\pm$ 5 K accuracy. The results of this calibration process and the subsequent reference colourations are displayed in Figure 4.16 and Table 4.3. To differentiate between temperature zones following tube testing, these colours were imported into MATLAB and the post-test tube processed in a dedicated script. By measuring the colour value of each calibration cell, the error associated with this technique is the sum of the scale used to produce the reference cells and the error in the furnace itself, yielding $\pm$ 55 K.

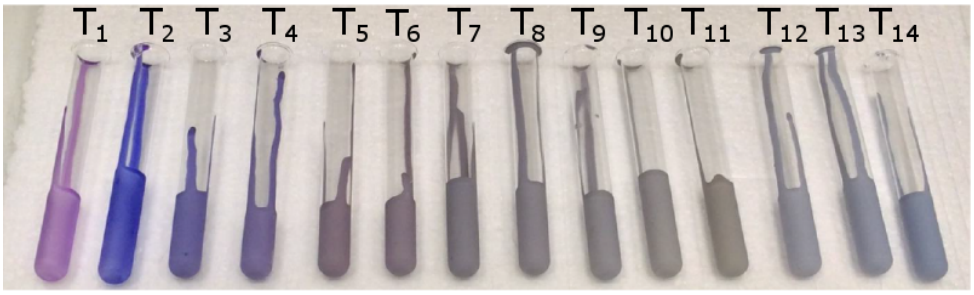

Figure 4.16: Calibrated colour cells for thermally-reactive paint (adapted from [91])

Table 4.3: Thermally-reactive paint calibration transition temperatures

T_1 [K]	T_2 [K]	T_3 [K]	T_4 [K]	T_5 [K]	T_6 [K]	T_7 [K]
<353	423	473	523	573	623	673
T_8 [K]	T_9 [K]	T_{10} [K]	T_{11} [K]	T_{12} [K]	T_{13} [K]	T_{14} [K]
723	773	823	873	923	973	1023

As can be seen, the maximum range of the thermal paint (1023 K = 750 °C) limits the discharge conditions which may be investigated using this technique. Contact with gas

temperatures above this limit results in destruction of the paint, and hence power must be applied gradually to the thruster (< 1.5 kW/s) while monitoring the temporal behaviour of the paint closely. Results from the adhesive thermometer method discussed previously were used to select an appropriate discharge condition to be assessed using the paint (see Section 5.5). Other considerations such as chemical reactivity of the plasma were also deemed important. Propellants containing oxygen were excluded to avoid oxidisation of the paint and its influence on the results.

Summary

The combination of these three techniques was used to establish a more thorough understanding of the distribution of wall temperatures (inner and outer) of the discharge chamber. This information provides the means to better understand the mechanisms behind chamber failure due to thermal loads and to improve future thruster designs.

4.3 Thruster Performance and Characterisation Techniques

The thruster performance was assessed through the measurement of thrust (and resultant calculation of I_{sp} using $\dot{m}$), thermal power, and efficiency (thrust and thermal) for the various propellants. Investigations into the discharge behaviour and exhibited regimes were conducted by assessing the inductive coil current and discharge skin depth.

4.3.1 Thrust Measurement

Thrust is one of the primary performance metrics used to assess propulsion systems, determining the time taken to perform manoeuvres and accelerate (or decelerate) the spacecraft.

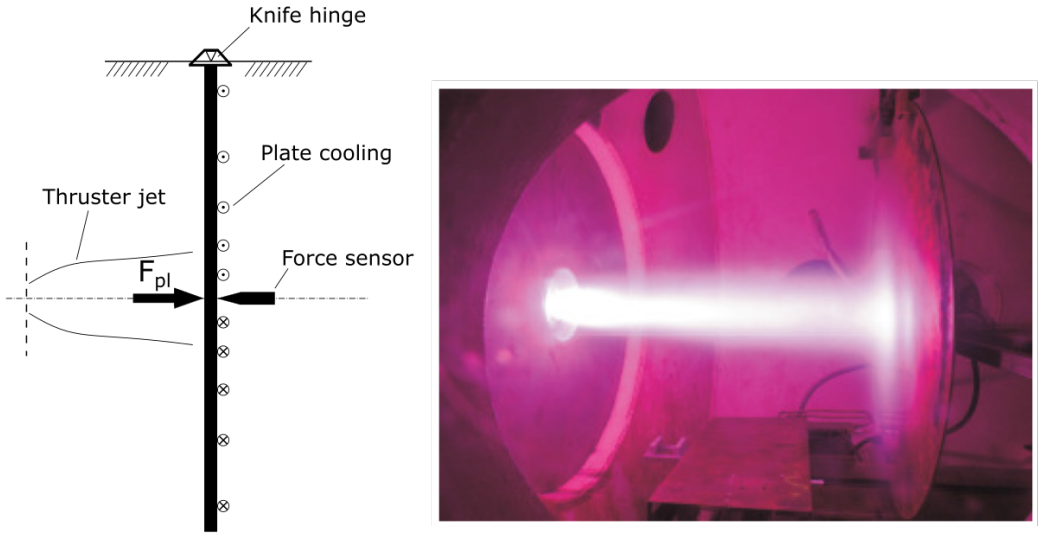

Figure 4.17: Baffle plate layout (left) and operational example with hydrogen [59] (right)

Due to the mounting of the thruster on the exterior of the tank a baffle plate assembly [95] was used in favour of a thrust balance to measure thrust during operation. An image of the baffle plate assembly in operation is shown in Figure 4.17. The baffle plate measures the force of plasma incident on the frontal surface by means of a ME-Messsysteme KD40s force sensor [96]. While the plate has been constructed with a sufficiently large diameter to capture the entire jet exiting the thruster, it is still prone to uncertainties which must be considered when assessing the accuracy of the results.

The two most significant error sources are the noise generated by water flow through the plate cooling pipes and by the propellant flow itself. Due to the high operating pressure of the cooling water (1.6 MPa), turbulence in the water flow causes vibration of the plate. While the cooling pipes are arranged in a counter-coaxial pattern to minimise momentum in any one direction, these vibrations are still significant and translate to noise measured by the force sensor. Inaccuracies caused by the propellant flow are a result of recirculating flow around the plate edges. In order to quantify the impact of these factors, a calibration stand consisting of three distinct mass disks (0.151, 0.149, and 0.145 kg) is used in order to apply a nominal load and assess the variation of force measured. This may be performed dynamically during testing as well as at set conditions to isolate particular influences [4]. The results of these calibrations are seen in Table 4.4.

[4]The calibration stand applies the masses in series by means of a retractable spindle. The force sensor may also preloaded, forcing it into contact with the plate by means of a small motor. This may be used to produce an additional, consistent offset before masses are applied.

Table 4.4: Baffle plate calibration conditions and results

Configuration	p_{tank} [Pa]	Water	Error [N]
1	101.32×10^3	-	± 0.749
2	101.32×10^3	✓	± 0.767
3	1.50	-	± 0.431
4	1.50	✓	± 0.729

As may be seen, the effect of cooling water has a significant impact on thrust measurements under vacuum conditions. This noise almost completely negates the error reduction obtained by removing ambient air contact with the plate. Cold gas measurements were also performed under evacuated tank conditions, with no discernible difference between forces produced by gas flow and those owing to the application of calibration mass. The resulting accuracy of thrust measurements using the baffle plate technique is estimate to be ± 0.729 N. This includes the ± 0.05 N error inherent to the force sensor itself. This total error is within an acceptable margin for the scale of thrust measurements performed in this research (0 - 10 N). This baffle plate design has previously been calibrated against a dynamic thrust stand [59] in order to account for factors such as the accommodation coefficient. This uncertainty is included in the total error.

The jet specific impulse is also derived from the measured thrust using:

$$I_{sp} = \frac{F}{g_0 \dot{m}_{pl}} \tag{4.28}$$

where g_0 is standard gravity and $\dot{m}_{pl}$ is the plasma mass flow rate, taken to be equal to that of the cold gas inflow since no accumulation occurs within the discharge volume. Specific impulse is used to determine the maximum velocity of the spacecraft as a result of the propulsion system (hence excluding gravity-assist manoeuvres). Thrust efficiency is used assess amount of thrust produced by a particular propellant considering its mass and the thruster input power. This is calculated as:

$$\eta_F = \frac{F^2}{\dot{m}_{pl} P_{RF}} \tag{4.29}$$

where P_{RF} is the RF input power of the IPG7 at the coil, taken as 75 % of the power supply anode power (P_A) due to efficiency inherent to the power supply triode arrangement [82].

This efficiency is not to be confused with the system thermal efficiencies discussed next in Section 4.3.2.

4.3.2 Thermal Power Measurement

While the primary objective of EP systems is to convert electrical power into thrust, analyses of the thermal power in electrothermal systems help to assess the coupling between coil and propellant. Furthermore, the magnitude of thermal power produced varies significantly with the propellant, with certain discharge conditions risking damage to the thruster. An understanding of the thermal power hence assists in thruster design and mission planning.

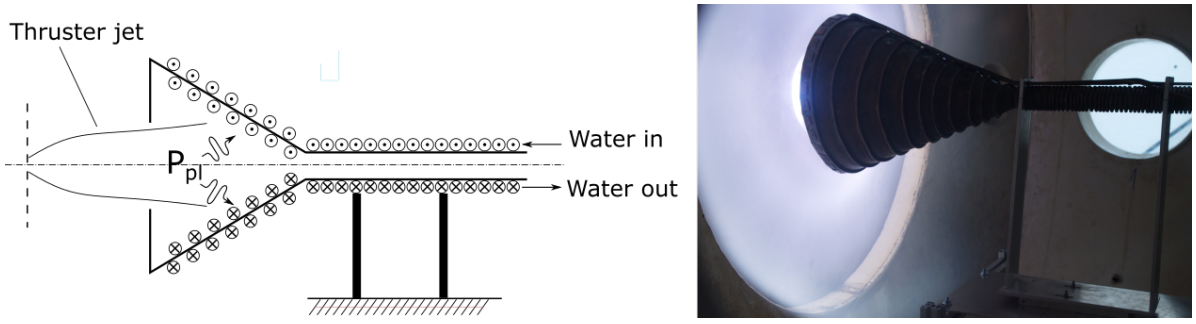

Figure 4.18: Cavity calorimeter layout (left) and during operation [90] (right)

Jet calorimetric thermal power (P_{pl}) is measured using the cavity calorimeter [50] shown in Figure 4.18. In these measurements, the same process is applied as that used to obtain the discharge tube heat flux, combining the flow rate of water through the calorimeter with the increase in water temperature. The same models of mass flow meter and thermometer are used in these measurements, resulting in a final accuracy of $\pm$ 0.09 kW (owing to a greater range of measurement temperatures and hence greater relative resolution) for stable discharge conditions. However, as in the case of tube heat flux, measurements taken using the calorimeter are influenced greatly by oscillations in the plasma.

The calorimeter is comprised of a double-cooled cavity shell with a 125 mm inlet diameter designed to capture the entire thruster jet. However, differences in the jet and tank pressures cause expansion of the flow with increasing distance from the thruster

exit, potentially exceeding the inlet diameter for certain flow conditions. For this reason, the calorimeter is placed as close as possible to the thruster outlet (without influencing the coil discharge) to mitigate flow losses. The calorimeter was placed at a distance of 0.11 m from the thruster outlet for these experiments. This distance has been shown to result in good capture of the flow volume without adversely affecting the discharge itself (though electromagnetic interference) or the tube pressure [50].

The thermal power measured using the calorimeter is combined with the integral tube cooling power from Equation 4.18, as well as the electrical input power, to yield the total thermal and effective thermal efficiencies of the thruster, given as:

$$\eta_{th} = \frac{P_{pl} + \dot{Q}_{tube,T}}{P_{RF}} \tag{4.30}$$

$$\eta_{th,eff} = \frac{P_{pl}}{P_{pl} + \dot{Q}_{tube,T}} \tag{4.31}$$

The distribution of thermal power between tube and jet is an important measure of propellant utilisation. In the same way that kinetic, rather than thermal, energy is the desired outcome of operation, so too is the effective transfer of energy from the discharge volume to the exiting flow. Without an effective transfer process, energy is retained in the discharge volume and the ultimate performance of the thruster is reduced, despite high values of total thermal efficiency. As such, high values of effective thermal efficiency should be sought in addition to total thermal efficiency.

4.3.3 Inductive Coil Current Measurement

As discussed in Section 4.2.2, the electromagnetic regime of the discharge is heavily dependent on coil parameters f_{RF} and I_{RF}. In order to measure these parameters during operation, a Hofer-Noser Karrer (HOKA) probe [97] is applied to the inductive coil, as seen in Figure 4.19. The HOKA probe measures the current passing through the coil section it is applied to (ΔL_{coil}) by means of the local, azimuthal magnetic field that is generated. During these experiments, the HOKA probe measured current at the coil end closest to the vacuum chamber. The measured signal is polarised with the direction of current circulation, allowing measurements of AC currents with operating frequencies up to 4 MHz. The maximum current amplitude measurable using this probe is 2 kA, with

an accuracy of ± 30 A. The current measured using the HOKA probe, I_{HOKA}, is equivalent to I_{RF}.

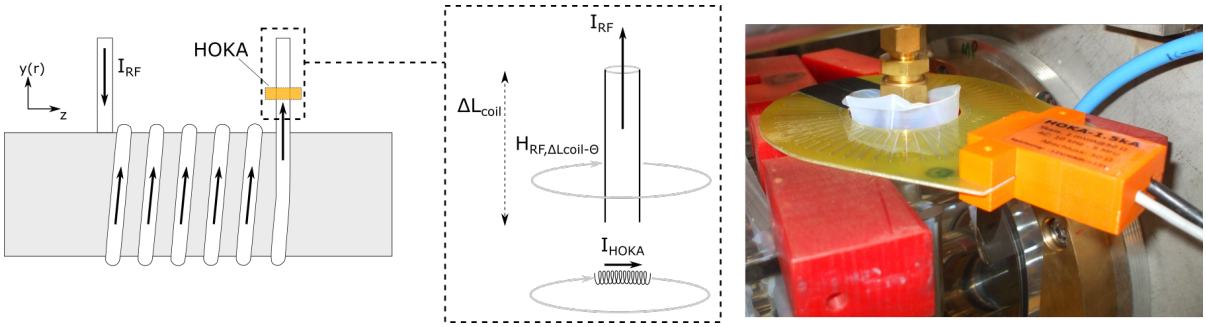

Figure 4.19: HOKA operating principle and probe installed on IPG7

Figure 4.20 shows a typical output from the HOKA probe converted to Root Mean Square (RMS) values (to account for the alternating polarity). This shows the capacitive discharge mode, with the coil current quickly reaching its maximum as the capacitors discharge before gradually reducing before the following cycle. This behaviour occurs at one of the power supply characteristic frequencies, f_{cyc}, which is the result of the full-wave rectifier and capacitor arrangement of the power supply. This is not to be confused with the coil driving frequency, f_{RF}, produced by separate capacitors in the resonant circuit. This frequency is also captured by the probe, with a Fast Fourier Transform (FFT) allowing analyses of the prominent characteristic discharge frequencies to be performed.

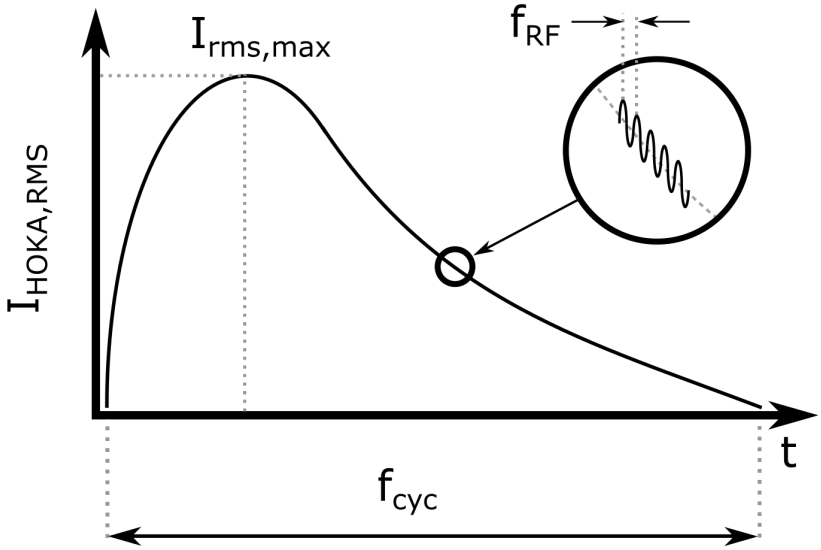

Figure 4.20: Typical HOKA output signal in the capacitive regime

Improving on previous campaigns using the HOKA probe, this thesis reports on a technique to discretise discharge cycles and assess variations in the coil current and driving frequency. This discretisation process, as shown in Figure 4.21, splits the discharge cycle into distinct time intervals where a local FFT can be performed and characteristic frequency obtained. For this investigation, discharges were separated into 100 intervals, representing a compromise between resolution and computational time. The ability to temporally resolve the discharge is of particular interest when investigating interactions between the plasma and coil (Section 4.2.1). The ability to track this interaction during the discharge cycle also allows the stability of the discharge to be assessed, as is detailed in Section 5.2.

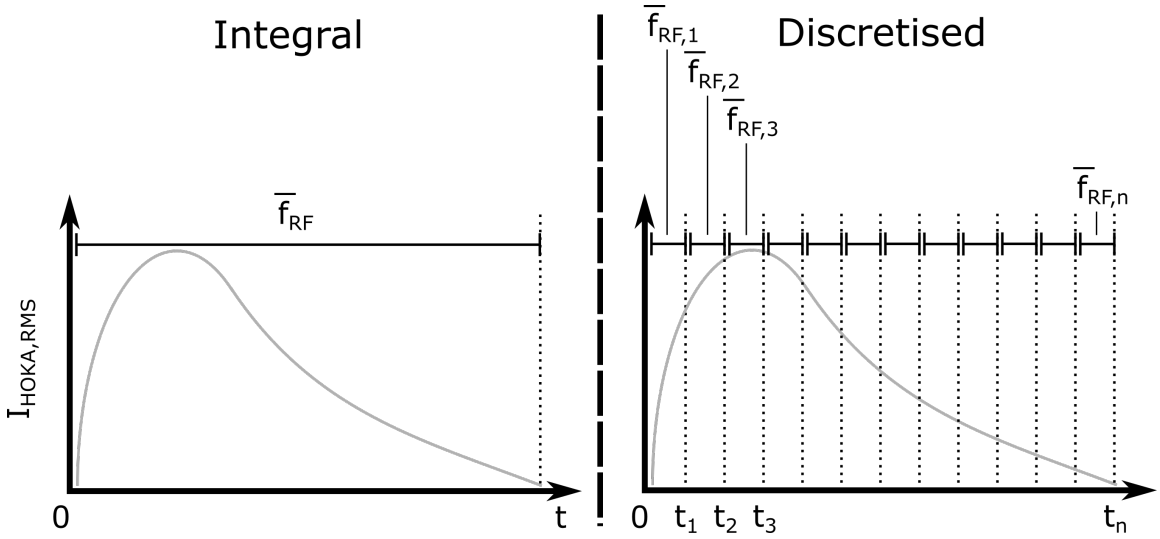

Figure 4.21: Determination of discharge characteristic frequency using the previous (left) and discretised (right) approaches

4.3.4 Visible and Magnetic Skin Depths

The skin depth is the fundamental characteristic of inductive coupling between the coil and plasma. It is dictated by the electron population within the discharge volume, though may also be visualised through the interaction between electrons and heavy particles. Figure 4.22 displays discharge cross sections for various gases tested. Note that the non-homogeneity for the CO_2 discharge is due to placement of the camera and not behaviour within the discharge chamber. It is clear from the intensity distributions in this image that the effects of the skin depth are clearly visible for a number of propellants.

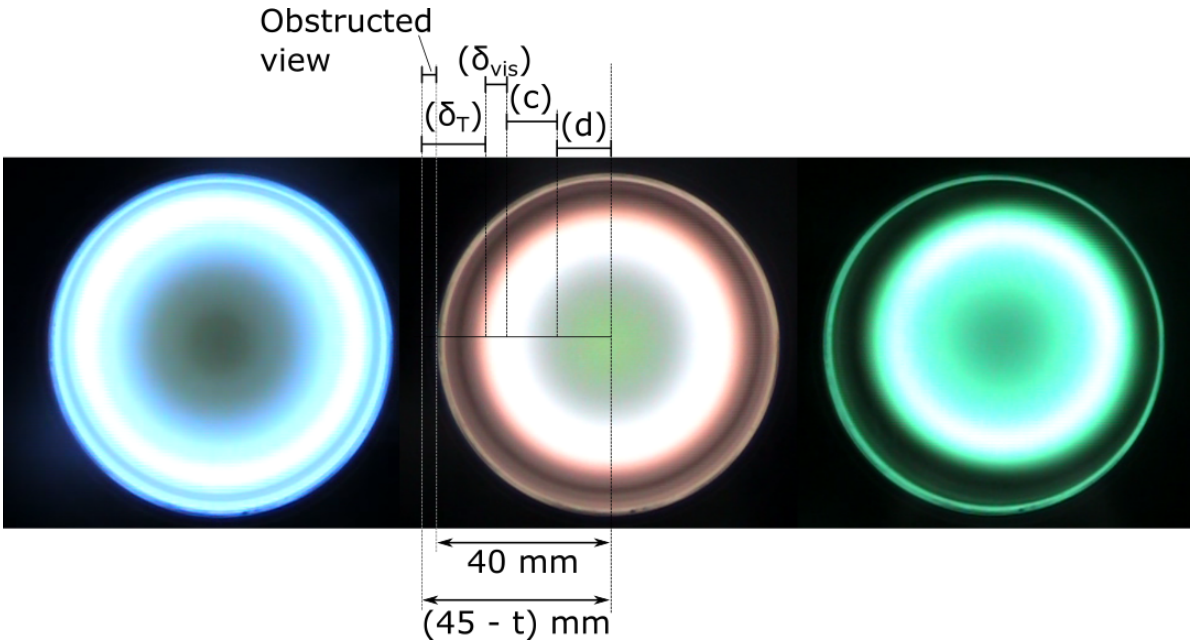

Figure 4.22: Visible skin depth for Ar (left), N_2 (centre), and CO_2 (right) inductive operation

This strongly radiating zone, termed the visible skin depth (δ_{vis}) is strongly linked to the true discharge skin depth (δ). However, not all energy from the electrons is transferred to heavy particle excitation and hence the visual method under-predicts the true skin depth. The intensity of this radiation is also highly dependent on the propellant and may not be measurable for all gases. Another way in which the true skin depth can assessed is by measuring the magnetic field distribution of the discharge. As the plasma magnetic field strength is dependent on the plasma azimuthal current, and hence electron number density [45], variations in the coil-generated field can be used to determine the plasma component. Values obtained using this method are termed the magnetic skin depth (δ_{mag}). As power is coupled into the plasma via the skin depth, obtaining information on the skin depth through either of these methods hence provides useful insight into the coupling of coil power to heavy particles, which are themselves responsible for thrust production. For this reason, comparisons of the true, visible, and magnetic skin depths were performed using numerical methods (discussed in Section 4.4) and experimental methods.

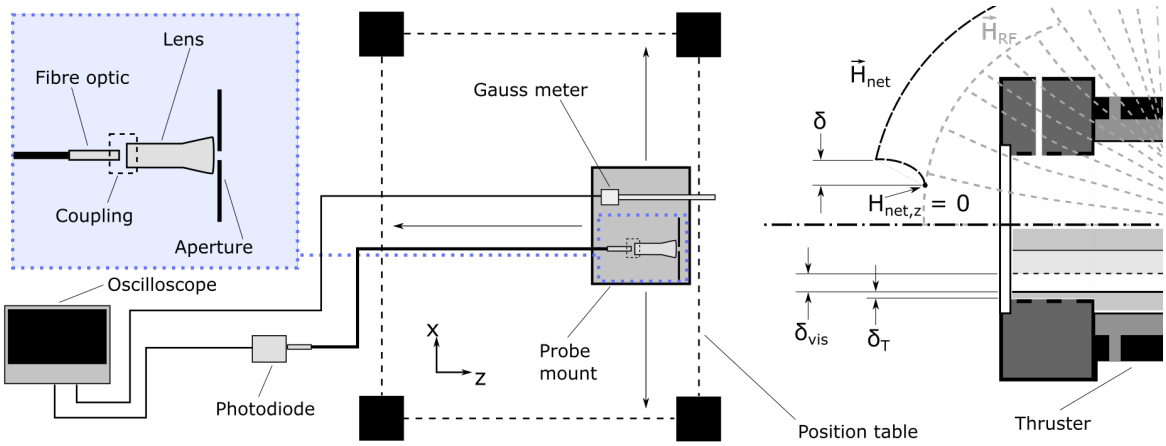

Figure 4.23: Skin depth investigation setup

Measurements of δ_{vis} and δ_{mag} were performed using the apparatus seen in Figure 4.23. A photodiode (Thorlabs DET-200 [98]) was used to record radial profiles of the relative light intensity. By normalising the intensity of the light recorded, the inner edge of the visible skin depth could be identified as the point of peak intensity. The outer edge (boundary between skin depth and thermal boundary layer) was then defined to begin once intensity was less than 90 % of the peak value. A Gauss meter (Projekt Elektronik FM 302 [99]) was used to measure the axial magnetic field strength. By comparing the magnetic field distribution during the capacitive and inductive regimes, the distance over which the plasma field disrupted the coil field is used to denote the magnetic skin depth.

The two-axis linear system allows both axial and radial profile measurements behind the thruster injector head to be performed. The range of this system is 0.210 and 0.290 m in the x and z-directions, respectively, though visual access to the discharge is limited (due to the geometry of the injector head) to a radius of 0.040 m about the centre axis. Since the photo diode focuses on relative, rather than absolute, measurements of radiation intensity, its distance from the discharge is not as critical as that of the Gauss meter. Measurements reported on in this thesis were performed at a distance of 0.120 m from the thruster, with the aperture placed before the fibre optic and lens used to increase the measurement depth of field and spatial resolution. The Gauss meter probe tip was positioned 0.177 m from the inductive coil at its nearest point (0.020 m from the thruster injector head).

The accuracy of the linear system is $\pm$ 10^{-5} m and the reference coordinate system of the drive system was recalibrated before each experiment using the control software. The accuracy of the Gauss meter is < 0.1 % [99].

As previously discussed, measurements of δ_{mag} are more accurate δ_{vis} when assessing the discharge behaviour of the thruster. However, the reduction of magnetic field strength with increasing distance from its source is significantly greater than that of visible radiation, subjecting measurements of δ_{mag} to significant spatial dependencies. The degradation of magnetic field strength may be described using the the Biot-Savart law [100], given as

$$H_z(z) = C_H \frac{1}{2} \frac{R^2 I_{RF}}{(z^2 + R^2)^{\frac{3}{2}}} \tag{4.32}$$

where C_H is a correction factor (for this case equal to 3.8923) used to calibrate the Gauss meter. From this relation it is clear that measurements of H_z taken at a significant distance from the discharge are considerably weaker, reducing the capacity to determine δ_{mag}. In addition to this, the maximum capture frequency of the Gauss meter used in these experiments is 100 kHz, significantly lower than the thruster driving frequency of 586 kHz. As a result, certain transient behaviour of the discharge may not be captured with the magnetic approach. Despite these restrictions, the use of magnetic field strength to determine values of δ_{mag} presents the distinct advantage of being gas-independent, depending only on electrons in the discharge volume. In this way, the reliance on particular radiating species is removed.

Due to the construction of the setup, measurements of the visible radiation and local magnetic field strength may be performed simultaneously, albeit at different radial positions given the fixed offset between the probes. This offset can however be removed in the post-test analysis and the values at a particular point re-aligned. These measurements may also be combined with those of the inductive coil current using the HOKA probe, providing a common time-scale to compare the development of both the electrodynamic and gasdynamic behaviour of the discharge. Such measurements have not been performed in the past and present novel information which may be used to better understand the transient behaviour of the discharge cycle.

4.4 Numerical Discharge Model for Skin Depth Analysis

A numerical tool has been developed to provide theoretical estimates for comparison with experimental skin depth measurements. However, while the techniques discussed in Section 4.3.4 are applicable to a variety of gases and gas mixtures (provided they exhibit sufficient radiation intensity and magnetic field strength), numerical simulations of the discharge require extensive knowledge of the plasma chemical reactions and transport properties. As a result, an argon discharge was simulated and compared against experimental measurements.

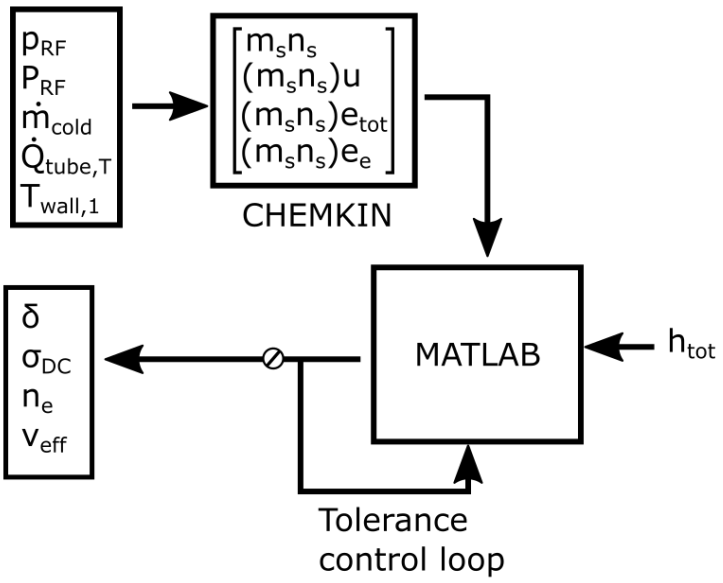

Figure 4.24: One-dimensional discharge simulation process

Figure 4.24 shows the process used to simulate thruster conditions. The discharge is modelled as a one-dimensional plasma plug flow using the CHEMKIN software [101]. The chemistry model used for these simulations was adapted from that of Gudmundson (2002) presented by Lieberman and Lichtenberg [45]. A comparison of chemistry models assessed within this work is detailed in Section 4.4.1.

The first step of the model is to use experimental input data to solve the Chapman-Enskog equations and establish a database of flow parameters with respect to temperature (T_{tra} and T_e) and enthalpy. Values of the discharge tube pressure (p_{RF}), electrical input power, mass flow rate, and tube heat flux were used as inputs. Using argon as the propellant,

the rotational and vibration equations were removed, with CHEMKIN used to solve the mass, momentum, energy, and electron energy equations. Outputs from the CHEMKIN solver are:

$$CHEMKIN_{out} = \left\{ \begin{array}{ccc} h_{tot} & M_{eff} & h_{sens} \\ T & \dot{m} & t_{plug} \\ T_e & P_{pl} & J \\ p & T_i & X_e \\ \rho & \dot{Q} & X_{Ar^*} \\ u & \dot{Q}_{surf} & X_{Ar^+} \\ c_p & T_{surf} & X_{Ar} \end{array} \right\}$$

where

h_{tot}	$\equiv$	Total specific enthalpy, [J/kg]
M_{eff}	$\equiv$	Effective flow molecular mass, [kg/mol]
P_{pl}	$\equiv$	Plasma power deposition, [W]
$\dot{Q}$	$\equiv$	Volumetric heat production rate, [W/m^3]
$\dot{Q}_{surf}$	$\equiv$	Surface heat production rate, [W/m^2]
T_{surf}	$\equiv$	Tube wall surface temperature
h_{sens}	$\equiv$	Sensible specific enthalpy, [J/kg]
t_{plug}	$\equiv$	Plug flow residence time, [s]
J	$\equiv$	Total ion current density, [A/m^2]

During these simulations, T_{surf} (not to be confused with the experimentally-obtained value, T_{wall}) used a fixed value of 500 K. This value was selected due to Argon's low thermal conductivity and low observed tube wall heat flux. Higher thermal conductivity gases (O_2 and N_2) display much greater thermal loads during operation and have previously been simulated using a wall temperature of 700 K [102]. Despite concerted efforts, additional stable solutions were not achieved due to the stiff nature of equations in the CHEMKIN software. Future numerical investigations should focus on more detailed 2D and 3D software developed at IRS [102, 103]. Within this project, numerical simulations were performed to obtain an estimate for comparison with experimental

results. The model discusses in this section is thus only used for cursory analyses and does not represent and fully-validated tool.

The database from CHEMKIN is imported into a MATLAB script which transforms the plug flow form into and inductive discharge with respect to its energy distribution resulting from the skin depth. This is done using an iterative loop, with the skin depth (true) acting as the control value.
Initial values for the skin depth and translational temperature are set at the beginning of the transformation loop.

$$\delta = \delta_0$$
$$T_{tra} = T_{tra,0}$$

Using the initial value for T_{tra}, values for the flow parameters (ρ,c_p,M) and the transport properties (μ,k) are extracted from the CHEMKIN database and calculated using the NASA polynomial relations [104], respectively.

$$\rho = \rho(T_{tra})$$
$$c_p = c_p(T_{tra})$$
$$M = M(T_{tra})$$
$$\mu = \mu(T_{tra})$$
$$k = k(T_{tra})$$

Using these values, the dimensionless flow parameters (Re, Pr, Nu) are be calculated. When considering the Nusselt number, the distinction between laminar and turbulent flows is made as follows [105]:

If Re < 3000

$$Nu_{lam} = 1.86\,(RePr)^{\frac{1}{3}} \left(\frac{d}{L}\right)^{\frac{1}{3}} \left(\frac{\mu}{\mu_{wall}}\right)^{\frac{7}{50}} \tag{4.33}$$

where μ_{wall} is the flow viscosity calculate using the wall temperature (assumed in this simulation as 500 K).

Re > 3000

$$\zeta = (0.79ln(Re) - 1.64)^{-2} \tag{4.34}$$

$$Nu_{turb} = \frac{\left(\frac{\zeta}{8}\right)(Re - 1000)Pr}{1 + 12.7\left(\frac{\zeta}{8}\right)^{2}(Pr^{\frac{2}{3}} - 1)} \tag{4.35}$$

As the plasma temperature is significantly higher than that of the wall, the influence of the wall is not significant on the flow. Hence the equation for the turbulent Nusselt number in this analysis differs from that used in the tube cooling water flow analysis (Section 4.2.3).

Using these values, the thermal boundary layer, δ_{T}, and outer plasma diameter, B, may be determined as

$$\delta_T = \frac{1}{c}\frac{l}{Nu} \tag{4.36}$$

$$B = 2(R - \delta_T) \tag{4.37}$$

where c is a correction factor (in this case 1.3) for computational stability, l is the discharge tube length, R is the tube inner radius, and t is the tube wall thickness.
From these values, the specific enthalpy contained within the skin depth zone (h_δ) may be calculated from measured specific enthalpy, h, obtained from experiments. This measured enthalpy combines thermal power measured in the jet ($\mathrm{P_{pl}}$) and tube ($\dot{Q}_{tube,T}$) as

$$h_{tot} = \frac{P_{pl} + \dot{Q}_{tube,T}}{\dot{m}_{pl}} \tag{4.38}$$

The skin depth enthalpy is hence [50]:

$$h_\delta = h\left(\left(\frac{2R}{B}\right)^2\left(4\frac{\delta}{B}\left(1-\frac{\delta}{B}\right)^{-1}\right)\right) \tag{4.39}$$

Using this new specific enthalpy value, values of $\mathrm{T_{tra}}$ and $\mathrm{T_e}$ within the skin depth zone may be interpolated from the CHEMKIN database and used to determine the species molar fractions within the flow. The plasma composition then allows the electron-neutral and electron-ion momentum transfer cross sections (from the Devoto reference model [106]) and momentum transfer frequencies to be determined, ultimately yielding a value for the DC electrical conductivity of the discharge.

$$\left.\begin{array}{r} \mathrm{T_{tra}} \rightarrow \psi_\mathrm{s}(\mathrm{T_{tra}}) \rightarrow \mathrm{n_s}(\mathrm{T_{tra}}) \\ \\ \mathrm{T_e} \rightarrow \mathrm{Q_{e\text{-}n}}(\mathrm{T_e}) \\ \mathrm{Q_{e\text{-}i}}(\mathrm{T_e}) \end{array}\right\} \left.\begin{array}{l} \\ \upsilon_{\mathrm{m,e\text{-}n}} \\ \upsilon_{\mathrm{m,e\text{-}i}} \end{array}\right\} \upsilon_m \rightarrow \sigma_{DC}$$

This value of electrical conductivity may thus be used to recalculate the discharge skin depth and compare with the value at the beginning of the cycle.

$$\delta_1 = \sqrt{\frac{2}{\mu_0 f_{RF} \sigma_{DC}}} \tag{4.40}$$

If the difference between δ_0 and δ_1 is greater than the set tolerance, the cycle is repeated, using the new values of skin depth and translational temperature as inputs.

4.4.1 Argon Chemistry

Table 4.5 lists the chemical reactions considered within the discharge model. Due to argon's extensive use in plasma simulations, a number of chemistry models exist for this simplified species list, with those investigated within this study listed in Table 4.6 and compared graphically in Figures 4.25-4.27.

Table 4.5: Argon chemistry considered

	Reaction
1	$e^- + Ar \rightleftharpoons Ar^* + e^-$
2	$e^- + Ar \rightleftharpoons Ar^+ + 2e^-$

These models differ in their mathematical formulations and the experimental setups from which they were extracted. Lieberman/Gudmundsson, Baeva et. al, and Stewart utilise the common modified Arrhenius format [45,107,108], while that of Min/BOLSIG+ [109] uses a polynomial relation to relate reaction rates to the electron temperature [109]. Furthermore, the original Gudmundsson et. al experiment [110] and that of Baeva et. al assessed microwave-generated plasmas, while Stewart [108] and Min [109] assessed a Townsend discharge and planar capacitive discharge, respectively. None of the models were hence explicitly validated against inductive systems which typically exhibit high electron temperatures due to their interaction with the coil [45]. As a result, each of them were assessed on their relative reaction rates.

Table 4.6: Reaction rate models considered

	Reaction applicability		
Model	1	2	Source
Lieberman/Gudmundsson	✓	✓	[45]
Baeva et. al	✓	✓	[107]
Stewart	-	✓	[108]
Min/BOLSIG+ (Maxwellian EEDF)	✓	✓	[109,111,112]
Min/BOLSIG+ (non-Maxwellian EEDF)	✓	✓	[109,111,112]

Following a comparison of the reaction rates, the Gudmundsson/Lieberman model was selected to describe the system. This model was selected due to its coverage of a wide range of electron temperatures (compares to the Min/BOLSIG+ model which covers only a narrow range) and it's high ion production rate at high temperatures. The difference in ion production rates for the models can been seen in Figures 4.26 and 4.27, with Gudmundsson/Lieberman and Min/BOLSIG+ producing ions at a rate $\approx$ 1000 times grater than the other models. Reaction rate constants implemented in the CHEMKIN chemistry model are listed in Table 4.7.

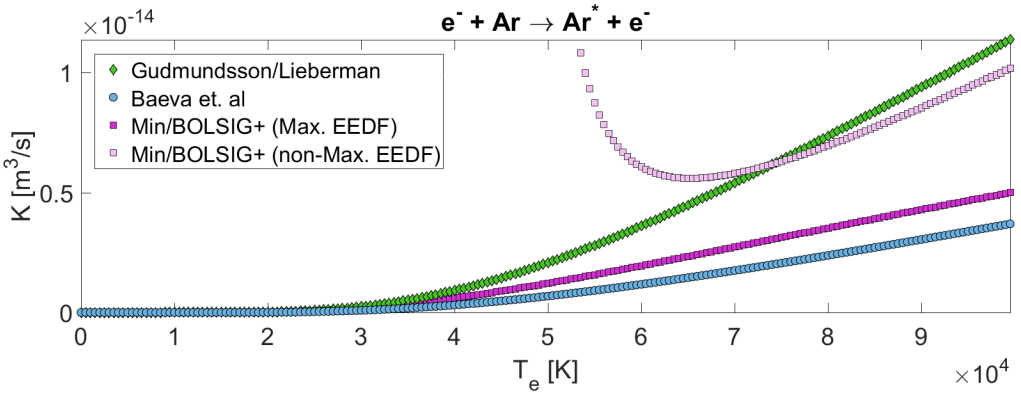

Figure 4.25: Rate coefficient for the electronic excitation of argon

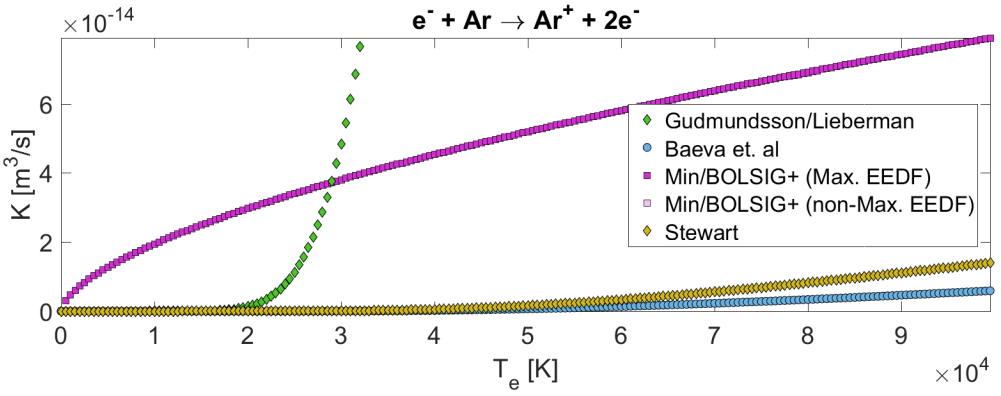

Figure 4.26: Rate coefficient for the electron ionisation of argon - scale 10^{-14} [m^3/s]

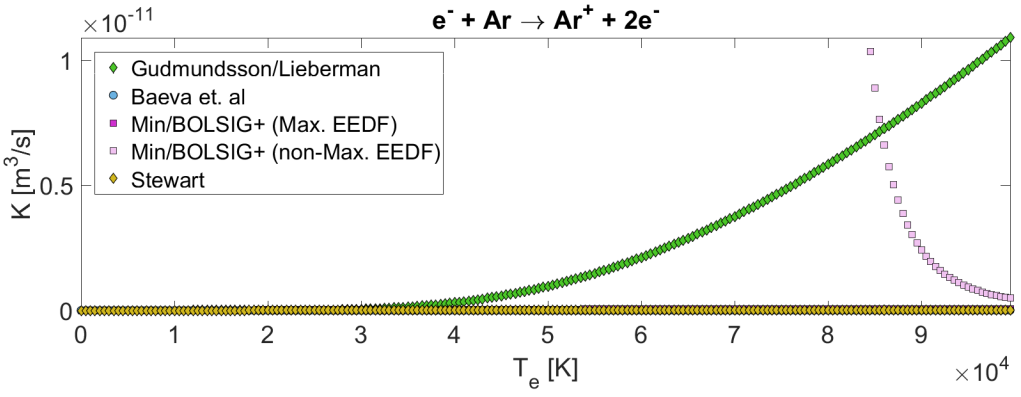

Figure 4.27: Rate coefficient for the electron ionisation of argon - scale 10^{-11} [m^3/s]

Table 4.7: Argon chemistry constants used in modified Arrhenius form, $k = AT^n e^{-E_a/(RT)}$

	Reaction	A [m^3/sK^n]	n	E_a/R [K]
1	$e^- + Ar \rightleftharpoons Ar^* + e^-$	1.303×10^{-15}	0.330	1.483×10^{4}
2	$e^- + Ar \rightleftharpoons Ar^+ + 2e^-$	9.358×10^{-14}	0.590	2.023×10^{5}

Chapter 5

Results and Discussion

This chapter reports on the results of this research. Each of the studies presented contribute to the overarching aim of assessing the performance of alternative propellants in an electrodeless propulsion system. This was achieved by obtaining experimental measurements of the thrust, specific impulse, and other relevant thruster metrics; developing novel techniques to characterise discharge regimes and assess their transient behaviour; comparing experimentally and numerically-obtained values of the inductive skin depth; assessing the impact of discharge tube wall thickness on chemically dissimilar propellants; and obtaining spatially-resolved information on the discharge tube wall temperature during operation. The combination of these studies produces a comprehensive assessment of electrodeless propulsion in the context of alternative propellant operation, including a comparison of performance with conventional EP systems.

5.1 Thrust and Thruster Performance

Thrust, specific impulse, and thrust-to-power ratio (F/P_{RF}) are three of the most critical thruster performance metrics used to determine the achievable trajectories for a propulsion system. Figures 5.1 - 5.3 show values for these metrics obtained experimentally using IPG7 for pure argon, oxygen, CO_2, and nitrogen plasmas, as well

as plasmas resulting from combinations of argon and the molecular species. Information on the volumetric flow rate, mass flow rate, and particle flux of each of the propellant configurations tested is given in Appendix A, with the volumetric proportions of the mixed propellants listed in Table 5.1. In order to support investigations of both thruster performance (thrust, I_{sp}) and the discharge itself (coil current profile), propellant flow rates were selected such that chemically dissimilar mixtures could be compared on mass flow and particle flux bases. However, a number of practical limitations resulted in equivalencies of 97.8 % to 81.2% between comparable mixtures. These included choked CO_2 flow resulting from propellant line freezing (past the operating envelope of the CO_2 gas warmer) and variations in propellant availability resulting from disturbances in the laboratory gas supply system. Further limitations were encountered once the propellant was ignited, with certain mixtures producing either unstable discharges or excessive thermal loads at low powers (50 kW). Despite these limitations, the conditions tested allow good comparisons on the basis of mass flow, particle flux, and volumetric ratios. Appendix A contains relevant chemical properties and reaction data for the species considered within this work. All measurements in this section were conducted using a 2.2 mm discharge tube wall thickness.

Table 5.1: Mixed propellant chemistry (by volume)

Propellant name	Propellant volumetric composition	$\dot{m}_{\text{eff}}$ [g/s]
Ar:O_2-5	0.59 Ar + 0.41 O_2	3.49
Ar:O_2-6	0.68 Ar + 0.32 O_2	3.69
Ar:N_2-9	0.58 Ar + 0.42 N_2	3.36
Ar:N_2-10	0.68 Ar + 0.32 N_2	3.58
Ar:N_2-11	0.74 Ar + 0.26 N_2	3.72
Ar:CO_2-14	0.74 Ar + 0.26 CO_2	3.28
Ar:CO_2-15	0.79 Ar + 0.21 CO_2	3.41

As shown in Figures 5.1 - 5.3, propellant configurations combining argon and the other gases produced significant increases in measured thrust, I_{sp}, and F/P_{RF} over their pure gas counterparts, with the exception of oxygen which displayed a slight reduction of I_{sp}. The reason for this general increase in thrust-specific performance, as well as

the difference between final values obtained by the single propellants, is a result of the propellant chemical properties and the discharge regime of the resultant plasma.

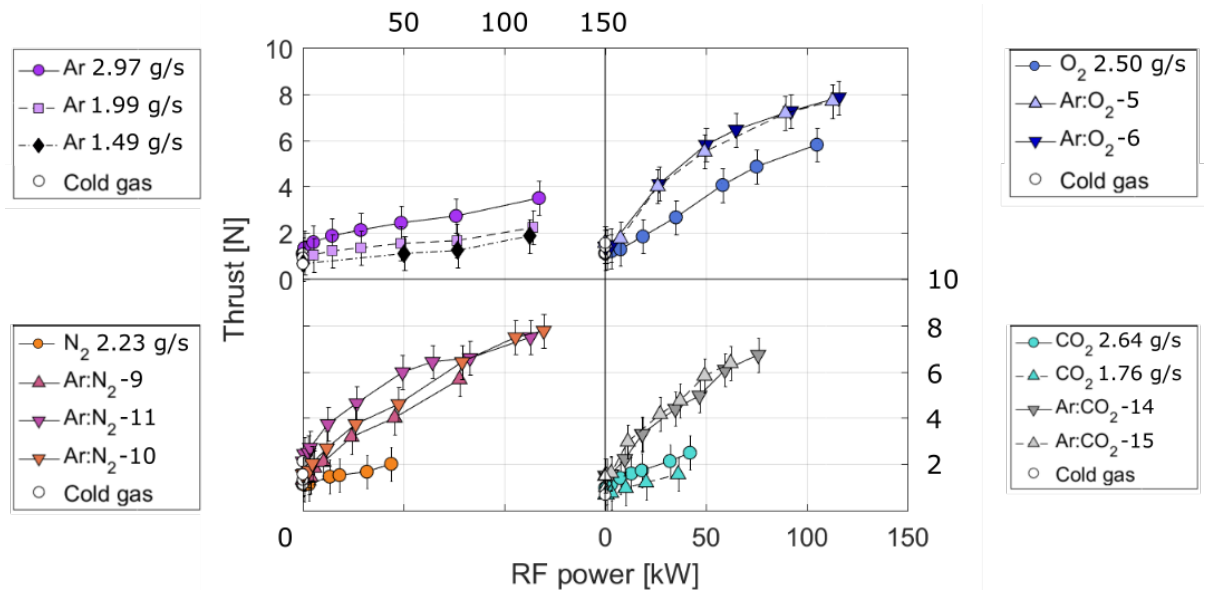

Figure 5.1: Measured alternative propellant thrust at respective mass flow rates (Table 5.1) and thruster input (RF) power

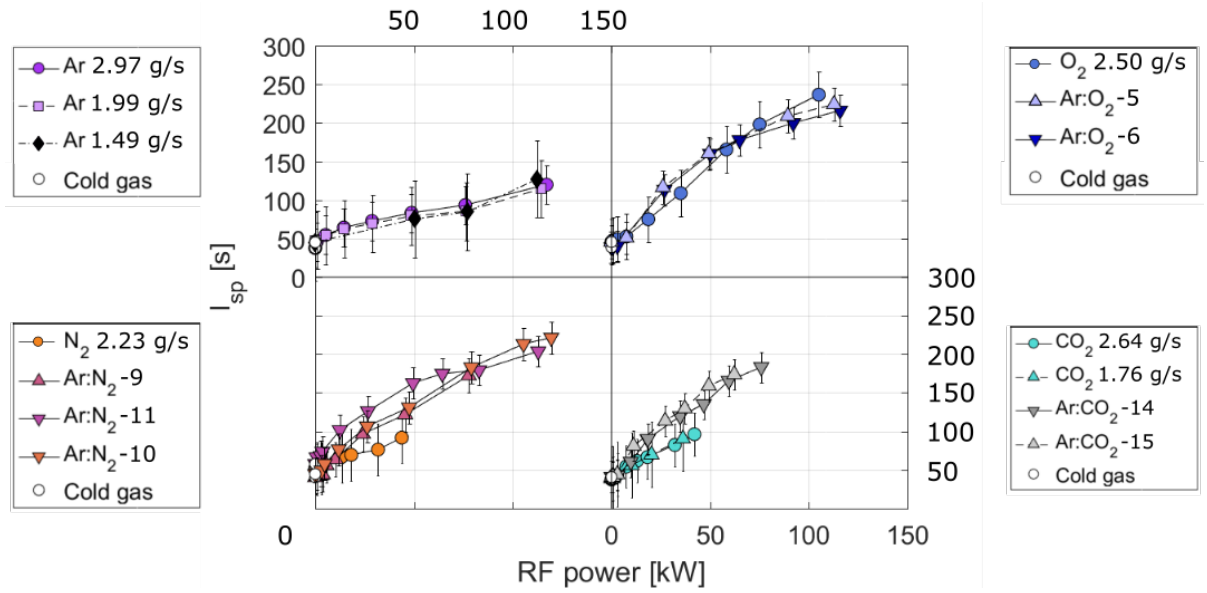

Figure 5.2: Alternative propellant specific impulse (conditions as in Figure 5.1)

In interpreting these values, the relation between thrust, I_{sp}, and mass flow rate, as given in Equation 4.28, should be considered. At low input powers, heating in the discharge chamber is low due to the low coupling efficiency of the capacitive mode. As a result, propellants exhibit similar values of I_{sp} ($\approx$ 50 s) and the influence of mass flow rate on thrust is more significant. This explains the higher thrust produced by Ar, in

comparison to the molecular species, at low input powers. However, at higher input powers, the influence of I_{sp} dominates that of the mass flow rate.

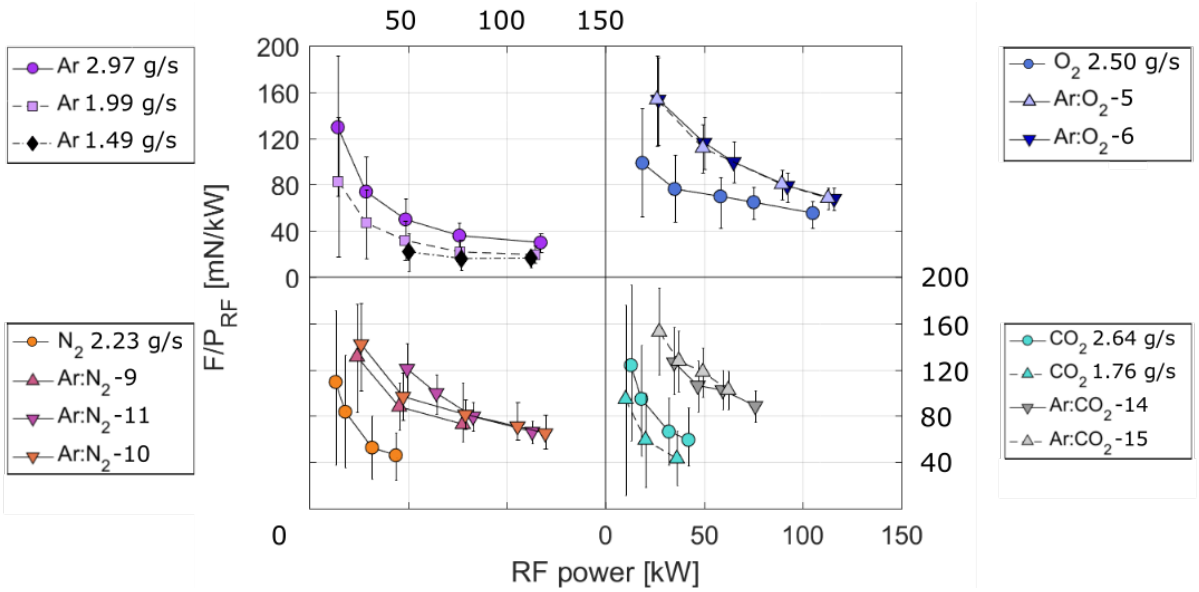

Figure 5.3: Alternative propellant thrust-to-power ratio (conditions as in Figure 5.1)

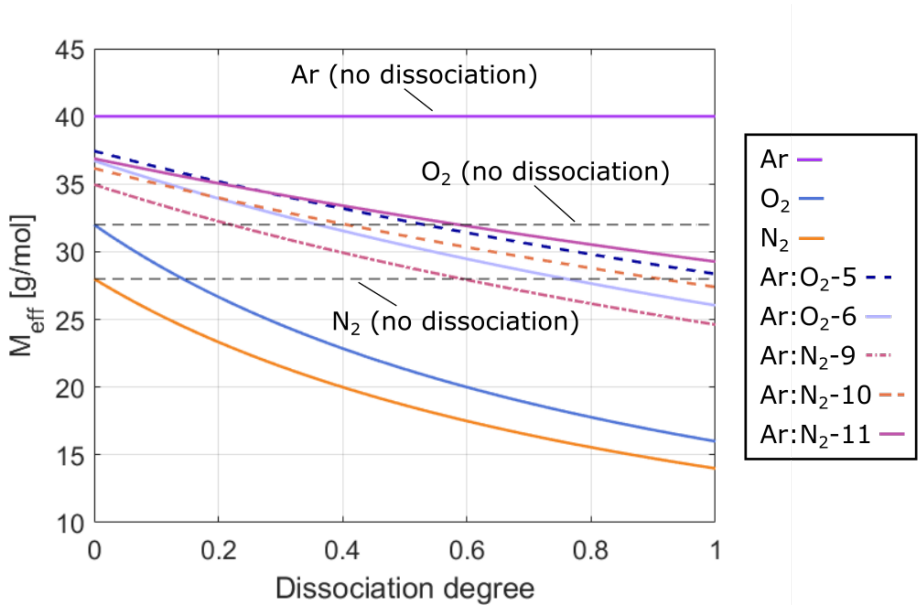

Figure 5.4: Impact of of propellant dissociation on mean molecular mass

The final velocity of particles exiting the thruster is dependent on the species molecular mass. With the exception of CO_2, Ar exhibits the highest molecular mass, with the other propellants able to obtain greater exit velocities in their molecular states. The impact of molecular mass on velocity is further highlighted when considering dissociation of the propellants. Any dissociation of O_2, N_2, or CO_2 greatly increases the maximum obtainable

value of I_{sp} in comparison to Ar. In the combined cases, dissociation acts to significantly lower the mean species molecular mass, as shown in Figure 5.4.

However, as is seen in Figures 5.1 - 5.3, the molecular propellants produced higher thrust when combined with Ar, despite the increase in mean molecular mass. The increase of thrust is also greater than that which can be attributed to the propellant mass flow rate. Thrust values recorded for N_2 and CO_2 were each a factor of 2 higher for 50 % and 20 % increases in the total mass flow rate, respectively. This improved performance is a result of an increased translational temperature in discharge volume. Increasing translational temperature acts to increase the pressure in the discharge chamber and causes propellant to exit the thruster at higher velocities. As the IPG7 is an electrothermal thruster, without additional acceleration mechanisms, the pressure difference between the discharge volume and vacuum tank is the sole source of propellant acceleration [1]. Translational temperature in the IPG7 jet is dependent on two primary factors; the quantity of energy transferred from the inductive coil and its distribution among heavy particles in the plasma.

Within electrodeless thrusters, energy is transferred from the coil to the electrons, which in turn transfer energy to heavy particles as a result of collisional (Ohmic) heating. The magnitude of energy conveyed to the propellant is dependent on the electron number density within the discharge volume, requiring consideration of the ionisation energy of the propellant species. Of the propellants tested, Ar yields the highest theoretical electron number density per unit of input power [113]. This is due to its atomic structure, with incoming energy converted to either excitation or ionisation processes. By comparison, molecular propellants tested exhibit greater ionisation energies as well as additional losses such as dissociation and the rotational and vibrational energy modes. However, despite its affinity for ion and electron production, final I_{sp} values recorded for Ar were almost a factor of 2 lower than propellant mixtures of significantly higher net ionisation energy. This is due to the second factor influencing translational temperature in the discharge volume; the thermal conductivity of the plasma.

[1] Due to the high discharge pressures and low magnetic field strength of the inductive coil, acceleration from electromagnetic forces can be neglected from analyses of thrust production.

As thrust is produced by heavy particle species (neutral and ionised) in the IPG7, the transfer of energy between atoms and molecules within the discharge volume is of high importance. Observing the thermal conductivities of the propellants investigated (Table A.1), the low value of Ar for both thermal conductivity and specific heat capacity explain why pure Ar propellants were ineffective at converting power from the inductive coil to useful thrust. This conversion was more effective for the molecular species, each of which exhibit higher specific heat capacity and gas thermal conductivity (with the exception of CO_2 for which thermal conductivity is lower than Ar at room temperature). The combination of these factors, being the molecular mass of the propellant, the transfer of energy from the inductive coil to electrons, and the distribution of thermal energy in the discharge, can be used to explain the results shown in Figures 5.1 - 5.3.

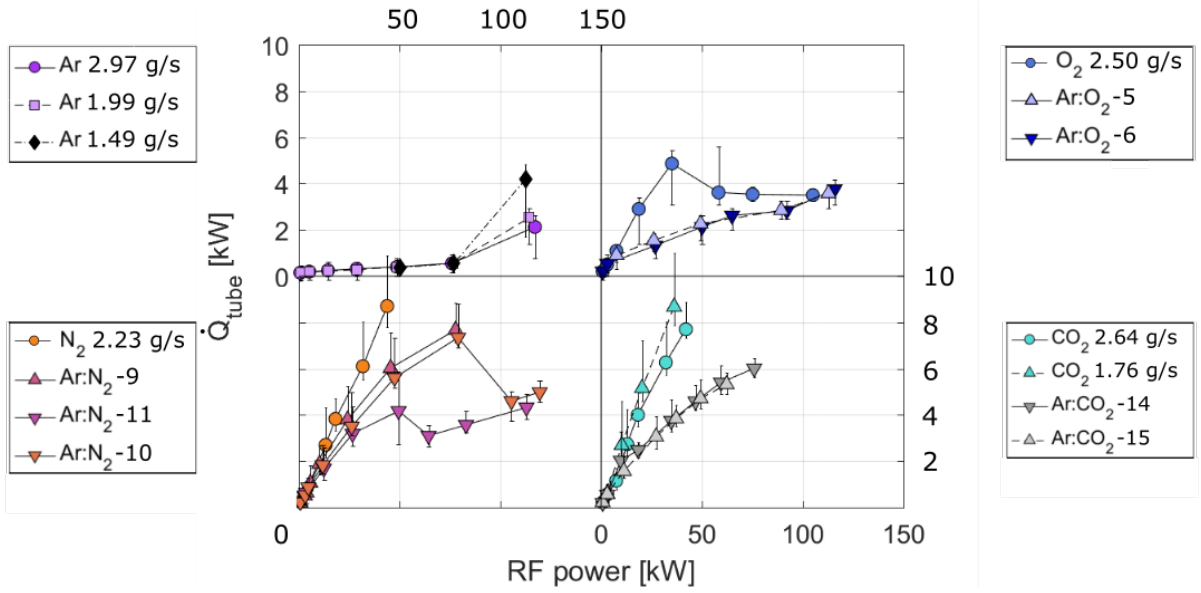

Figure 5.5: Discharge tube heat flux for the alternative propellants (conditions as in Figure 5.1)

O_2 displayed the highest final thrust, I_{sp}, and F/P_{RF} from the molecular propellants as a result of its relatively low dissociation and ionisation energies, as well as its high thermal conductivity and specific heat capacity. Both N_2 and CO_2 displayed poor performance due to their respective chemical properties. The high ionisation energy, dissociation energy, and specific heat capacity of these two propellants resulted in a high temperature plasma which was unable to transition to the subsequent discharge regime due to an insufficient degree of ionisation. As a result, N_2 and CO_2 exerted significant thermal stress (> 9 kW) on the discharge tube at relatively low input powers (< 50 kW). This prevented additional power to be applied to the propellant without the risk of critical damage to the thruster

as discussed in Section 4.2.3. The discharge tube heat fluxes recorded during experiments are shown in Figure 5.5.

The increased thrust, I_{sp}, and F/P_{RF} of the propellant mixtures is a result of preferential combination of propellant chemical properties. By combining argon with the molecular species, a high discharge electron number density (produced using argon) was combined with the high thermal conductivity and low molecular mass of the other gases. This facilitated an effective transfer of energy from the coil to heavy particles in the discharge volume and hence a high thruster performance. Furthermore, the combined thermal conductivity of these propellant mixtures acted to reduce thermal loads on the discharge chamber, allowing N_2 and CO_2 to be used with higher input powers.

Decreases in discharge tube heat flux for increasing input power, as shown in Figure 5.5 for the O_2 and Ar:N_2 conditions, highlight another critical factor when considering the performance of propellants within the thruster. This behaviour is representative of the high inductive discharge regime, with the plasma collapsing to the tube centre axis (producing a higher plasma density) and hence increasing the thermal boundary layer within the tube. As discussed in Section 4.2.1, the thruster displays a number of discharge regimes, each with their own electromagnetic field orientation and plasma-coil coupling efficiency. Coupling efficiency is lowest for the capacitive regime, increases through the low inductive regime, and reaches a maximum in the high inductive regime [50]. Examples of the discharge cross-sections of these three regimes are shown in Figure 5.6.

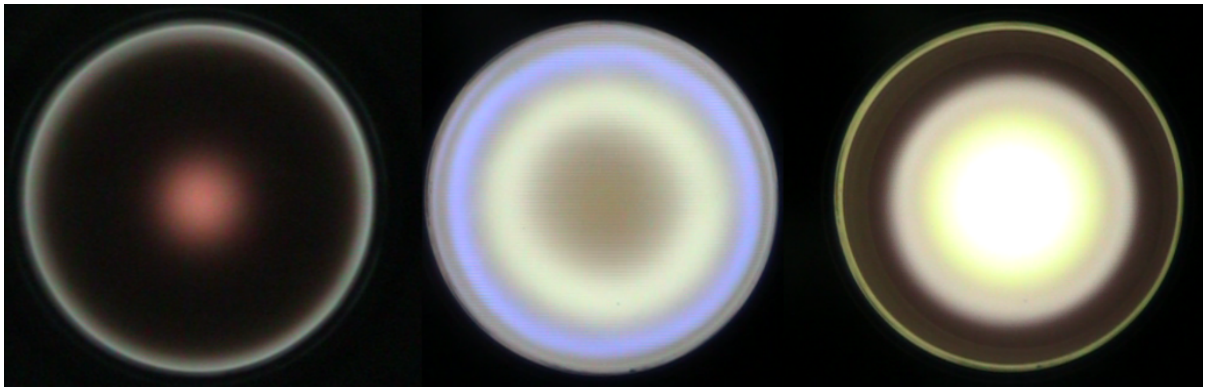

Figure 5.6: Capacitive (left), low inductive (centre), and high inductive (right) discharge cross-sections for O_2

Increased coupling efficiency leads to a greater proportion of electrical input energy being transferred to the propellant. As can be seen from the results presented in this section, this has a significant effect on final values of thrust and I_{sp} produced by the thruster. The ability to accurately identify and characterise these discharge regimes, as well as the transitions between them, is hence required to better understand and optimise the performance of the various propellants. A novel technique to achieve this goal will be presented in Section 5.2.

5.2 Discharge Regime Classification

The following section reports on the previous and improved methods of assessing discharge regimes in the thruster. In this section, the analysis is performed on three propellant conditions to provide a succinct overview of the technique. The same analyses may be performed for other gas mixtures. This analysis has been published in Plasma Sources Science and Technology [114].
The propellants assessed in this study are pure O_2, Ar:O_2-5 (0.59 Ar + 0.41 O_2), and Ar:O_2-6 (0.68 Ar + 0.32 O_2). These propellants were chosen to provide variation in the gas transport properties and chemistry. Additional information on the propellant conditions is given in Appendix A.

Figure 5.7 shows measurements of thermal power from both the jet and the discharge chamber for the three propellant configurations assessed. The results in Figure 5.7 represent a common method used previously to identify regime transitions, citing a significant increase and decrease for transitions to the low inductive and high inductive regimes, respectively. However, as can be seen, the visibility of these trends is not equal between the three gas configurations. Input power conditions at which discharge regimes transitions were observed for the three propellants are listed in Table 5.2, identified using a combination of the HOKA probe and data obtained from the generator power supply. The two stable discharge regimes either side of a transition may be separated by several hundred volts, with the region between these points switching in an unstable manner between the two. Transitions are hence defined using the first position at which a stable discharge in the regime is achieved, with lines in

Figure 5.7 indicating the beginning of the unstable transition zone.

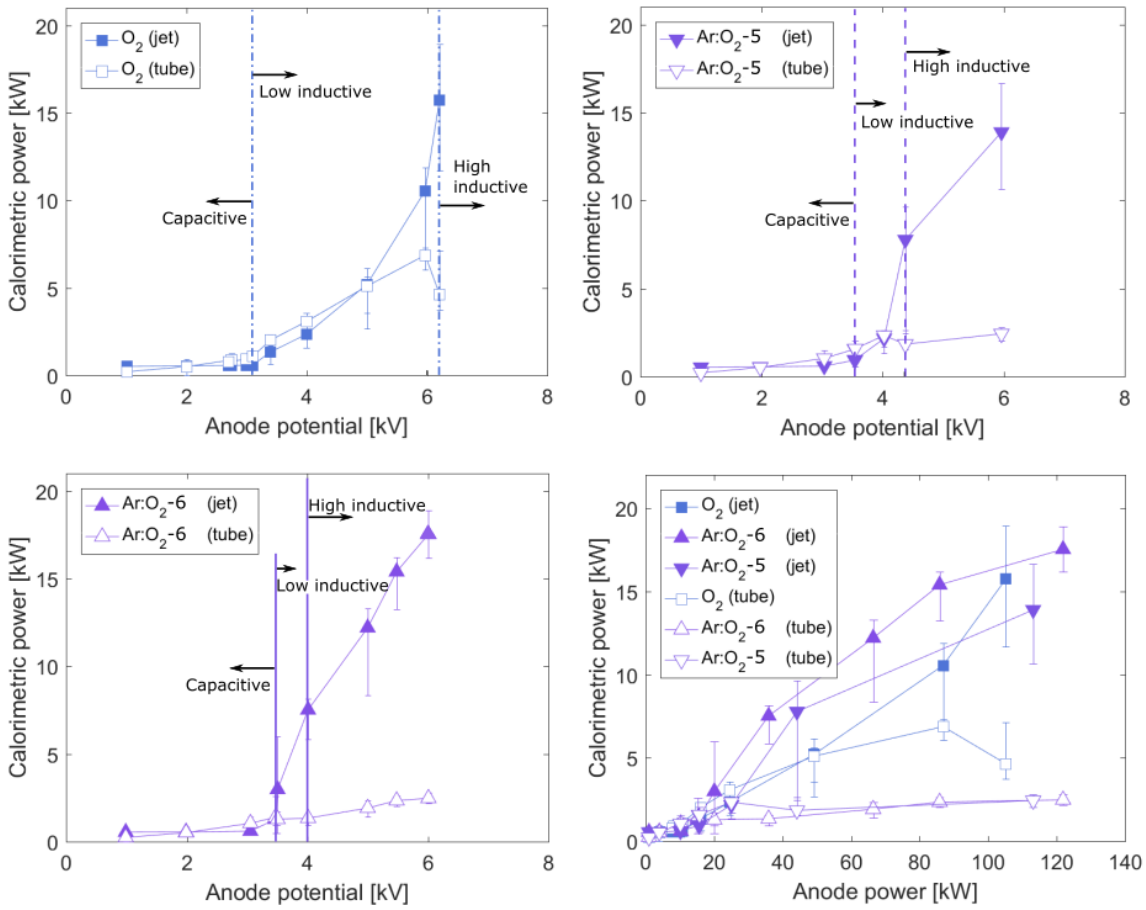

Figure 5.7: Measured calorimetric thermal power (jet and tube) for pure O_2 and Ar:O_2 mixtures

Table 5.2: Conditions at transitions between discharge regimes

	Capacitive → inductive		Low inductive → high inductive	
	U_A [kV]	P_A [kW]	U_A [kV]	P_A [kW]
O_2	3.1	11	6.2	105
Ar:O_2-5	3.6	16	4.4	44
Ar:O_2-6	3.4	15	4.0	36

Transitions from the low to high inductive mode are clearly identifiable in pure O_2 flows, with the tube thermal power decreasing as the plasma condenses to the centre of the flow [50]. The magnitude of this reduction decreases with increasing proportions of Ar. This is due to argon's low thermal conductivity, retarding heat transfer to the discharge

tube walls and producing a lower overall tube thermal power. The reduction in thermal power recorded in the discharge tube owing to the low to high inductive transition was 32.5 %, 22.9 %, and 8.1 % for O_2, Ar:O_2-5, and Ar:O_2-6, respectively. The decrease in visibility for tube thermal power in the mixed flows is somewhat compensated by that of the jet power, which shows a distinct increase once the higher inductive mode has been reached. Recording this increase does however require constant measurements of the generator plume thermal power, restricting the use of other measurement probes in the tank.

The transition from the capacitive to low inductive regime is somewhat unclear amongst all three configurations. This transition is associated with an increase in thermal power, again observed primarily in the jet flow rather than the discharge tube. Increases of 1.51 %, 55.44 %, and 112.13 % were recorded for the O_2, Ar:O_2-5, and Ar:O_2-6 propellants, respectively. In contrast to the second transition, the visibility of the first transition is higher with increasing proportions of Ar. An investigative technique based on thermal conductivity hence has sever limitations in its applicability to chemcially dissimilar gasses. Previous campaigns have also utilised parameters such as the tube pressure and jet dynamic pressure (radial) profile to define transitions [50, 65]. However, these techniques also rely on gasdynamic effects, requiring a high propellant thermal conductivity.

A more reliable method of addressing transitions in the plasma is to assess behaviour of the electrons, performed here through measurements of the inductive coil current. Figure 5.8 displays measured values of the coil current for the capacitive, low inductive, and high inductive regimes, as well as the RF frequencies observed over the given capture period. As can be seen, each of the discharge regimes display distinct behaviour with respect to the contours of the current profiles as well as the characteristic frequencies exhibited.

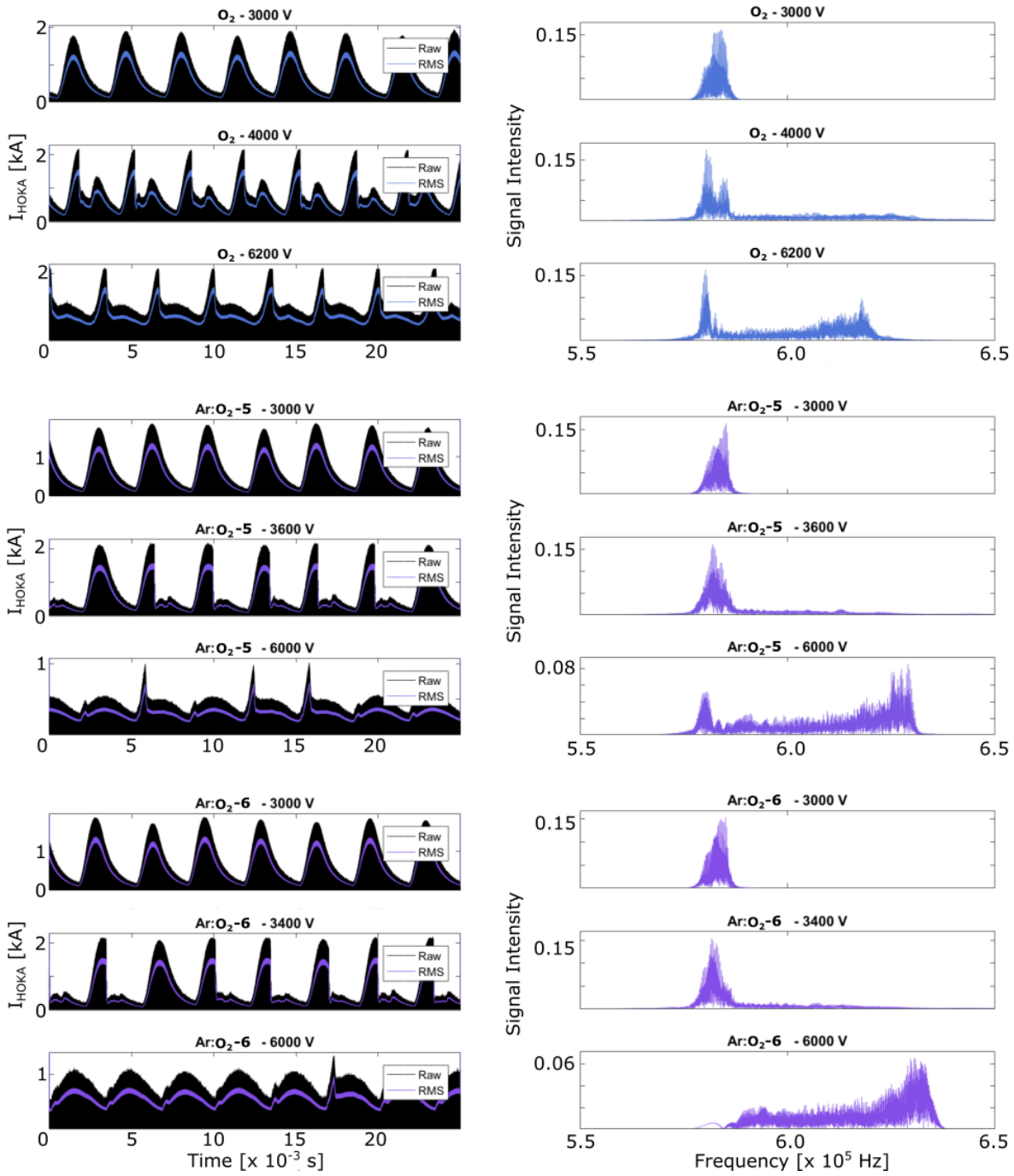

Figure 5.8: Progression through capacitive (top), low inductive (middle) and high inductive (bottom) discharge regimes for coil current (left) and characteristic coil frequency (right) for the three propellants

Discharges in the capacitive regime exhibit a current flow as discussed in Section 4.3.3, being dominated by the RF power supply and showing little interaction with charged species in the flow. This behaviour continues up until the instigation of the low inductive regime, where the azimuthal current generates a significant electron population to cause a deviation from this capacitive profile. The magnitude of this deviation varies depending on

the propellant mass flow rate and volumetric composition, though it is clearly identifiable for the gases tested within this project. Furthermore, a broader set of characteristic frequencies become visible once the low inductive mode is reached. Combining these two traits, the first discharge transition can be clearly identified regardless of the gas utilised. A similar variation in the current profile and characteristic frequencies is also observed for the transition between low and high inductive operation. Variations in the coil current and frequency are equally identifiable between the three propellants, showing a lack of sensitivity to the propellant transport properties. The use of coil current to distinguish between discharge regimes hence represents a significant improvement over the thermal method shown in Figure 5.7 which displays a high dependence on propellant transport properties.

The characteristic capacitive frequency (f_{cap}) of the system exhibited a reasonably stable mean value of 586 kHz ($\pm$ 0.3 %) for each of the three propellants tested. Variations of $\approx$ 1 % are attributed to small instabilities and fluctuations within the power supply as well as weak interactions with the working gas. This frequency remains present throughout both inductive regimes, though the instigation of additional characteristic frequencies are of a different order and origin than instabilities in the power supply. The deviation of coil current profiles in the two inductive modes from that of the capacitive is attributed to variations in the degree of ionisation in the discharge and subsequent electron number density. Once the azimuthal electric field within the plasma has been established, electrons within the plasma are able to engage in Coulombic interaction with electrons on the inductive coil surface (as discussed in Section 4.2.1), which themselves exhibit azimuthal motion due to the geometry of the coil. As the coil-plasma coupled system may be described as an equivalent transformer, the shifts in coil frequency may thus be attributed to the impedance matching of the RF resonant circuit to the resultant plasma discharge. An increased degree of ionisation within the discharge volume produces an impedance imbalance from the purely capacitive configuration. Hence compensation is sought through a modulation of the coil current itself. Such behaviour is corroborated by the increasing magnitude of final characteristic frequencies observed with increasing power and increasing proportions of Ar. The tendency of Ar to produce ions with lower input power than O_2 (due to dissociation losses and differences in required ionisation energy) would support a greater degree of ionisation for increasing quantities of Ar within the flow.

In addition to identifying discharge regimes, the data presented in Figure 5.8 can be used to assess the transient behaviour of discharges within a single discharge cycle. This is achieved by discretising the set and assessing the frequency exhibited at distinct intervals. An example of such a discretisation is shown in Figure 5.9 for the O_2 case, with results being the average of 10 individual cycles. In this Figure, $I_{HOKA,RMS}$ denotes the root-mean-squared coil current measured by the HOKA probe, and f_{char} represents the characteristic frequency measured at the given interval. This figure highlights the relationship between the deviation in the coil current profile and shift in coil operating frequency, resulting from increased flow ionisation as previously discussed.

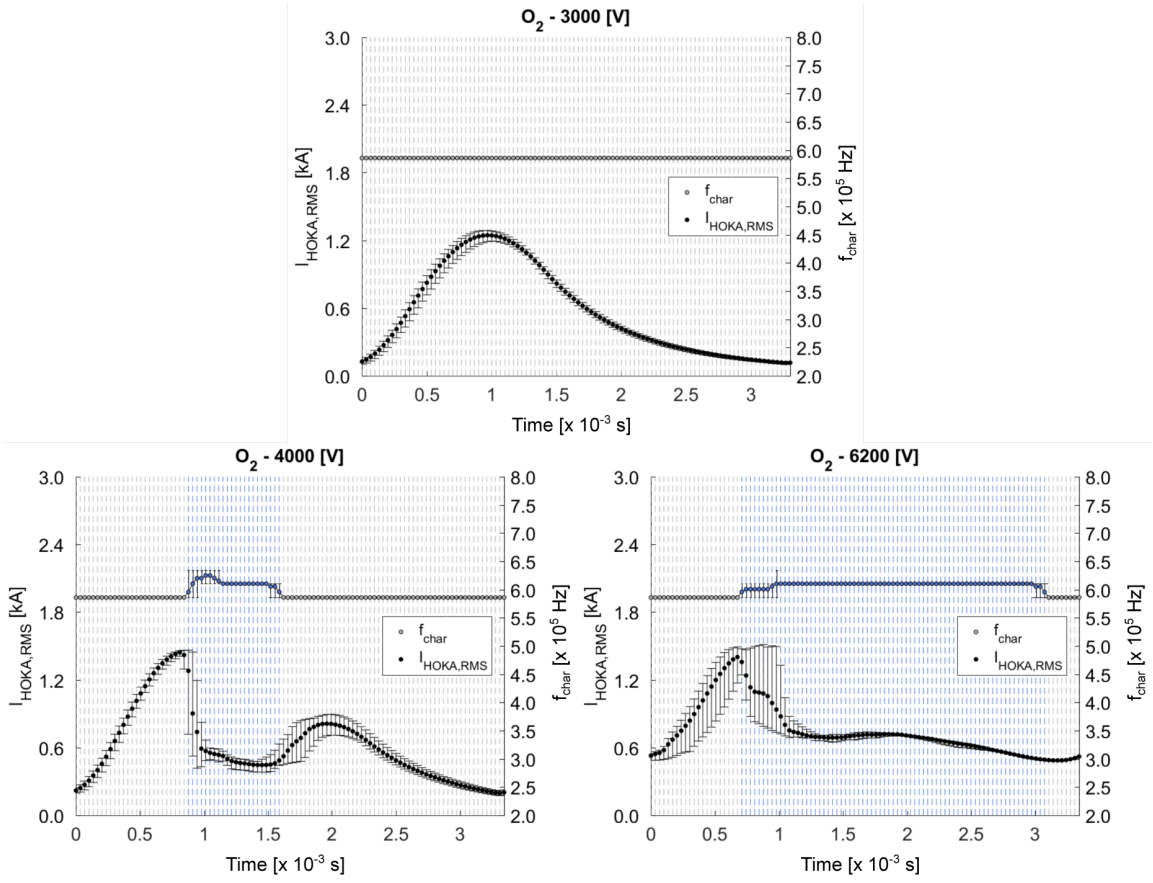

Figure 5.9: Discretised coil current profiles for the three regimes for O_2

A discretised frequency analyses for all three gas configurations is shown in Figure 5.10. By analysing points at which the dominant discharge frequency deviates from f_{cap}, the proportion of time spent in the inductive regime may be calculated. This information assists in assessments of the stability and consistency of the discharge, with significant implications for electric propulsion systems. As previously shown, the thrust and I_{sp} of the thruster depend heavily on the discharge regime. Hence the ability to assess the duration spent in the different regimes, and whether transitions to these regimes are

stable or temporary, provides information which can be used to further optimise thruster performance.

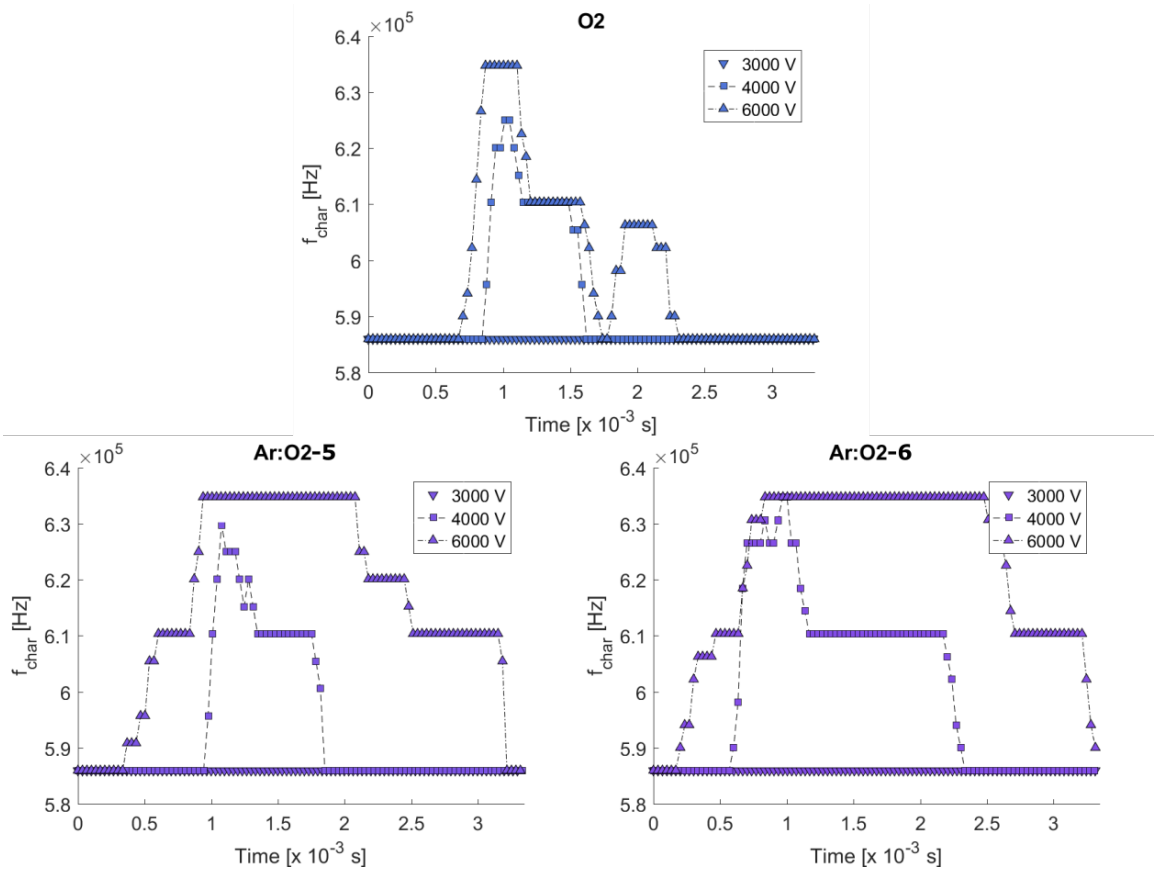

Figure 5.10: Transient frequency behaviour of the three propellants

The distributions of time spent in the capacitive and inductive regimes for the three propellants tested are given in Figure 5.11, with the influence of both increasing power and increasing proportions of Ar evident. Within this assessment, no distinction is made between high and low inductive regimes. As can be seen, a number of distinct frequencies are common between the two inductive regimes, requiring additional information to differentiate their sources. At its maximum power condition, Ar:$O2_2$-6 showed that 94 % of its discharge cycle occupied the inductive regime. By comparison, O2 and Ar:$O2_2$-5 occupied the inductive regime 71 % and 85 % of the time, respectively, at maximum power. By increasing the time spent in the inductive regime, fluctuations in discharge chemistry may be reduced, hence producing more stable test conditions. While applied in this case to a mixture of noble and diatomic gases, the same analysis may be used with any gas mixture within the IPG. This includes the alternative propellants reported on in Section 5.1.This method is also non-intrusive, presenting a significant advantage over the thermal power method and its reliance on measurement

equipment in the thruster jet.

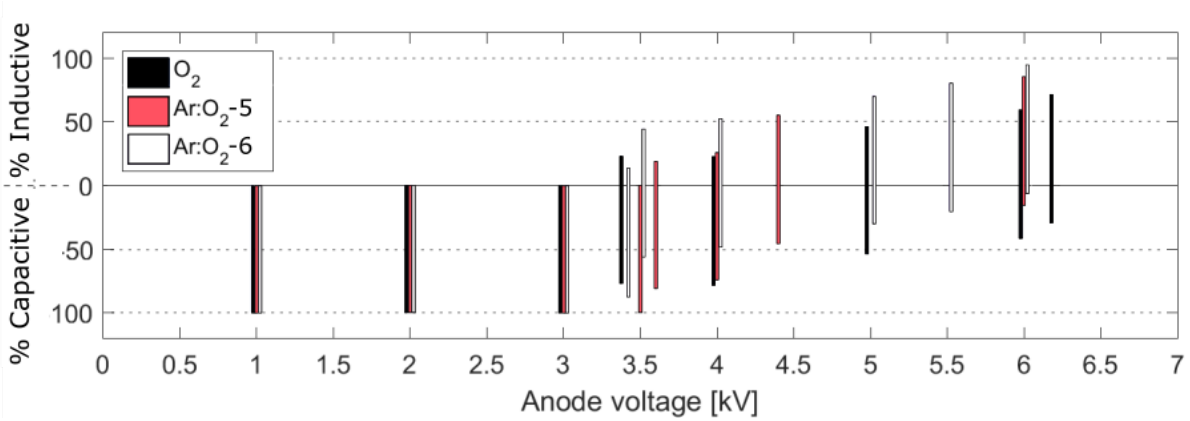

Figure 5.11: Regime dominance with increasing power

Considering the initial capacitive proportion of each cycle (being that prior to the first measurable shift in characteristic frequency), an evaluation of the energy required to instigate inductive operation may be performed by taking the integral of the measured current and multiplying it by the coil potential (assumed here to be 75 % of the anode potential [82]). This value, termed ignition energy (E_{ignit}) is given by:

$$E_{ignit} = U_{rf} \int_0^{t_H} I_{HOKA,RMS} \quad dt \tag{5.1}$$

$$U_{rf} \approx 0.75 U_A$$

where t_H is the time at which the initial deviation in frequency and capacitive current profile is observed. Results for this measurement are given in Figure 5.12.
As is to be expected, the energy required to instigate the inductive discharge decreases with increasing power. This is due to the increase in energy deposited and retained in the discharge between discharge cycles, reducing the extent of cooling and recombination. The vertical lines in this plot represent the anode potentials at which the respective gases transition between modes, with significant drops in the ignition energy observed immediately following each transition. There is however a common increasing trend for the necessary ignition energy leading up to each transition, with pure O_2 showing the greatest variation over the total power range. The influence of increasing quantities of Ar within the flow is also clear, with the necessary ignition energies for the higher inductive

flows featuring Ar significantly lower than those of O_2. The same behaviour is not observed for the transition to the low inductive regime, however, requiring consideration of the respective chemical properties of the two propellant species.

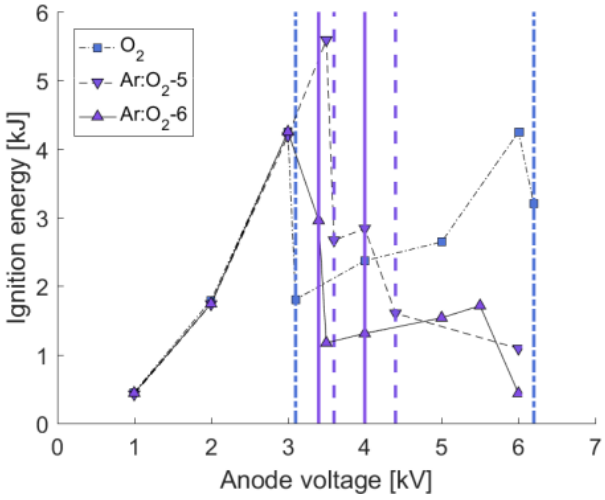

Figure 5.12: Ignition energy with increasing potential, discharge transition lines as given in Table 5.2

Argon's monatomic structure allows the conversion of incoming energy to excitation or ionisation only, producing a greater plasma ionisation degree than O_2 for the same input energy. As a result, flows with a combination of Ar and O_2 are expected to transition with lower input power than pure O_2, owing to an increased electron number density. However, power required for the capacitive to low inductive transition is seen to increase with the addition of Ar. This increase is a result of interaction between the argon and oxygen species within the discharge and is likely attributed to a change in the distribution of frozen losses between the two core species. In order to investigate this phenomena further, additional measurements such as emission spectroscopy are required. These are presently out of the scope of this project and should be performed as future work.

Other notable points from Figure 5.12 are the variations in ignition energy for each gas at its respective transition points. Results for O_2 show an almost consistent value of 4.25 kJ required to transition to both the low and high inductive modes, while the Ar:O_2 mixtures show a significant reduction in necessary energy between the two transition points (5.59 and 2.84 kJ for Ar:O_2-5 and 4.25 and 1.17 kJ for Ar:O_2-6). The reasons for this discrepancy will also require further investigation to discern.

The progression and convergence of coil current over the full power range is also of interest, particularly when considering the variation in gas configurations. This data is shown in Figure 5.13, with the influence of Ar clearly visible in causing convergence between the mean and maximum coil currents within the cycle. Such behaviour can also be seen in Figure 5.9, where discharges in the high inductive range tend towards a greater homogeneity in the temporally resolved current. The peak current in the coil is consistently observed immediately before the transition between low and high inductive modes. This behaviour is likely caused by ionisation of the discharge volume steadily decreasing following the coil current peak, to a point where the inductive mode cannot be maintained and only capacitive coupling is supported.

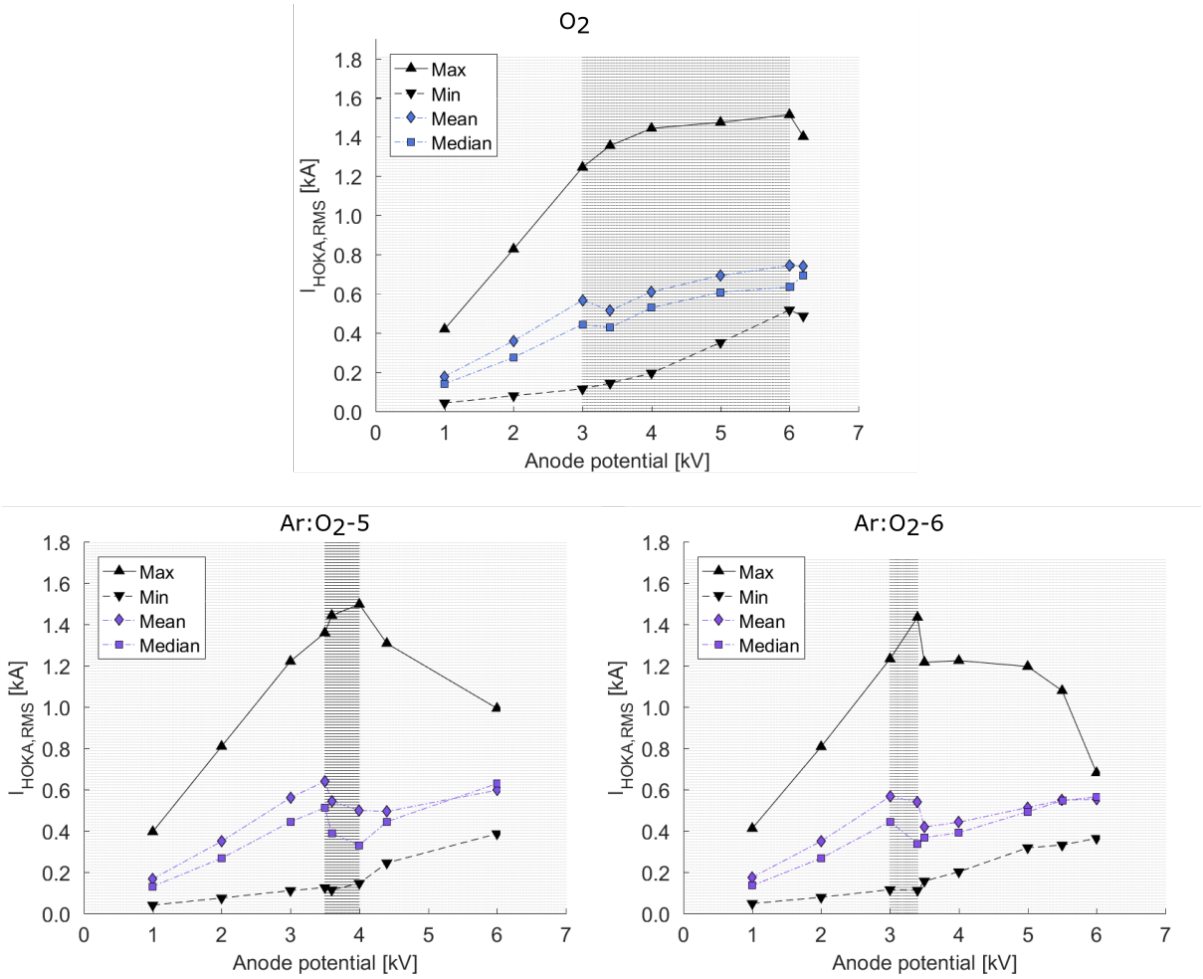

Figure 5.13: Convergence of peak and mean coil current with increasing potential for the three propellants

The end result of analyses discussed within this section is a method of non-intrusively identifying and characterising discharge regimes exhibited by the

thruster. This includes the ability to assess the transient behaviour and stability of discharges for various propellant configurations. Discharge instabilities have clear implications on the performance of the thruster, with the method presented here allowing their investigation regardless of propellant chemical properties.

The technique detailed in this section may be used to assist in the explanation of increased thrust produced by certain propellants, discussed in Section 5.1. While this method is unable to assess the conversion of electrical input energy to usable kinetic energy (to produce thrust), it does provide a means to identify the discharge regime occupied by the propellants at each input power condition. As each regime represents a particular power coupling efficiency, propellant conditions which occupy more efficient regimes at lower input powers display a steeper thrust-to-power gradient, as seen in the previous section. This information can be used to separate the thrust produced by the propellant's cold gas conditions (mass flow rate and transport properties) from that generated by preferential coupling with the thruster coil heating. As a result, the ability to observe the discharge behaviour at the same time as thruster performance enables a more comprehensive understanding of the thruster and its effective utilisation of a given propellant.

5.3 Electromagnetic Transition Behaviour

Building upon the results from Section 5.2, additional techniques were developed in order to assess the electromagnetic behaviour of the discharge (rather than the inductive coil) with a similar temporal resolution. This approach was met with measured success as well as limitations. Figure 5.14 shows videos of radial distributions of visible radiation and net magnetic field strength generated by the thruster in the low inductive and high inductive regimes. Still images of these videos are given in Appendix B. The reference propellant condition for this analysis is the Ar:N_2-10 mixture (0.68 Ar + 0.32 N_2). A number of other propellants were also investigated using this technique, with their behaviours being equitable. Ar:N_2 is hence used here as an example of how the technique may be applied.

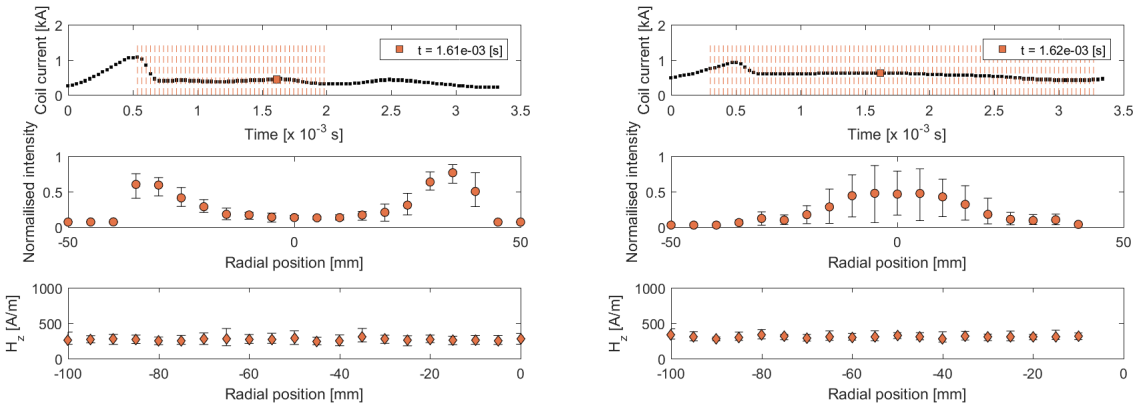

Figure 5.14: Ar:N_2-10 coil current, visible radiation, and net magnetic field strength for the low inductive (left) and high inductive (right) regimes

Pause Play

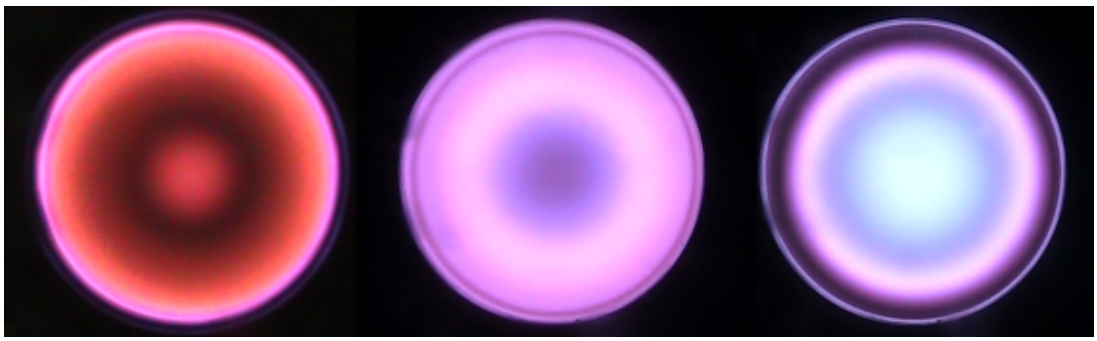

Figure 5.15: Video images of the Ar:N_2 discharge cross section for the capacitive (left), low inductive (centre), and high inductive (right) regimes

From these dynamic images, a number of immediate observations may be made. Firstly, while the radiation intensity and distribution of the plasma shown in Figure 5.14 agree well with standard video images taken of the discharge cross-section (Figure 5.15), the values vary significantly over the total discharge cycle. As in Section 5.2 the shaded area in Figure 5.14 indicates inductive operation as determined by the HOKA method. During the capacitive component of the cycle, the radiation intensity increases proportionately with the coil current, indicating a strong coupling between the electron and electronic temperatures (T_e and T_{el}, respectively) within the discharge. However, following the initial transition to inductive operation, visible radiation diminishes almost entirely before reappearing in its expected (regime-specific) distribution. This delay indicates a strong thermal nonequilibrium between T_e and T_{el} as a result of the discharge azimuthal electric field. Furthermore in the case of the low inductive

discharge, the position of maximum radiation intensity, used to determine δ_{vis}, displays significant radial variation during the cycle. While not identical to the true skin depth behaviour, this variation in δ_{vis} displays another example of significant transient variation of energy within the discharge cycle. Values for δ_{vis} are shown in Figure 5.16.

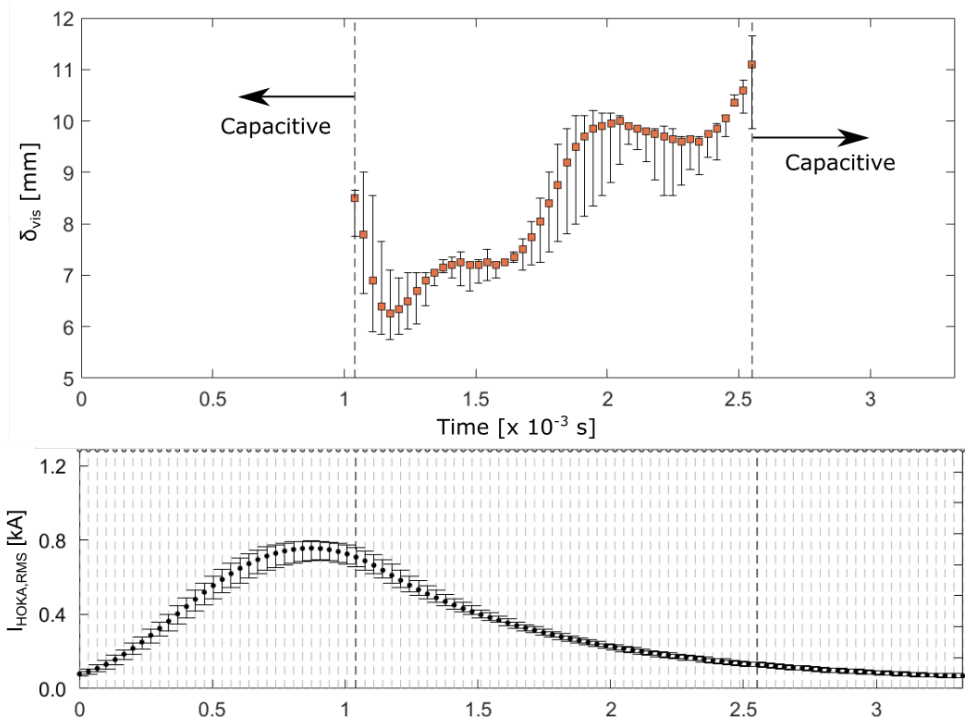

Figure 5.16: Variation of visible skin depth during operation for Ar:N_2-10, low inductive discharge (above) and capacitive discharge profile (below)

Excluding the erroneous initial values, which display significant errors as the radiation profile first forms in the discharge, values for δ_{vis} display the same behaviour expected from the true skin depth. As $\delta \propto 1/\sqrt{n_e}$, the skin depth should increase with decreasing electron number density as the total available current from the inductive coil decreases (as per the capacitive discharge profile). This behaviour is shared by δ_{vis}, confirming that the two are strongly linked.

As previously discussed, the true skin depth within the discharge may be more accurately ascertained through measurements of the plasma magnetic field strength. The value determined through experimental results is here termed δ_{mag}. Using the Biot-Savart to account for the decrease in magnetic field strength with increasing distance form its source (as detailed in Chapter 4.3.4), field strength produced at the coil surface (z = 0 mm), as well as a comparison between the measured and calculated strengths at the probe location (z = 177mm), are shown in Figure 5.17 for the low

inductive case. As can be seen, measured values of the net magnetic field strength agree well with coil-dependent values calculated. However, such agreement indicates that no component of the plasma-dependent magnetic field is measured by the probe, revealing a major limitation in this measurement technique.

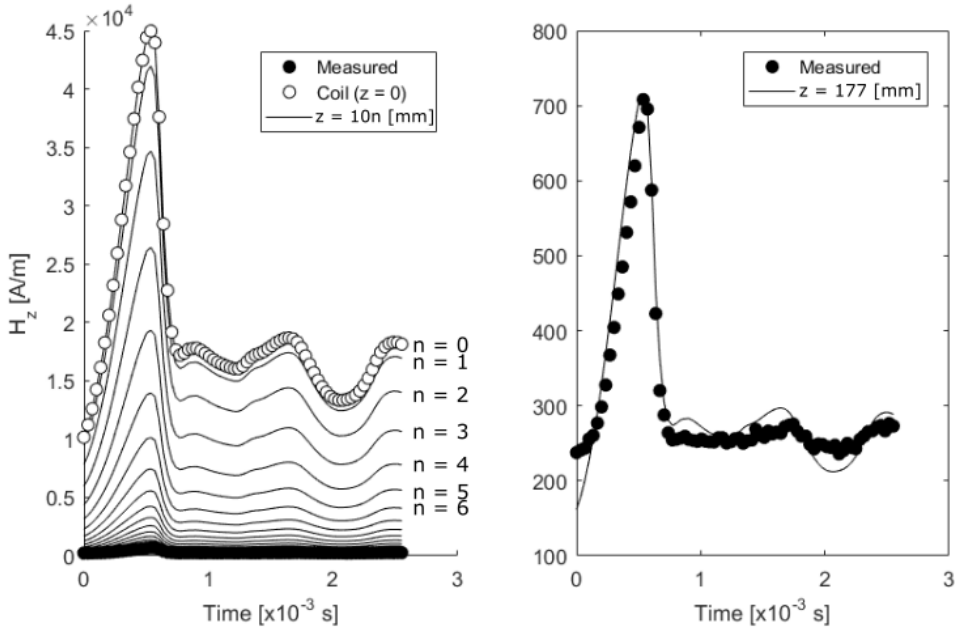

Figure 5.17: Calculated magnetic field strength with increasing (axial) distance and comparison with measured values (near field, left, and measurement location, right)

Within the radial profiles measured, no significant variation in the spatially-resolved field strength was observed. The uniformity of H_z with respect to radial position is clearly visible in Figure 5.14 (and Figures B.1 - B.12), with the measured magnetic field intensity varying only with the coil current. Considering Equation 4.14 and the degradation of magnetic field strength at the measurement position (given by Equation 4.32), the expected radial profile for a range of skin depths is shown in Figure 5.18. As can be seen, the magnitude of field strength measured at the probe location was sufficient that the observation of a number of skin depths should have been possible. The fact that the field strength displayed uniform values across the radial profile thus leads to two possible scenarios. The first scenario is that the skin depth was greater than 35 mm, with its observation being obscured by noise in the measurement device. However, given the signal uniformity was consistent for a variety of propellant and power settings (including those very close to the transition point), it is unlikely that such a value would be immediately and consistently reached regardless of the input

conditions. The second, more likely explanation is that the inductive discharge takes place at a distance from the probe significantly greater than that of the inductive coil.

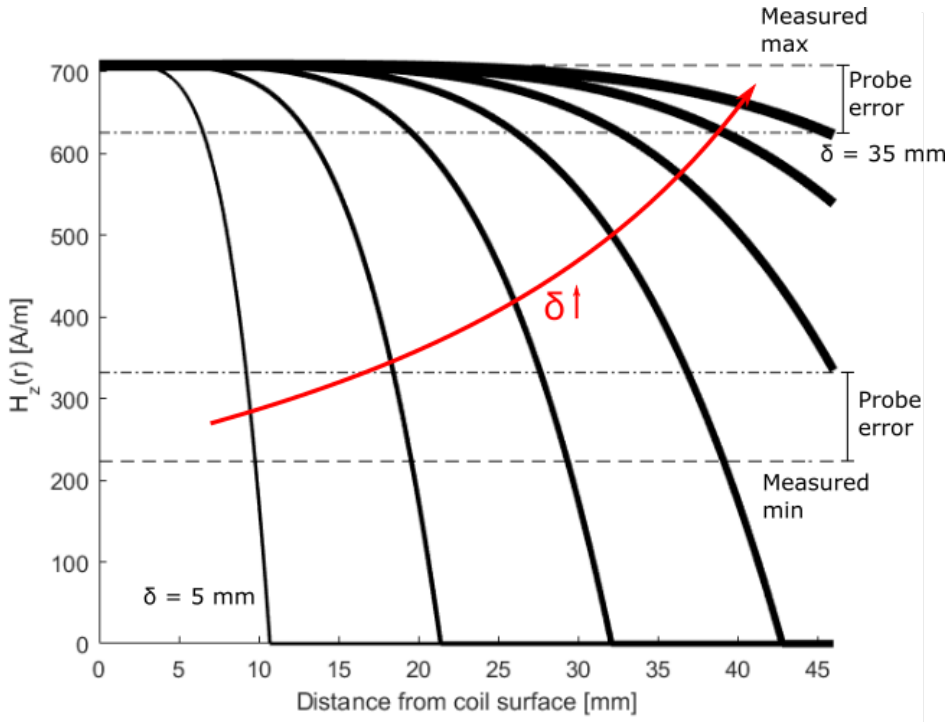

Figure 5.18: Calculated magnetic probe signal variation with increasing skin depth

During operation, current flowing through the coil is constrained by the coil geometry. The motion of each electron is hence restricted by the population of neighbouring electrons. As a result, the behaviour of the current along the length of the coil does not vary with its position, regardless of its local interaction with the plasma. This is evident in the correlation of calculated and measured magnetic field strength, with measurements of the coil current taken at the opposite end to those of the magnetic probe. The plasma discharge, on the other hand, is sustained over a discreet volume within the discharge tube. The axial location and length of the discharge volume is dependent on the input power and propellant chemical properties. Given the length of the inductive coil (0.13 m) and the decay of magnetic field strength shown in Figure 5.17, effects of a plasma volume of significantly lower length than the coil would be indistinguishable at a location far from that of its interaction with the coil. As will be shown in Section 5.5, spatially-resolved measurements of the tube wall temperature support this theory, showing the region of maximum energy coupling to the plasma to occur at a distance significantly greater than that of the coil portion closest to the magnetic probe. For this reason, experimental observations of the true skin depth were

ultimately unsuccessful. However, the time-resolved measurements of the magnetic field strength still provide useful information on assessing transitions between the discharge regimes. Significant among these results is a confirmation of the secondary effects of the inductive discharge ([50]), being its resultant azimuthal electric field opposing current within the coil and subsequent damping of the net magnetic field distribution of the thruster. The ability to assess this magnetic damping at both the beginning and end of the inductive regime period may assist in assessing aspects of the hysteresis over the discharge cycle ([45]).

Table 5.3 compares values of δ_{vis} obtained using this technique with simulated values of the true skin depth. Simulated values were obtained using the 1D model developed within this project and compared with previous simulations using a 2D model developed at IRS.

Table 5.3: Comparison of numerically calculated skin depth and experimentally determined visible skin depth for argon

Source	$\dot{m}$ [g/s]	P_{RF} [kW]	$I_{coil,max}$ [A]	f_{cap} [kHz]	δ [mm]	δ_{vis} [mm]	σ_{DC} [$\times 10^4$ S/m]
Experiment	2.97	120	1078	586	-	7.8 - 9.7	4.464 - 2.887
1D model	2.97	121	-	586	19.2	-	0.737
Lenzner [115]	1.00	-	390	600	26.0	-	0.391

As may be seen from this table, measured values of the visible skin depth are a factor of 2-2.5 lower than the true skin depth obtained using the same input conditions in the 1D model. While a discrepancy between δ and δ_{vis} is expected owing to the differing behaviour of electrons and heavy species within the discharge, the magnitude of this offset may be partially due to differences in the definitions of δ and δ_{vis}. The visible skin depth has been defined as the point of peak radiation intensity owing to heating of the propellant by the inductive coil. The true skin depth is defined as the point at which the electron number density is sufficient to cancel the coil magnetic field strength with its own opposing field. Given differences in the convective transfer of energy within the thruster, it is thus logical that the skin depth penetrates further into the discharge volume than the point of peak visible radiation. As a result, it is possible that the values of the visible skin depth used to calculate σ_{DC} should be adjusted to consider such

behaviour by means of an offset factor. For example, applying a factor of 2 to δ_{vis} (thus mirroring its distance from the thermal boundary layer on both sides of the point of peak radiation) would in turn bring values of σ_{DC} into a range more fitting with theoretical models and account for the presence of electrons past the strongly radiating zone. This would change the range of electrical conductivity measured during operation to 1.116 - 0.722×10^4 S/m. In order to assess whether such an offset factor may be used to assess the true skin depth (and hence electrical conductivity) of more complex gas mixtures, further simulations and measurements for other gas species are required. Nevertheless, the results from this argon case show that the potential for extracting electrical conductivity data using this experimental technique is present, providing a powerful tool for future discharge characterisations. It should also be noted that the two numerical tools agree reasonably well when differences in the propellant flow rate are considered as well as the coil current, which has been shown consistently in experimental conditions to exceed 1000 A. The estimated value of 390 A used by Lenzner is hence an underestimate of the conditions observed in experiments. A high input current value would in turn provide a greater degree of ionisation in the flow and cause reduced skin depth generation.

5.4 Effect of Wall Thickness Variation

While previous sections have focused largely on the interaction between propellants and the inductive coil, the discharge tube containing the plasma itself has also been found to have a strong influence on the discharge. A number of tube wall thicknesses (2.2, 3.0, and 4.0 mm) and their effect on the thruster discharge were investigated. Pure Ar and Ar:N_2 mixtures were assessed to provide a more thorough investigation than previous studies which utilised a single propellant [65]. Results from the campaign conducted by Nawaz and Herdrich are also used for comparison with measurements from this investigation. A summary of the conditions assessed is given in Table 5.4.

Table 5.4: Propellant volumetric comparison

Propellant	Composition	M_{eff} [kg/mol]	$\dot{m}_{eff}$ [g/s]
Ar	Ar	40	2.97
Ar:N_2-8	0.62 Ar + 0.38 N_2	35	2.85
Air [65]	0.77 N_2 + 0.23 O_2	29	2.75

Figure 5.19 displays the thermal (calorimetric) powers measured within this test campaign. As can be seen, the influence of wall thickness is substantial on the pure argon flow, with total thermal powers both in the discharge chamber and in the resultant jet increasing with increasing wall thickness. The point at which transitions from the low inductive to high inductive regime was also observed to decrease, being 130 kW, 115 kW, and 76 kW for the 2.2, 3.0, and 4.0 mm cases, respectively. This indicates an improved coupling efficiency between the inductive coil and the plasma flow. No change to the capacitive/low inductive transition was observed due to the low powers required to generate the inductive discharge in Ar (< 1 kW).

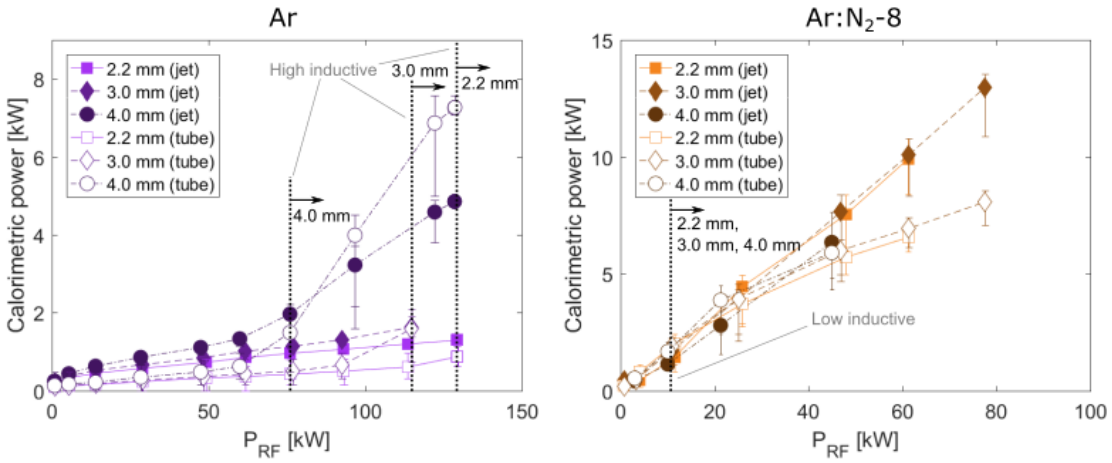

Figure 5.19: Calorimetric thermal power of the jet and discharge tube for Ar and Ar:N_2-8

Results for the argon-nitrogen mix are substantially different from those of pure argon. In these experiments, thermal power showed minimal variation with increasing wall thickness, with each of the three thicknesses requiring 11 kW to complete the transition to the low inductive regime. No transition to the high inductive mode was

achieved. The impact of tube thickness on thermal power for Ar:N_2-8 was hence negligible.

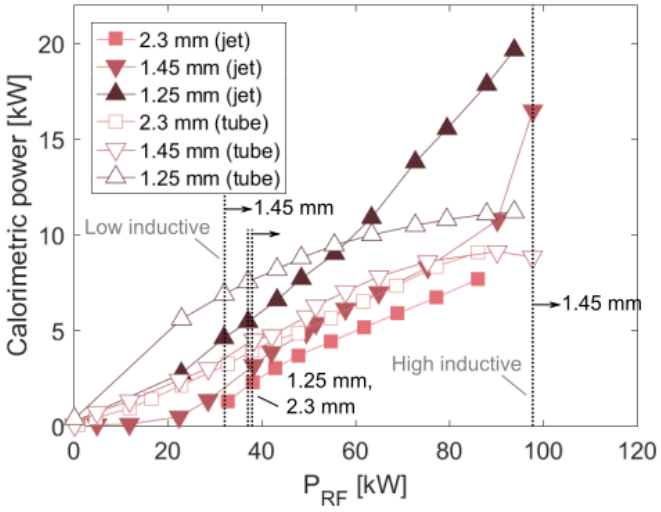

Figure 5.20: Calorimetric thermal power for the jet and discharge chamber (tube) utilising air (adapted from [65])

Previous experiments using air (Figure 5.20) show an increase in thermal power (both tube and jet) for decreasing wall thicknesses. At the time of investigation, the authors proposed this behaviour as being applicable to all gases, with a reduction in the tube wall thickness increasing the net magnetic field strength applied to the plasma (as discussed in Section 4.2.3). However, while the net thermal power did increase, reductions in wall thickness also led to a change in the discharge coupling with the inductive coil. Variations in the input power at the transition between capacitive and low inductive operation were similar for the three thicknesses; the 2.3 mm and 1.25 mm conditions produced transitions at 32 kW, while the 1.45 mm condition recorded a transition at 28 kW. Though this difference is minor, the occurrence of the low inductive to high inductive transition for only the 1.45 mm condition is not. This indicates that 1.45 mm represented an optimal thickness for the propellant and mass flow rate tested. Given that the 1.25 mm air condition showed poorer thermal coupling for a higher net magnetic field strength, as did all three of the Ar conditions, the effect of wall thickness on the discharge must hence consider more than the magnetic field strength in the discharge volume. A more comprehensive assessment must also consider the propellant chemical properties and the requirements of the different discharge regimes. An analysis combining these factors is performed in this section.

The input powers required to complete transitions between the discharge regimes for the three propellants considered in this section are shown in Figure 5.21. Despite being primarily composed of Ar, the magnitude of thermal power recorded in the Ar:N_2-8 experiments show the clear influence of N_2 chemical properties for the same reasons discussed in Section 5.1. Jet thermal powers recorded for the mixed propellant are up to a factor of 10 higher than pure Ar for the 2.2 mm and 3.0 mm conditions (Figure 5.19). A comparison of visible radiation emitted by the Ar and Ar:N_2-8 conditions, shown in Figure 5.22, also highlights the impact of N_2 on the discharge chemistry, thermal boundary layer, and skin depth. As a result, the effect of chemical properties, particularly thermal conductivity and specific heat capacity, must be considered when assessing the behaviour of the three propellants.

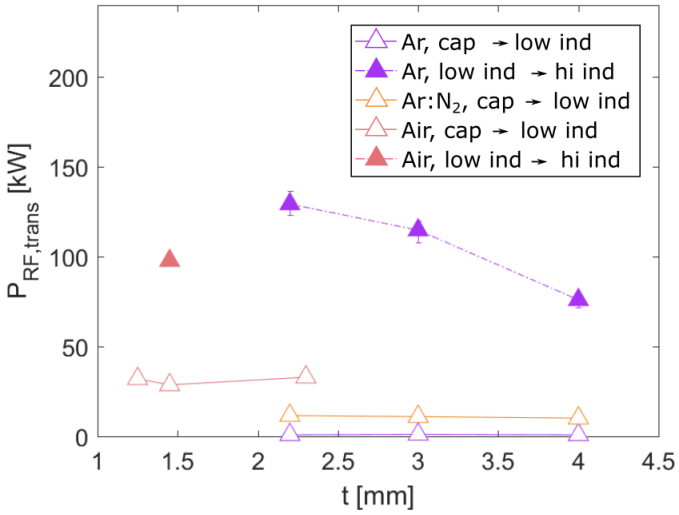

Figure 5.21: Discharge transition input powers for Ar, Ar:N_2, and air

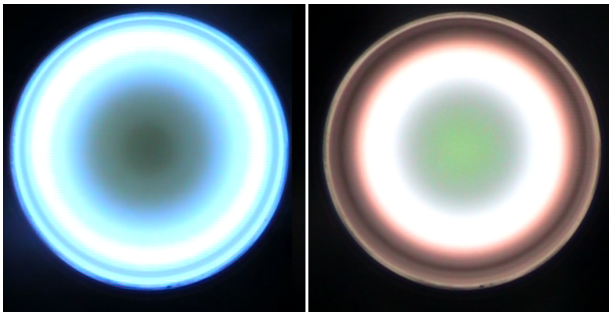

Figure 5.22: Inductive discharge cross-sections for Ar (left) and Ar:N_2 8 (right)

As discussed in Section 4.2.3, increasing the chamber wall thickness acts to decrease the net magnetic field strength to which charged particles within the plasma are

exposed. However, this statement is true for all dielectric or non-conductive media, requiring consideration of the thermodynamic relationship between the discharge chamber wall and the thermal boundary layer. Consider the inductive discharge cross-section shown in Figure 5.23, where $\dot{Q}_H$ is the heat flux generated from the externally-applied coil magnetic field and $\dot{Q}_{diff,1}$ and $\dot{Q}_{diff,2}$ are the diffusion of thermal power radially inwards and outwards from the skin depth, respectively.

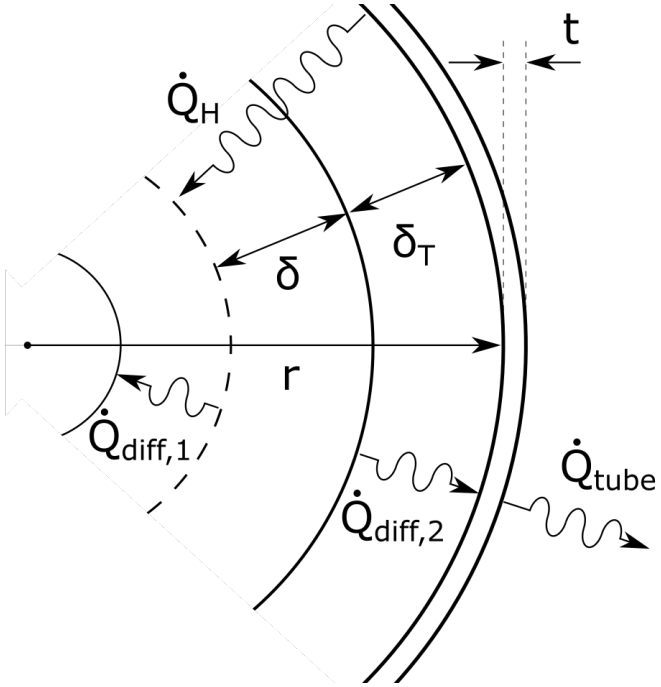

Figure 5.23: Notational diagram of thermodynamic and electromagnetic behaviour within the inductive discharge

As the wall thickness is decreased, the thermal energy used to establish the skin depth should increase due to the greater net magnetic field strength incident on the plasma. However, decreasing the tube wall also increases the conductive heat flux from inner to outer tube wall. As a result, a greater quantity of $\dot{Q}_{diff,2}$ is transferred to the tube cooling water and the internal wall temperature is reduced. Discharges within this system are of a relatively high pressure (500 - 2000 Pa), making heavy particle collisions important with regard to the distribution of energy in the discharge volume. A lower discharge chamber wall temperature would hence extract more energy from the skin depth and increase the thermal boundary layer thickness [2].

If the thermal boundary layer is treated as a zone with negligible ionisation degree due

[2]This process assumes that the effect of lowering the chamber wall temperature dominates that of supplying more energy to the flow through the increased incident magnetic field strength.

to its relatively low temperature, then the thickness of the boundary layer may also be considered a dielectric separation between coil and plasma. This is an important assumption given that, as seen in Figure 4.6, electric fields in the coil and azimuthal plasma current (used to form the skin depth) act in opposing directions. Therefore any dielectric medium separating the two fields will have an influence on the magnitude of the resultant azimuthal field within the plasma. This includes the Coulombic interaction between the coil and discharge. The assumption of such behaviour within the discharge can be used to explain the results presented in this section.

The first case considers the pure argon discharge. As can be observed in Figure 5.22, thermal boundary layers for argon are much smaller than those involving nitrogen due to argon's low specific heat capacity and low ionisation energy. As a result, the primary dielectric separation in this discharge is produced by the discharge chamber wall and the net magnetic field strength remains high due to charged particle proximity to the coil surface. This explains the observed behaviour, with the increase in wall thickness acting primarily to separate the opposing electric (and magnetic) fields, while the degree of ionisation in the skin depth region remains high due to a small thermal boundary layer and hence high net magnetic field strength.

The second case considers the non-monatomic discharges (Ar:N_2-8 and air), particularly the 1.45 mm tube tested for air, beyond which discharge transitions were not observed. In these situations, the high specific heat capacity and thermal conductivity of the propellants produce thermal boundary layers significantly larger than the tube wall thickness. As a result, increases in the wall thickness beyond a particular value have minimal effect, while certain reductions (such as that from 2.3 mm to 1.45 mm) provide a balance in net magnetic field strength and separation between the opposing currents. This balance can however be upset, as in the case of the 1.25 mm wall. In this tube configuration, the net electrical energy delivered to the plasma was increased, though elevated convection losses to the thruster cooling water prevented the discharge from developing sufficient ionisation to transition to the high inductive mode.

Measurements obtained in this study have hence helped to develop a greater understanding of the impact of tube wall thickness on the resultant plasma discharge. Future propellant configurations investigated may make use of this information,

considering not only mechanical separations from component geometry, but also gasdynamic separations generated within the discharge volume itself.

In addition to coupling, the impact of wall thickness on the thermal efficiency for a given propellant is also of interest. Figure 5.24 shows the total and effective thermal efficiencies of Ar and Ar:N_2-8. As expected, total thermal efficiency for Ar remains low except in the case of the 4.0 mm condition, due to the earlier transition to the high inductive regime. However, an analysis of the effective efficiency shows that this increase is dominated by thermal power within the discharge chamber rather than the jet. Hence the usable thermal power for thrust applications in fact decreases.

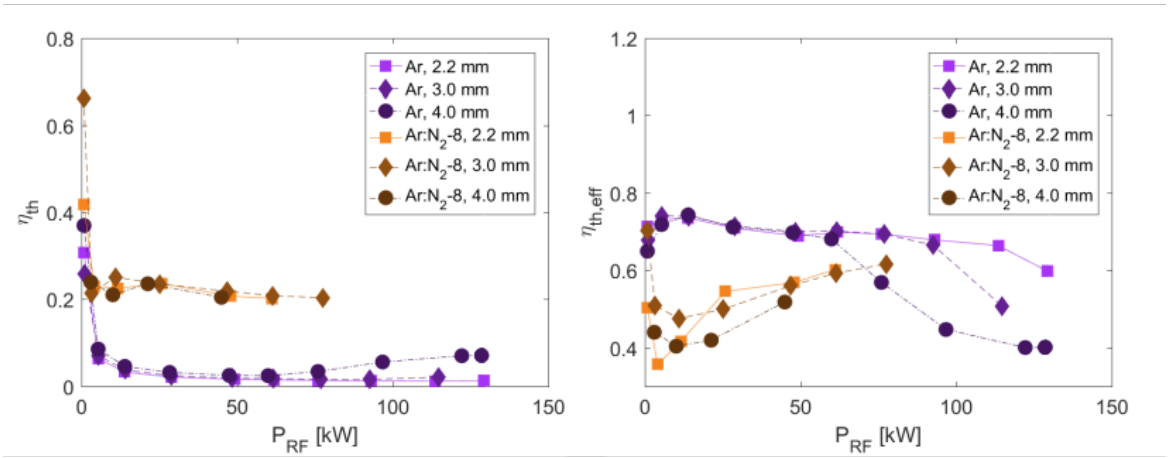

Figure 5.24: Total and effective thermal efficiency for argon and Ar:N_2-8

Ar:N_2 maintains a marginally decreasing total thermal efficiency above the asymptote of 20 %, with minimal variation between chamber thicknesses. However, the effective efficiency shows that usable thermal power within the flow is steadily increasing. Improved performance for thinner wall thicknesses is seen at low power levels, though at high powers the three tube thickness converge to produce similar results.

Results for air show that while the total thermal efficiency produced by the 1.25 mm condition is significantly higher than that of the other two tube, the 1.45 mm condition produced the highest effective thermal efficiency. This is due to the use of the high inductive mode coupling and highlights the need to consider the effect of discharge regimes within the thruster from a number of different perspectives.

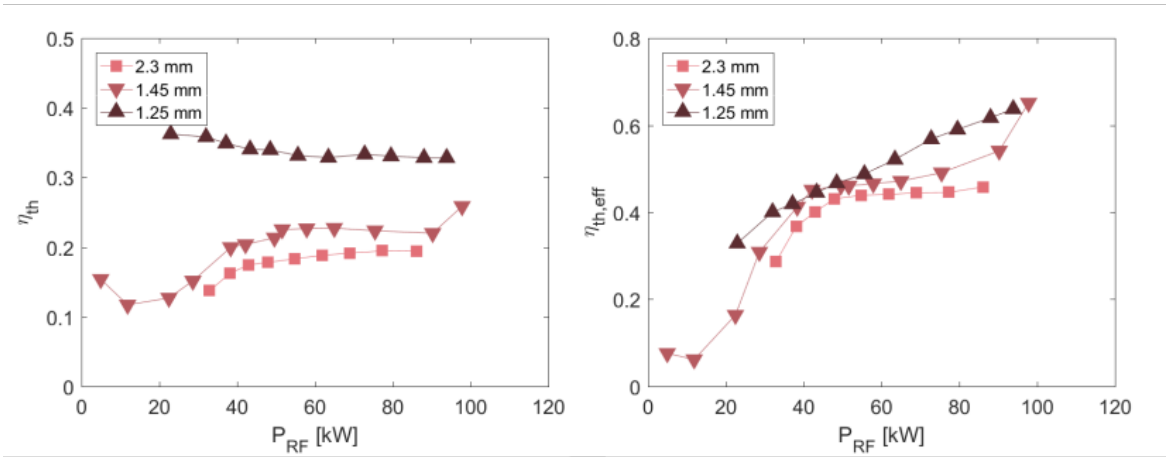

Figure 5.25: Total and effective thermal efficiency for air (adapted from [65])

The impacts of wall thickness presented in this section highlight the strong interaction between the propellant and the discharge chamber, as well as providing a more comprehensive assessment of power coupling with respect to the propellant chemical properties. When considering the dielectric separation between plasma and coil, both the discharge chamber wall and the discharge thermal boundary layer play a role in determining thruster performance. The combination of these two aspects provide further information on the balance of electromagnetic and thermodynamic behaviour within the discharge chamber.

Understanding this behaviour is of particular importance when determining the desired propellant configuration for a particular mission. As seen through the results in Section 5.1, mixtures of dissimilar gases can exhibit strong characteristics of a minority constituent, with strong implications on system performance for a given thruster geometry. As a result, propellants and thruster components may be chosen to take advantage of favourable performance of a particular gas, or the availability of a particular resource. In the context of space operations, this may correlate to long-range, multi-destination missions, or those centred around a propellant supply of varying/cyclic chemical composition. The ability to react to such changes in the operational environment, or tailor a mission simply by supplying an existing propulsion system with a particular propellant mixture, is an example of inductive propulsion system's inherent flexibility and potential for future space operations.

5.5 Discharge Tube Wall Temperature

As discussed in Section 4.2.3, different measurement techniques were used in order to obtain spatially-resolved data on the discharge tube wall temperature. While the analytical and adhesive thermometer techniques were applied to a number of plasma conditions (with results given in Table 5.6), the thermal paint technique was used only when testing Ar:N_2-8. The tube heat flux recorded during this test was 5782 W [3]. This condition was chosen to provide sufficient flow enthalpy (and hence wall temperature) at moderate input powers as well as avoiding the use of chemically reactive species such as oxygen.

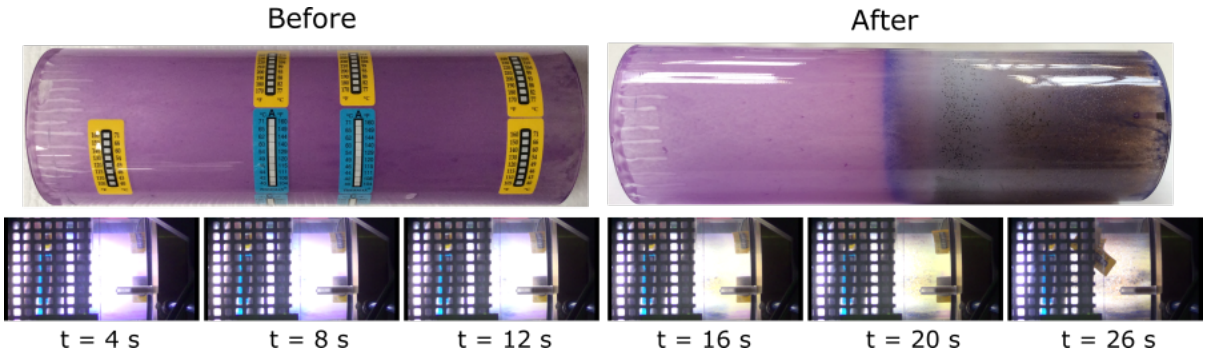

Figure 5.26: Thermal paint before and after exposure to the plasma discharge

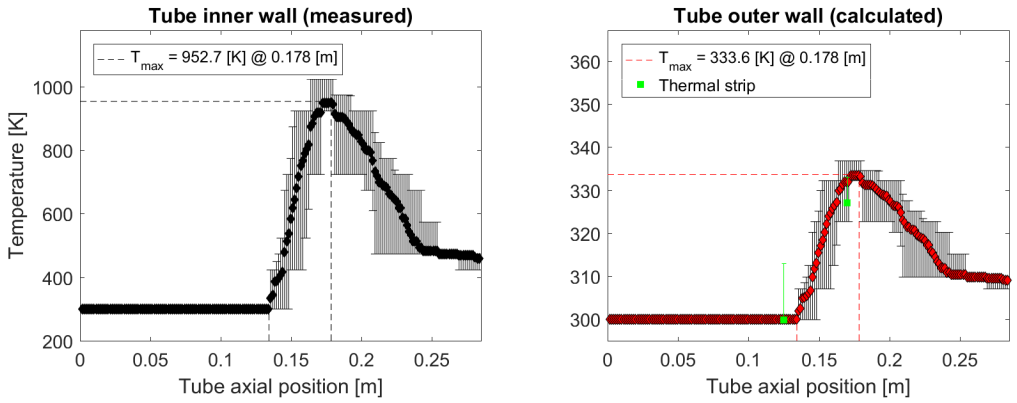

Figure 5.27: Tube wall inner (measured) and outer (calculated) wall temperatures from thermal paint method and point measurements from adhesive thermometers

[3]Note that in this section, W, rather than kW, is used to quantify heat flux to the tube. This is done due to the greater importance placed on these values when calculating absolute wall temperature, in contrast to previous sections which used $\dot{Q}_{\text{tube}}$ to highlight order of magnitude difference in different propellant conditions.

Images of the painted tube before and after testing are given in Figure 5.26, with the subsequently calculated tube wall temperatures (inner and outer surface) shown in Figure 5.27. As can be seen from these figures, no significantly elevated wall temperatures were recorded until at least the centre of the tube, correlating to the mid-point of the inductive coil. While the minimum activation temperature of the paint (353 K) limits the resolution of this initial transition, the point of maximum recorded temperature occurs between the final two coil turns (closest to the thruster outlet). The paint also reveals steep thermal gradients, with the inner wall temperature increasing by almost a factor of 3 over a small portion of the tube length. Plotting the cumulative tube heat flux with axial position, shown in Figure 5.28, approximately one third of the total integral heat flux is incident on the tube over 15 % of its length. The location of maximum heating determined using this method agrees well with previously recorded tube failures, caused by exceeding the integral cooling powers listed in Figure 4.7. It should be noted that the increasingly large error bars with increasing axial position result from a combination of errors in the paint technique and the averaging of measurements at locations around the tube circumference. A total of 10 discrete strip samples were used for the assessment. Comparisons between average temperatures obtained using the paint method and integral cooling method are shown in Table 5.5. The two methods show good agreement, though the similarity in final temperature values, despite a significant (7 %) difference in the respective heat flux values. This agreement adds confidence to the results obtained through the thermal paint method, providing new data on the distribution of thermal energy within the discharge tube.

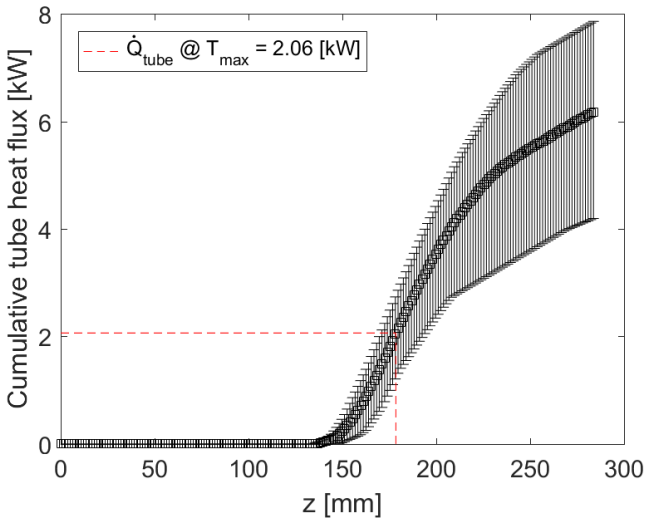

Figure 5.28: Cumulative tube wall heat flux with axial position

Table 5.5: Total tube heat flux and average wall temperatures from integral and thermal paint methods

Method	$\dot{Q}_{\text{tube,T}}$ [W]	$T_{\text{wall,in}}$ [K]	$T_{\text{wall,out}}$ [K]
Integral	5782	480.34	309.08
Thermal paint	6203	482.99	309.73

Table 5.6 lists the results from a series of conditions investigated using the adhesive thermometers. While loose agreement can be seen in some of the results, the overall technique produced lower confidence results due to mechanical limitations.

The first of these limitations was the discrepancy between thermometer strips applied in close proximity to the inductive coil. The two brands of adhesive thermometers utilised showed different final temperatures when applied at the same axial position. This is reflected in Table 5.6, with one of the brands displaying tube surface temperatures significantly greater than the other (marked in grey) and above the boiling temperature of the tube cooling water. The lack of phase change in the water flow during these tests (a phenomenon which has been clearly observed in previous tests) suggests that the fluid used within the thermometers was disturbed during testing. The spiral nature of the coil may have been an influencing factor in these contrary measurements, with the dimensions of the adhesive strips (51 x 18 mm) being comparable to the distance between coil turns. Hence the different thermometers may have been exposed to a significant range of temperatures depending on their position with relation to the coil contour. Other potential sources are heating from the electromagnetic fields or simply faults in the thermal strip production.

Table 5.6: Local tube (outer) wall measurements obtained using adhesive thermometer technique

				$T_{wall,out}(z)$ [K]					
	$\dot{V}$	t	$\dot{Q}_{tube,T}$	0.040	0.080	0.125	0.170	0.215	0.255
	[l_n/min]	[mm]	[W]	[m]	[m]	[m]	[m]	[m]	[m]
Ar:N_2	67:41	3	5782	(fail)	-	< 313	327-333	-	(fail)
Ar:N_2	67:41	3	6279	(uc)	(uc)	(uc)	(uc)	(uc)	> 344
							(455)	(400)	
							(melt)		
Ar	100	4	6601	< 313	313-316	> 344	> 344	(fail)	338-344
							(534)		
						(melt)	(melt)		
Ar:N_2	67:41	4	6605	< 313	< 313	< 350	> 389	(uc)	338-344
							(melt)		
Ar:N_2	67:41	3	8555	-	-	-	-	> 344	> 344

(fail) = failure of thermometer adhesive

- = no measurement taken at this position

(uc) = no clear, consistent result

(melt) = destruction of thermometer body observed

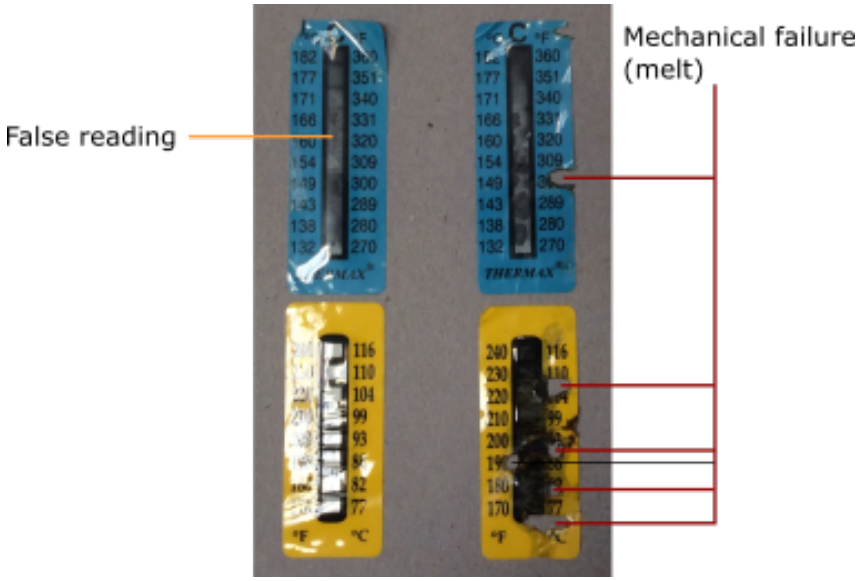

Figure 5.29: Examples of thermometer discrepancy and mechanical (melt) failure during the Ar:N_2-8 4 mm test

The other major limitations of the adhesive thermometer technique were material failures of both the adhesive and thermometer (plastic) body, designated *fail* and *melt* in Table 5.6, respectively. As shown in the footage of tests with this technique (Figure 5.26), strips often detached from the tube during operation, voiding measurements at those locations. Such detachment was often caused by elevated tube temperatures, though was also observed at room temperature water tests, with the flow of cooling water loosening the strips. Failures of the thermometer body itself were linked to proximity to the inductive coil, with the lack of cooling water between the two resulting in localised destruction. An example of this melting damage is given in Figure 5.29.

5.6 State of Inductive Propulsion and Alternative Propellants

The previous sections have reported on thruster performance using alternative propellants, techniques to assess the discharge and propellant utilisation, and impacts of the thruster geometry on the resultant plasma. In order provide context of these results, this section will address the performance of the thruster with regard to the wider EP field and how it may be improved in the future.

Table 5.7: Maximum performance conditions of the propellants tested

Propellant	$\dot{m}$ [g/s]	F_{MAX} [N]	$I_{sp,MAX}$ [s]	P_{RF} [kW]	η_F [%]	F/P_{RF} [mN/kW]
O_2	2.50	5.8	236.7	105	6.4	55.4
Ar:O_2-5	3.49	7.7	224.2	113	7.5	68.3
Ar:O_2-6	3.69	7.9	216.1	116	7.3	67.8
N_2	2.23	2.0	91.7	44	2.0	45.9
Ar:N_2-9	3.36	5.7	172.3	78	6.2	72.8
Ar:N_2-10	3.58	7.8	221.4	120	7.1	65.0
Ar:N_2-11	3.72	7.5	203.8	113	6.7	66.3
CO_2	2.64	2.5	96.1	42	2.8	59.3
Ar:CO_2-14	3.28	6.7	183.3	76	9.0	88.7
Ar:CO_2-15	3.41	6.4	173.8	62	9.7	102.3

Table 5.8: Comparative performance of other EP systems with alternative propellants

Propellant/ Thruster	$\dot{m}$ [g/s]	F_{MAX} [N]	$I_{sp,MAX}$ [s]	P [kW]	η_F [%]	F/P [mN/kW]
O_2						
RIT [6]	2.03×10^{-4}	6.00×10^{-3}	3016	0.45	39.5	13.3
N_2						
RIT [6]	1.77×10^{-4}	5.25×10^{-3}	3017	0.45	34.5	11.7
HET [6]	2.27×10^{-3}	21.0×10^{-3}	944	1.06	21.8	23.6
HHT [10]	4.86×10^{-3}	39.0×10^{-3}	818	1.86	21.8	21.0
CO_2						
HET [9]	3.95×10^{-4}	3.25×10^{-3}	838	1.50	17.8	21.7

Table 5.7 shows the maximum thrust and I_{sp} conditions obtained for O_2, CO_2, N_2, and their combinations with argon, including their respective input powers and thrust efficiencies. Values for F/P_{RF} recorded within these tests are comparable (or in some cases, superior) to some of the conventional thrusters discussed in Chapter 2. However, values for I_{sp} are more than a factor of 10 lower than those achievable with other EP

systems, particularly ion thrusters. As a result, thrust efficiency for the IPG7 is also significantly lower than the other EP systems assessed. The performance of these other EP systems is tabulated in Table 5.8.

The highest I_{sp} recorded in this work (236.7 s for O_2) is still well below the 350 s value used to justify the use of EP over classical chemical propulsion. However, given the present, basic design of the IPG7, a number of possibilities exist to improve values of I_{sp} to a competitive level. Combined with the system's high thrust and thrust-to-power ratio, the potential for inductive propulsion systems to play a key role in future space operations is high.

The primary limitation to propellant exhaust velocity in this system can be described in terms of the suboptimal thruster geometry. While the electrothermal mechanism generates thrust through heating of the working fluid, the constant cross-section of the IPG provides no preferential expansion (and hence acceleration) of the gas, as is the case with other electrothermal EP classes such as arcjets. As a result, the implementation of a mechanical nozzle should provide significant additional jet velocity through dedicated expansion and acceleration of the flow. However, due to the scope of this project, the development of a mechanical nozzle is not feasible in the time available. Such a task is seen as a primary objective for future work on this topic.

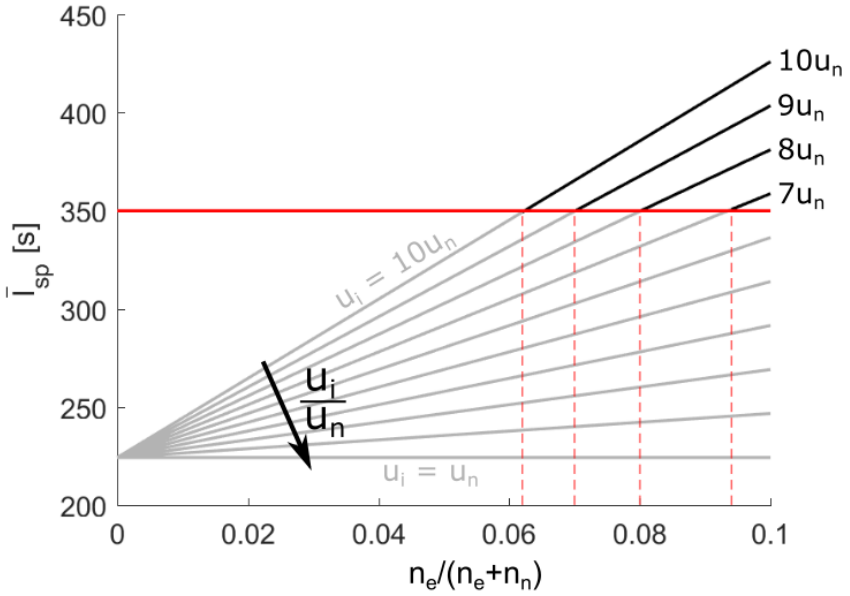

Figure 5.30: Effective mean thruster exhaust velocity after charged particle acceleration

Another method of increasing the specific impulse is to apply an external,

electromagnetic or electrostatic acceleration mechanism to the flow, thus increasing the charged heavy particle velocity to levels comparable with other EP systems. However, developed originally as a tool for planetary entry simulation, the primary focus of the IPG is to produce flows of high enthalpy rather than a significant degree of ionisation. Previous studies have estimated this degree of ionisation as less than 10 % [115, 116]. This limits the impact of charged species on the effective average thruster impulse. Figure 5.30 shows the effective (mean) specific impulse with respect to flow ionisation degree ($n_e/(n_e + n_n)$) for a number of charged particle acceleration gains, calculated as:

$$\bar{I}_{sp} = \frac{1}{g_0}\left(u_i\left(\frac{n_e}{n_e + n_n}\right) + u_n\left(1 - \frac{n_e}{n_e + n_n}\right)\right) \tag{5.2}$$

where u_i and u_n are the ion and neutral exhaust velocities, respectively. The baseline value for u_n is taken from the Ar:O_2-5 as a reference.

Accelerating charged heavy species to 10 times the neutral species velocity would provide the necessary mean propellant velocity for ionisation degrees in excess of 6 %. While this is a feasible ionisation degree for present IPG operation, the flux of propellant through this system is significantly larger than that of present electrostatic or electromagnetic systems. As such, the acceleration mechanism would need to be carefully designed in order to interact with a sufficient proportion of the charged species population. Additionally, since such an acceleration mechanism has not been developed for such high propellant flows, no comment can presently be made about the amount of additional power required to achieve such performance and its subsequent influence on parameters such as the thrust efficiency.

The implementation of thruster acceleration mechanisms, whether mechanical or electromagnetic, will have a significant impact on the thruster discharge. The measurement techniques developed within this project will therefore be of extensive use when assessing new thruster geometries, particularly with respect to the utilisation of propellant in the discharge. The ability to accurately characterise the discharge regime for a particular thruster geometry will assist in analysing whether plasma entering the acceleration volume has been effectively heated within the discharge chamber. Furthermore, spatially-resolved information on the tube wall temperature can be used to improve future cooling systems and reduce thermal losses in the thruster. The combination of these factors can hence be used for improved operation with alternative propellants in an inductive propulsion system.

Chapter 6

Outlook

In order to continue developing the capabilities of future inductive propulsion systems utilising alternative propellants, a number of design aspects may be identified as being of critical importance. While the thrust and specific impulse of the system were greatly improved using propellant modification, the ultimate thrust capabilities of the system are still below the desired threshold separating electric and chemical propulsion. As a result, improvements to the thruster geometry and acceleration mechanisms are necessary. Such developments could be achieved through the following:

- Develop mechanical and magnetic nozzles to be adapted to current thruster geometry;
- Identify means to improve the position of the inductive coil with respect to discharge tube, including reducing tube length prior to coil opening;
- Investigate new coil cross-sections to increase coupling efficiency (and decrease input power required for transitions).

Such modifications to the thruster geometry may be assessed using the measurement techniques presented in this thesis, which depend only on the interaction between propellant and coil. These techniques may also be improved to yield greater information regarding the discharge characteristics. Examples of such improvements are:

- Implement segmented HOKA probe (rather than present integral design) to allow non-uniform current flow over coil cross-section to be investigated;
- Coupling visible skin depth measurements with monochromatic filters or spectroscopy to identify the distribution of particular species within the discharge;
- Investigate potential presence of helicon wave signatures in discharges in order to better clarify mechanisms behind the high inductive regime.

Implementing the modifications listed here would serve not only to improve the performance and understanding of the system as a propulsion device, but would also allow the planetary entry simulation capabilities of similar inductive systems to be significantly increased.

In addition to these tasks, additional simulations and measurements of the true and visible skin depths for gases other than Ar (most likely O_2 or N_2 given their previous implementation in plasma-oriented models) would assist in measuring discharge electrical conductivity non-intrusively during operation.

Chapter 7

Conclusions

The aim of this work was to implement and compare a number of alternative propellants in an electrodeless propulsion system. This comparison was to include a particular focus on the thruster discharge regimes, including the development of novel techniques to allow their accurate assessment. In doing so, progress can be made towards developing space propulsion technology capable of operating and refuelling without direct contact with Earth.

Through these investigations, a clear benefit in combining propellants was observed. These propellant combinations utilised the low ionisation energy of the noble species (Ar) with the high thermal conductivity of molecular species (O_2, N_2, CO_2). The complimentary combination of species properties produced significantly greater net thrust and specific impulse. With the implementation of additional acceleration mechanisms (such as a mechanical nozzle), these values can be further improved and present competitive alternatives to conventional EP systems.

Thruster performance in the IPG is strongly linked to the plasma electromagnetic discharge regime. Through the choice of gas species, transitions to higher coupling efficiency regimes can be achieved with lower input powers, allowing more of the total supply power to be transferred to the propellant.

In order to better understand electromagnetic transitions in the IPG, several measurement techniques were developed. Temporally-resolved measurements of the inductive coil current revealed the link between the discharge regime and the dominant characteristic coil frequency at discreet intervals in the cycle. As the discharge enters

the inductive regime, an increase in coil discharge frequency is observed as a result of impedance matching between plasma and coil. This identification allowed the proportion of time spent in the two regimes to be quantified and hence the stability of the discharge to be quantified. Discharges which combined atomic and molecular propellants displayed inductive coupling for up to 94 % of the total discharge cycle. This is compared to 71 % recorded for a discharge using only the molecular propellant. Such a measurement represents a significant improvement on previous investigative techniques, allowing the first assessment of how effectively propellant is utilised from an electrodynamic perspective.

A new measurement technique was also developed to record values of the visible and magnetic skin depths during operation, with successful measurements taken for the visible component but not for the magnetic. Comparisons of the visible skin depth, measured experimentally, and the true skin depth, determined numerically, were also performed. The visible skin depth was shown to be approximately twice that of the calculated skin depth, though this difference is proposed to be rectified by considering the highly radiating zones either side of the peak.

The lack of variation in the radial profile of magnetic field strength, combined with spatially-resolved measurements of the discharge tube wall temperature, provide strong arguments that the inductive discharge takes place at a significant distance downstream of the first coil section.

Variations in the discharge tube wall thickness were performed for chemically dissimilar gases (Ar and an Ar:N_2 combination) and compared to a similar study performed in the past with air. Measured thermal power with Ar was higher for thicker tube walls, and discharge regime transitions were recorded at significantly lower input powers. The combined Ar:N_2 propellant was dominated by N_2 chemical properties and displayed marginally lower performance with increased wall thickness. This behaviour was linked to the thermal boundary layer in the flow behaving as a secondary dielectric separation after the tube wall. This highlights the differences in propellant interaction with the thruster and the influence of minor constituents in combined propellants.

In working towards the objective of developing more flexible, refuellable spacecraft for future operations, the sum of the work reported on in this thesis highlights the potential to greatly alter thruster performance through propellant composition, as well as presenting non-intrusive methods through which the effective utilisation of propellant may be assessed accurately and dynamically.

Appendix A

Propellant Conditions and Chemistry

Relevant chemical properties and reaction data for the species considered are given in Table A.1. Table A.2 lists the propellant conditions assessed within this work.

Table A.1: Chemical properties and reaction data for the species considered in this work [117–119]

	M [kg/mol]	ρ_{298K} [kg/m^3]	$c_{p,298K}$ [kJ/kg·K]	κ_{298K} [kW/m·K]	$\Delta H_{f,298K}$ [kJ/mol]	$\Delta H_{i,298K}$ [kJ/mol]
Ar	40×10^{-3}	1.784	0.520	1.835×10^{-5}	-	1521
O_2	32×10^{-3}	1.429	0.919	2.736×10^{-5}	O=O, 498.3	1165
O	16×10^{-3}	-	-	-	-	1314
N_2	28×10^{-3}	1.250	1.040	2.703×10^{-5}	N≡N, 946.0	1503
N	14×10^{-3}	-	-	-	-	1402
CO_2	44×10^{-3}	1.977	0.844	1.771×10^{-5}	C=O, 749.0	1329
CO	28×10^{-3}	1.250	1.043	2.722×10^{-5}	C=O, 749.0	1352
C	12×10^{-3}	-	-	-	-	1086

Table A.2: Propellant flow rates tested

	Ar		O_2		N_2		CO_2		$\dot{m}_{eff}$	Particle flux	Proportion (volume)	
	[l_n/min]	[g/s]	[l_n/min]	[g/s]	[l_n/min]	[g/s]	[l_n/min]	[g/s]	[g/s]	[$\times 10^{24}$ 1/s]	Ar	X
1	100	2.97	-	-	-	-	-	-	2.97	2.69	1.0	-
2	67	1.99	-	-	-	-	-	-	1.99	1.80	1.0	-
3	50	1.49	-	-	-	-	-	-	1.49	1.34	1.0	-
4	-	-	105	2.50	-	-	-	-	2.50	2.82	-	1.0
5	75	2.23	53	1.26	-	-	-	-	3.49	3.44	0.59	0.41
6	90	2.68	43	1.01	-	-	-	-	3.69	3.56	0.68	0.32
7	-	-	-	-	107	2.23	-	-	2.23	2.88	-	1.0
8	67	1.99	-	-	41	0.85	-	-	2.85	2.90	0.62	0.38
9	75	2.23	-	-	54	1.13	-	-	3.36	3.47	0.58	0.42
10	90	2.68	-	-	43	0.90	-	-	3.58	3.57	0.68	0.32
11	100	2.97	-	-	36	0.75	-	-	3.72	3.65	0.74	0.26
12	-	-	-	-	-	-	80	2.64	2.64	2.16	-	1.0
13	-	-	-	-	-	-	53	1.76	1.76	1.44	-	1.0
14	90	2.68	-	-	-	-	32	1.05	3.73	3.28	0.74	0.26
15	100	2.97	-	-	-	-	27	0.89	3.86	3.42	0.79	0.21

Appendix B

Transient Discharge Behaviour Still Images

Figures B.1 - B.12 show the transient discharge behaviour described in Section 5.3 as still images rather than the embedded video format.

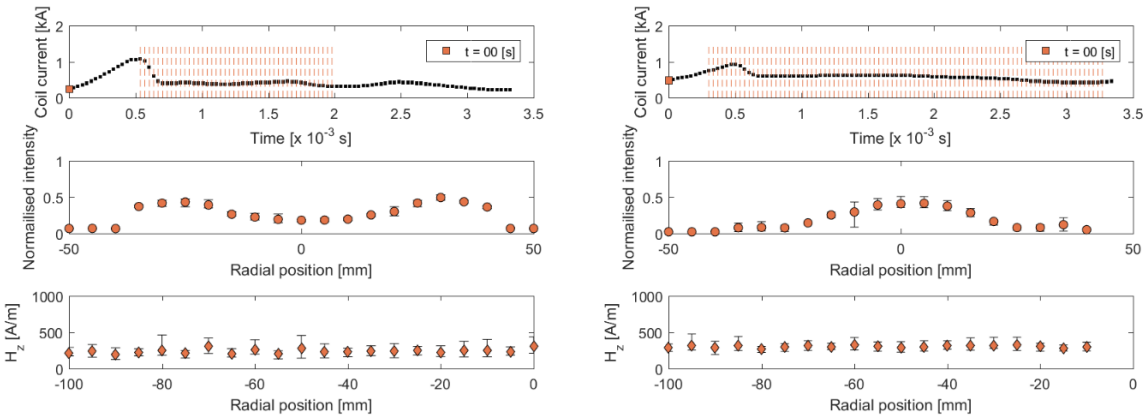

Figure B.1: Low inductive (left) and high inductive (right) discharges, t = 0.0 ms

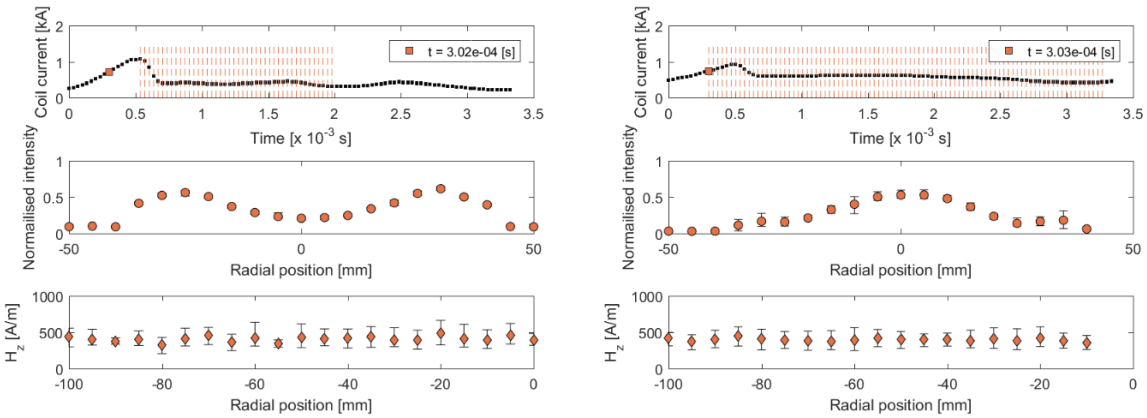

Figure B.2: Low inductive (left) and high inductive (right) discharges, t = 0.3 ms

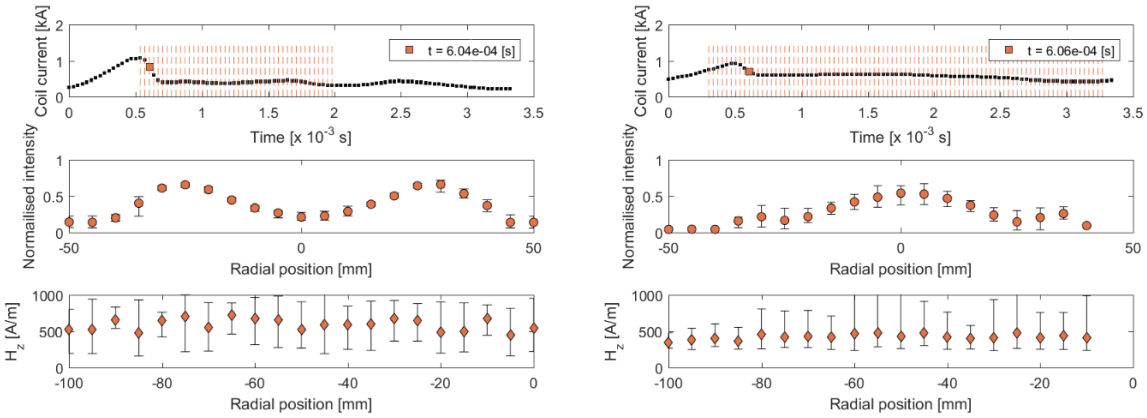

Figure B.3: Low inductive (left) and high inductive (right) discharges, t = 0.6 ms

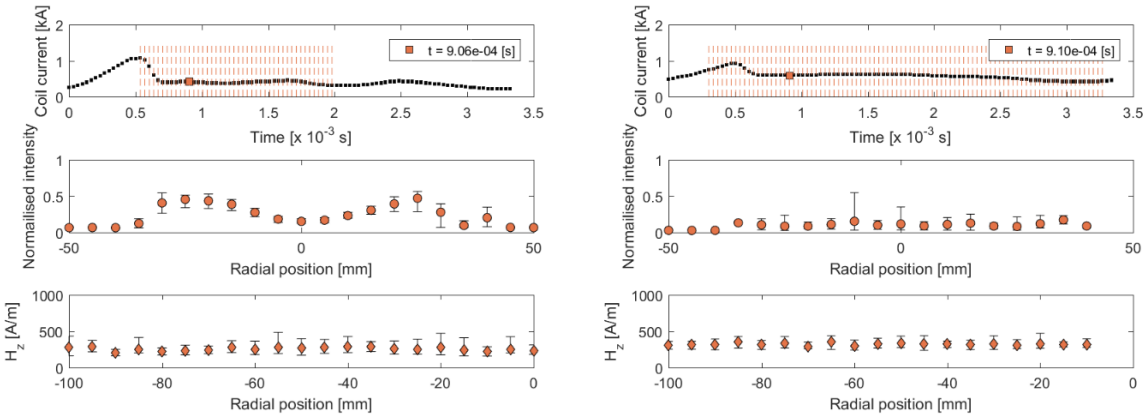

Figure B.4: Low inductive (left) and high inductive (right) discharges, t = 0.9 ms

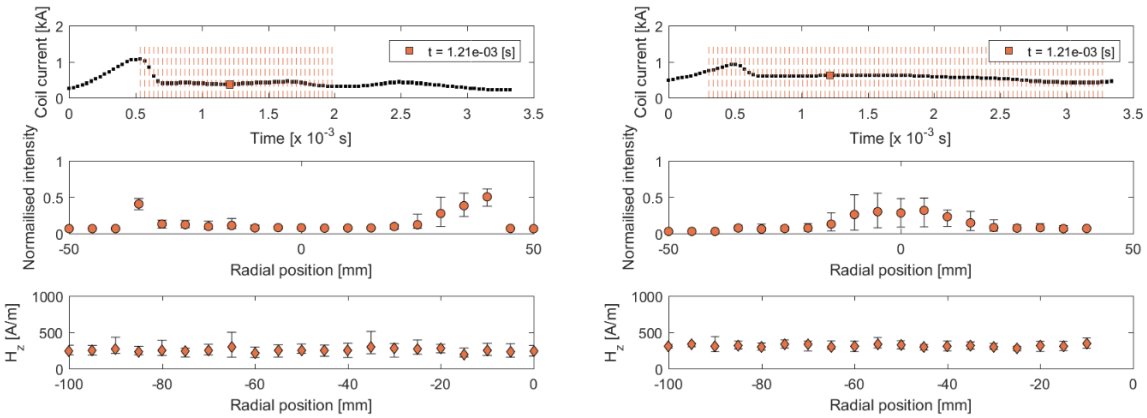

Figure B.5: Low inductive (left) and high inductive (right) discharges, t = 1.2 ms

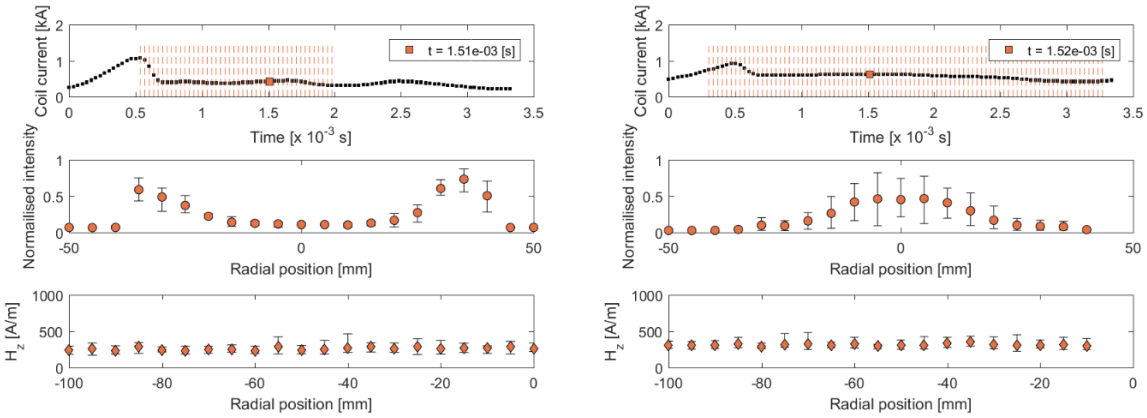

Figure B.6: Low inductive (left) and high inductive (right) discharges, t = 1.5 ms

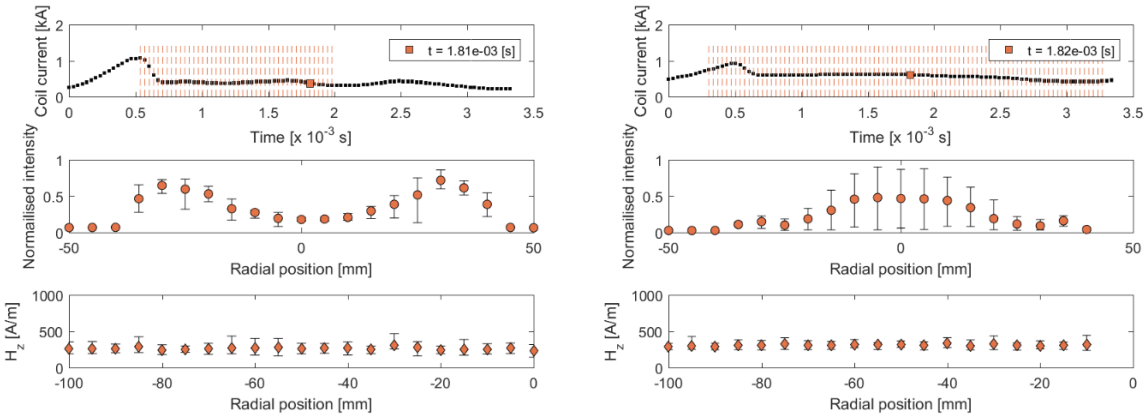

Figure B.7: Low inductive (left) and high inductive (right) discharges, t = 1.8 ms

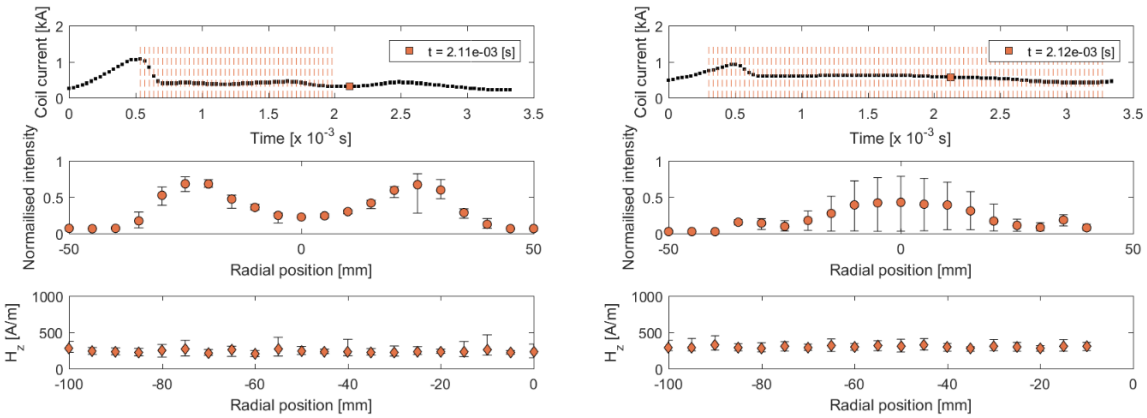

Figure B.8: Low inductive (left) and high inductive (right) discharges, t = 2.1 ms

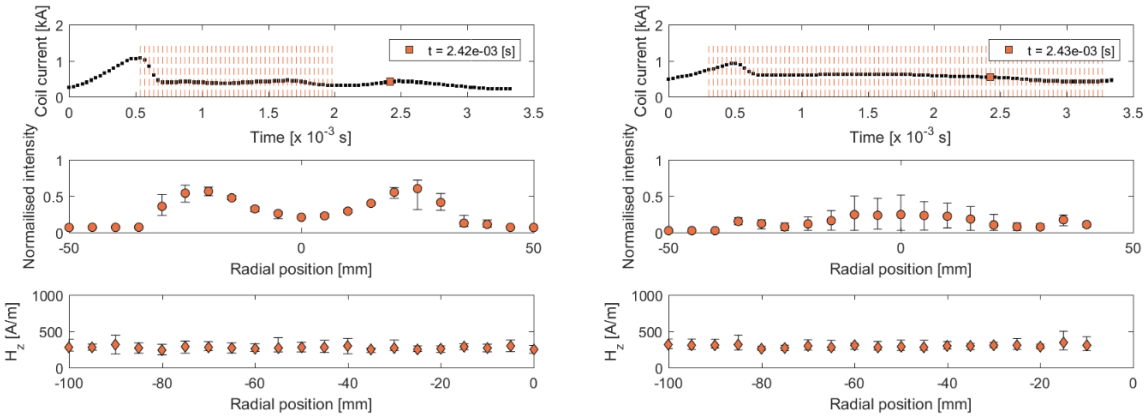

Figure B.9: Low inductive (left) and high inductive (right) discharges, t = 2.4 ms

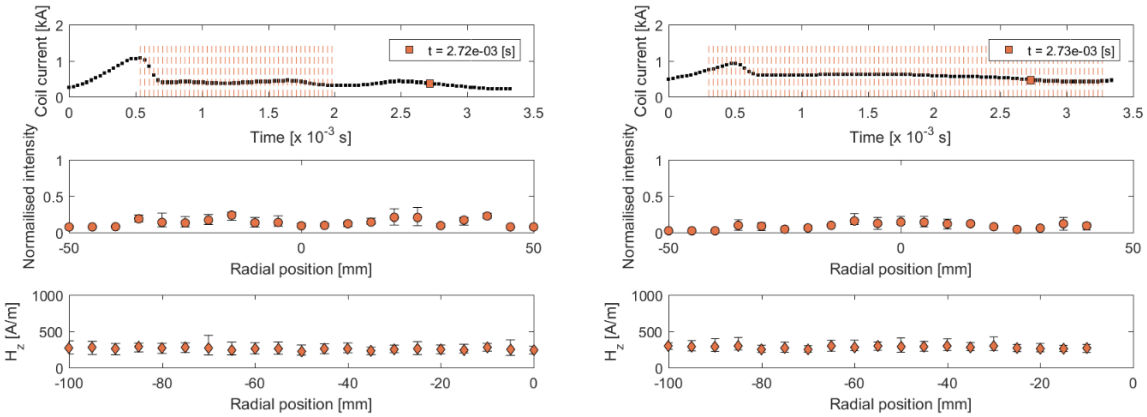

Figure B.10: Low inductive (left) and high inductive (right) discharges, t = 2.7 ms

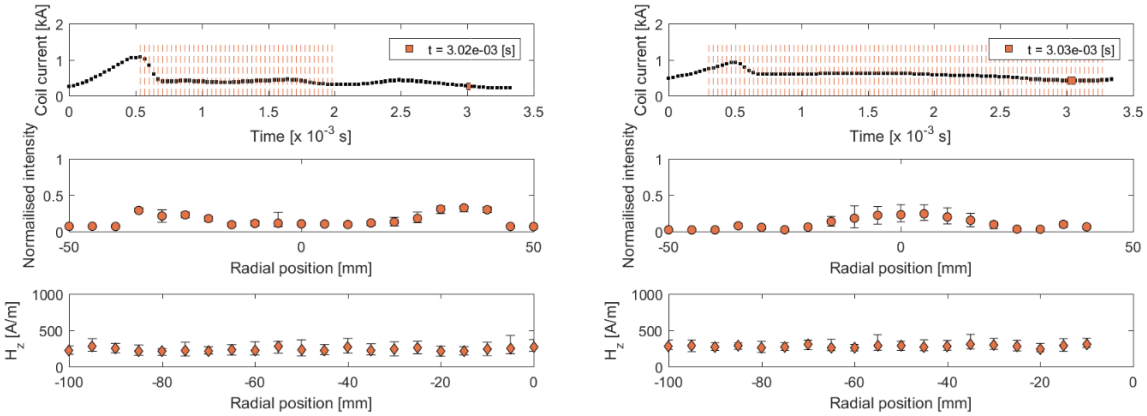

Figure B.11: Low inductive (left) and high inductive (right) discharges, t = 3.0 ms

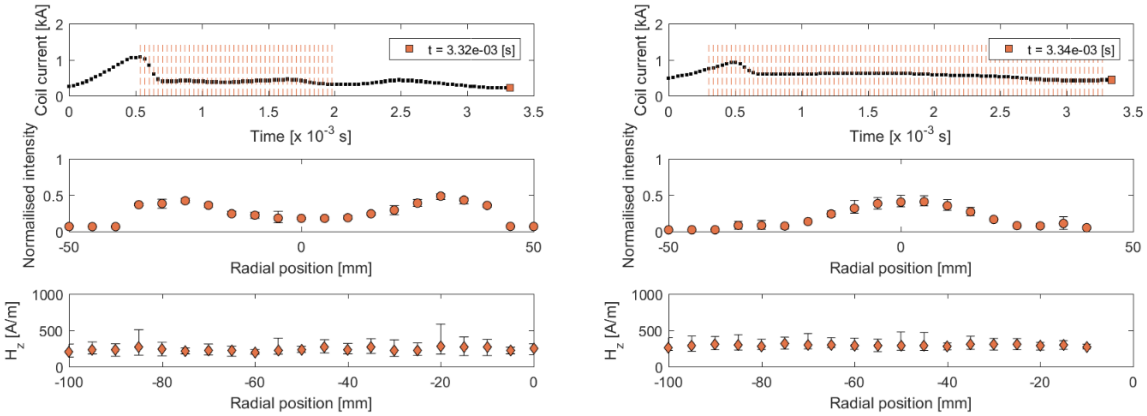

Figure B.12: Low inductive (left) and high inductive (right) discharges, t = 3.3 ms

Bibliography

[1] Sutton, G. P. and Biblarz, O., *Rocket Propulsion Elements*, John Wiley and Sons, Inc, 2010.

[2] Martinez-Sanchez, M. and Pollard, J. E., "Spacecraft Electric Propulsion-An Overview," *Journal of Propulsion and Power*, Vol. 14, No. 5, Sept. 1998, pp. 688–699.

[3] Goebel, D. M. and Katz, I., *Fundamentals of Electric Propulsion: Ion and Hall Thrusters*, NASA JPL, 2008.

[4] Dressler, R. A., Chiu, Y. H., and Levandier, D. J., "Propellant Alternatives for Ion and Hall Effect Thrusters," *AIAA 38th Aerospace Sciences Meeting & Exhibit*, January 2000.

[5] Nishiyama, K., "Air Breathing Ion Engine Concept," *54th International Astronautical Congress*, October 2003.

[6] Cifali, G., Misuri, T., Rossetti, P., Andrenucci, M., Valentian, D., Feili, D., and Lotz, B., "Experimental characterisation of HET and RIT with atmospheric propellants," *32nd International Electric Propulsion Conference*, September 2011, IEPC-2011-224.

[7] Frisbee, R. H., Polk, J. E., Gallimore, A. D., and Marrsee, C. M., "Oxygen-Propellant Plasma Thrusters for Cis-Lunar Electric Propulsion Missions," *34th AIAA/ASME/SAE/ASEE Joint Propulsion Conference and Exhibit*, July 1998.

[8] Pekker, L. and Keidar, M., "Analysis of Airbreathing Hall Effect Thrusters," *Journal of Propulsion and Power*, 2012.

[9] Hohman, K., "Atmospheric Breathing Electric Thruster for Planetary Exploration," Final report Grant no. NNX11AR29G, Busek Space Propulsion, 2012.

[10] Shabshelowitz, A., *Study of RF Plasma Technology Applied to Air-Breathing Electric Propulsion*, Ph.D. thesis, University of Michigan, 2013.

[11] Uematsu, K., Morimoto, S., and Kuriki, K., "MPD Thruster Performance with Various Propellants," *Journal of Spacecraft*, Vol. 22, No. 4, 1984, pp. 412 – 416.

[12] Hou, L., Shen, Y., Tang, H., and Zhao, W., "Improvement on Stability of Water Arcjet," *IEEE Transactions on Plasma Science*, Vol. 39, No. 1, 2011, pp. 608 – 614.

[13] Shiraki, S., Fukutome, Y., Inoue, F., Matsumoto, K., Tahara, H., Nogawa, Y., and Momozawa, A., "Performance Characteristics of Low-Power Arcjet Thruster Systems with Gas Generators for Water," *34th Internation Electric Propulsion Conference*, 2015, IEPC-2015-230.

[14] Yanagida, N., Ohata, M., Horisawa, H., and Kobayashi, A., "An Al-water Fed DC Arcjet," *34th International Electric Propulsion Conference*, 2015, IEPC-2015-232.

[15] Charles, C., Boswell, R. W., Laine, R., and MacLellan, P., "An experimental investigation of alternative propellants for the helicon double layer thruster," *Journal of Physics D: Applied Physics*, Vol. 41, 2008, pp. 175213.

[16] McElroy, M. B., Kong, T. Y., and Yung, Y. L., "Photochemistry and Evolution of Mars' Atmosphere: A Viking Perspective," *Journal of Geophysical Research*, Vol. 82, No. 28, 1977, pp. 4379–4388.

[17] Yelle, R. V., Strobell, D. F., Lellouch, E., and Gautier, D., "Engineering Models for Titan's Atmosphere," *Huygens: Science, Payload and Mission*, edited by A. Wilson, Vol. 1177 of *ESA Special Publication*, Euopean Space Agency, 1997, pp. 243–256, Provided by the SAO/NASA Astrophysics Data System.

[18] Muscatello, A. C. and Santiago-Maldonado, E., "Mars In Situ Resource Utilization Technology Evaluation," *50th AIAA Aerospace Sciences Meeting*, Nashville, Tennessee, January 2012.

[19] Simon, T. and Sacksteder, K., "NASA In-Situ Resource Utilization (ISRU) Development and Incorporation Plans," *Technology Exchange Conference*, Galveston, Texas, November 2007.

[20] Piccolo, F., "Exploration of Lunar resources: ISRU and oxygen production," *9th ILEWG Lunar Conference*, Sorrento, Italy, October 2007.

[21] Barnett, J. J. and Chandra, S., "COSPAR International Reference Atmosphere," Tech. rep., Committee on Space Research, 2012.

[22] Kumar, S., "The SO2 Atmosphere and Ionosphere of Io: Ion Chemistry, Atmospheric Escape, and Models Corresponding to the Pioneer 10 Radio Occultation Measurements," *Icarus*, Vol. 61, September 1985, pp. 101–123.

[23] Liang, M. C., Lane, B. F., Pappalardo, R. T., Allen, M., and Yung, Y. L., "Atmosphere of Callisto," *Journal of Geophysical Research*, Vol. 110, 2005.

[24] NASA, "Solar System Exploration," website, 2014, solarsystem.nasa.gov/planets [23.07.2013].

[25] Shematovich, V. I., Johnson, R. E., Cooper, J. F., and Wong, M. C., "Surface-Bound Atmosphere of Europa," *Icarus*, Vol. 173, 2005, pp. 480–498.

[26] Sittler, E. C., Johnson, R. E., Jurac, S., Richardson, J. D., McGrath, M., Crary, F., Young, D. T., and Nordholt, J. E., "Pickup Ions at Dione and Enceladus: Cassini Plasma Spectrometer Simulations," *Journal of Geophysical Research*, Vol. 109, 2004.

[27] Teolis, B. D., Jones, G. H., Miles, P. F., Tokar, R. L., Magee, B. A., Waite, J. H., Roussos, E., Young, R. T., Crary, F. J., Coates, A. J., Johnson, R. E., Tseng, W. L., and Baragiola, R. A., "Cassini Finds an Oxygen-Carbon Dioxide Atmosphere at Saturn's Icy Moon Rhea," *Science*, Vol. 330, 2010, pp. 1813 – 1815.

[28] Cruikshank, D. P., Brown, R. H., and Clark, R. N., "Nitrogen on Triton," *Icarus*, Vol. 58, 1984, pp. 293 – 305.

[29] Lellouch, E., Blanc, M., Oukbir, J., and Longaretti, P. Y., "A Model of Triton's Atmosphere and Ionosphere," *Advanced Space Research*, Vol. 12, No. 11, 1992, pp. 113 – 121.

[30] Yung, Y. L. and McElroy, M. B., "Stability of an Oxygen Atmosphere on Ganymede," *Icarus*, Vol. 30, 1977, pp. 97–103.

[31] Rapp, D., *Human Missions to Mars*, Praxis Publishing, Chichester, UK, 1st ed., 2007.

[32] Sanders, G. B., "ISRU: An Overview of NASA's Current Development Activities and Long-Term Goals," *38th Aerospace Sciences Meeting and Exhibit*, Reno, NV, January 2000.

[33] DiCara, D., del Amo, J. G., Santovincenzo, A., Carnicero-Dominquez, B., Arcioni, M., Caldwell, A., and Roma, I., "RAM Electric Propulsion for Low Earth Orbit Operation: an ESA Study," *30th International Electric Propulsion Conference*, 2007, IEPC-2007-162.

[34] Sentman, L. H., "Free Molecule Flow Theory and its Application to the Determination of Aerodynamic Forces," Tech. rep., Lockheed Missiles and Space Company, 1961.

[35] Accettura, A. G., Bruno, C., Casotto, S., and Marzari, F., "Mission to Mars using integrated propulsion concepts: considerations, opportunities, and strategies," *Acta Astronautica*, Vol. 54, No. 7, 2004, pp. 471 – 486.

[36] Junaedi, C., Hawley, K., Walsh, D., Roychoudhury, S., Abney, M. B., and Perry, J. L., "Compact and Lightweight Sabatier Reactor for Carbon Dioxide Reduction," *41st International Conference on Environmental Systems*, Portland, Oregon, July 2011, AIAA 2011-5033.

[37] Choueiri, E. Y., "A Critical History of Electric Propulsion: The First 50 Years (1906-1956)," *Journal of Propulsion and Power*, Vol. 20, 2004, pp. 193–203.

[38] JPL, "Electric Propulsion Multimedia," website, 2016, http://sec353ext.jpl.nasa.gov/ep/ multimedia.html [04.08.2016].

[39] Reid, B. M., *The Influence of Neutral Flow Rate in the Operation of Hall Thrusters*, Ph.D. thesis, University of Michigan, 2009.

[40] Tajmar, M., Genovese, A., and Steiger, W., "Indium Field Emission Electric Propulsion Microthruster Experimental Characterization," *Journal of Propulsion and Power*, Vol. 20, No. 2, April 2004, pp. 211–218.

[41] Boxberger, A. and Herdrich, G., "Experimental Test Campaign of Gas-fed Steady State Applied-Field Magnetoplasmadynamic Thruster SX3," *33rd International Electric Propulsion Conference*, 2013, IEPC-2013-251.

[42] Myers, R. M., "Applied-Field MPD Thruster Performance with Hydrogen and Argon Propellants," *Journal of Propulsion*, Vol. 9, No. 5, 1993, pp. 781 – 784.

[43] Auweter-Kurtz, M., Herdrich, G., Laure, S., and Wagner, H., "Plasma source development for technical applications at IRS," *Vacuum*, Vol. 73, 2004, pp. 309 – 316.

[44] Ducati, A. C., Giannini, G. M., and Muehlberger, E., "Experimental results in high-specific-impulse thermoionic acceleration," *AIAA Journal*, Vol. 2, No. 8, 1964, pp. 1452–1454.

[45] Lieberman, M. and Lichtenberg, A., *Principles of Plasma Discharges and Materials Processing*, John Wiley and Sons, Inc, Hoboken, New Jersey, 2nd ed., 2005.

[46] Harding, G. N. and Thonemann, P. C., "A study of helicon waves in indium," *Proceedings of the Physical Society*, Vol. 85, No. 2, 1965, pp. 317 – 328.

[47] Boswell, R. W., "Very efficient plasma generation by whistler waves near the lower hybrid frequency," *Plasma Physics and Controlled Fusion*, Vol. 26, No. 10, 1984, pp. 1147 – 1162.

[48] Charles, C. and Boswell, R. W., "Current-free double-layer formation in a high-density helicon discharge," *Applied Physics Letters*, Vol. 82, No. 9, 2003, pp. 1356 – 1358.

[49] Harle, T., Pottinger, S. J., and Lappas, V. J., "Helicon double layer thruster operation in a low magnetic field mode," *Plasma Sources Science and Technology*, Vol. 22, No. 1, 2013, pp. 015015.

[50] Herdrich, G., *Construction, Qualification and Characterisation of an Inductively Heated Plasma Wind Tunnel for Atmospheric Reentry Simulation (German)*, Ph.D. thesis, Institute for Space Systems, University of Stuttgart, 2004.

[51] Haines, M. G., "A review of the dense Z-pinch," *Plasma Physics and Controlled Fusion*, Vol. 53, No. 9, 2011.

[52] Blackstock, A. W., Fradkin, D. B., Liewer, K. W., Roehling, D. J., Stratton, T. F., and Williams, M., "Experiments using a 25-kw hollow cathode lithium vapor MPD arcjet," *AIAA Journal*, Vol. 8, No. 5, 1970, pp. 886–894.

[53] Sovey, J. S., Rawlin, V. K., and Patterson, M. J., "Ion Propulsion Development Projects in U.S.: Space Electric Rocket Test I to Deep Space 1," *Journal of Propulsion and Power*, Vol. 17, No. 3, May 2001, pp. 517–526.

[54] Beattie, J. R. and Matossian, J. N., "Mercury ion thruster technology," Tech. rep., NASA Hughes Research Labs, 1989.

[55] Ramsey, W. D., "12-cm Magneto-Electrostatic Containment Mercury Ion Thruster Development," *Journal of Spacecraft and Rockets*, Vol. 9, No. 5, May 1972, pp. 318–321.

[56] Nishiyama, K. and Kuninaka, H., "Discussion on Performance History and Operations of Hayabusa Ion Engines," *Transactions of the Japan Society for Aeronautical and Space Sciences, Aerospace Technology Japan*, Vol. 10, No. ists 28, 2012.

[57] del Amo, J. A. G., "Review of ESA Experimental Research Activities for Electric Propulsion," Tech. rep., NATO Research and Technology Organisation, 2011.

[58] Mercer, C. R., Mcguire, M. L., Oleson, S. R., and Barrett, M. J., "Solar Electric Propulsion Concepts for Human Space Exploration," *AIAA Space 2015*, No. AIAA-2015-4521, 2015.

[59] Boehrk, H., *For Inductive Re-Heating of a Supersonic Plasma Flow (German)*, Ph.D. thesis, Institute for Space Systems, University of Stuttgart, Stuttgart, Germany, May 2009.

[60] Chen, F. F., "Physics of helicon discharges," *Plasma Physics*, Vol. 3, No. 5, 1996, pp. 1783 – 1793.

[61] Klozenberg, J. P., McNamara, B., and Thonemann, P. C., "The dispersion and attenuation of helicon waves in a uniform cylindrical plasma," *Journal of Fluid Mechanics*, Vol. 21, No. 3, 1965, pp. 545 – 563.

[62] Endlich, P., *Experimental Simulation of Spacecraft Entry into the Matian Atmosphere (German)*, Ph.D. thesis, Institute for Space Systems, University of Stuttgart, 2009.

[63] Marynowski, T., Loehle, S., and Fasoulas, S., "Two-Photon Absorption Laser-Induced Fluorescence Investigation of CO2 Plasmas for Mars Entry," *Journal of Thermophysics and Heat Transfer*, 2014.

[64] Longmier, B. W., III, E. A. B., Carter, M. D., Cassady, L. D., Chancery, W. J., Diaz, F. R. C., Glover, T. W., Hershkowitz, N., Ilin, A. V., McCaskill, G. E., Olsen, C. S., and Squire, J. P., "Ambipolar ion acceleration in an expanding magnetic nozzle," *Plasma Sources Science and Technology*, Vol. 20, No. 1, 2011.

[65] Nawaz, A. and Herdrich, G., "Impact of Plasma Tube Wall Thickness on Power Coupling in ICP Sources," *Plasma Sources Science and Technology*, Vol. 18, 2009.

[66] Virko, V. F., Virko, Y. V., Slobodyan, V. M., and Shamrai, K. P., "The effect of magnetic configuration on ion acceleration from a compact helicon source with permanent magnets," *Plasma Sources Science and Technology*, Vol. 19, No. 1, 2010, pp. 015004.

[67] Chen, F. F., "Experiments on helicon plasma sources," *Journal of Vacuum Science & Technology A*, Vol. 10, No. 4, 1992, pp. 1389 – 1401.

[68] Celik, Y., Crintea, D. L., Luggenhoelscher, D., Czarnetzki, U., Ishijima, T., and Sugai, H., "Wave propagation and noncollisional heating in neutral loop and helicon discharges," *Physics of Plasmas*, Vol. 18, 2011.

[69] Blackwell, D. D. and Chen, F. F., "Two-dimensional imaging of a helicon discharge," *Plasma Sources Science and Technology*, Vol. 6, No. 4, 1997, pp. 569 – 576.

[70] Kortshagen, U., Gibson, N. D., and Lawler, J. E., "On the E-H mode transition in RF Inductive discharges," *Journal of Physics D: Applied Physics*, Vol. 29, No. 5, 1996, pp. 1224 – 1236.

[71] Abdel-Rahman, M., von der Gathen, V. S., and Gans, T., "Transition phenomena in a radio-frequency inductively coupled plasma," *Journal of Physics D: Applied Physics*, Vol. 40, No. 6, 2007, pp. 1678 – 1683.

[72] Norlen, G. and NIST ASD Team, "NIST Atmoic Spectra Database (version 5.3) - Ar I," Tech. rep., National Institute of Standards and Technology, Gaithersburg, MD, 1973, http://physics.nist.gov/cgi-bin/ASD/lines1.pl [01.08.2016].

[73] Whaling, W., Anderson, W. H. C., Carle, M. T., Brault, J. W., Zarem, H. A., and NIST ASD Team, "NIST Atmoic Spectra Database (version 5.3) - Ar II," Tech. rep., National Institute of Standards and Technology, Gaithersburg, MD, 1995, http://physics.nist.gov/cgi-bin/ASD/lines1.pl [01.08.2016].

[74] Moore, C. E. and NIST ASD Team, "NIST Atmoic Spectra Database (version 5.3) - N I," Tech. rep., National Institute of Standards and Technology, Gaithersburg, MD, 1975, http://physics.nist.gov/cgi-bin/ASD/lines1.pl [01.08.2016].

[75] Moore, C. E. and NIST ASD Team, "NIST Atmoic Spectra Database (version 5.3) - N II," Tech. rep., Gaithersburg, MD, 1976, http://physics.nist.gov/cgi-bin/ASD/lines1.pl [01.08.2016].

[76] Wenaker, I. and NIST ASD Team, "NIST Atmoic Spectra Database (version 5.3) - O I," Tech. rep., National Institute for Standards and Technology, Gaithersburg, MD, 1990, http://physics.nist.gov/cgi-bin/ASD/lines1.pl [01.08.2016].

[77] Amorim, J., Maciel, H. S., and Sudano, J. P., "High-density plasma mode of an inductively coupled radio frequency discharge," *Journal of Vacuum Science & Technology B*, Vol. 9, No. 2, 1991, pp. 362 – 365.

[78] Bronkhorst High-Tech B. V., *Datasheet F-202AV Mass Flow Controller for Gases*, 2015, Technical manual.

[79] Bronkhorst High-Tech B. V., *Datasheet F-203AV Mass Flow Controller for Gases*, 2015, Technical manual.

[80] Pfeiffer Vacuum, *Compact FullRange Gauge*, April 2008, Technical manual.

[81] MKS Instruments, *MKS Baratron Type 622B/623B/626B Absolute Pressure Transducers*, March 2013, Technical manual.

[82] Fritz Duesseldorf GmbH, *Technical Specification of the RF-Capacitors and the Triode RS 3300 CJ of the PWK3-IPG Energy Supply (German)*, 1997.

[83] Schoenherr, T., Komurasaki, K., Romano, F., Massuti-Ballester, B., and Herdrich, G., "Analysis of Atmosphere-Breathing Electric Propulsion," *IEEE Transactions on Plasma Science*, Vol. 43, No. 1, 2015, pp. 287–294.

[84] Romano, F., Massuti-Ballester, B., Schoenherr, T., and Herdrich, G., "System Analysis and Test Bed for an Air-Breathing Electric Propulsion System," *5th RGCEP - Russian-German Conference on Electric Propulsion and their Applications*, Dresden, Germany, September 2014.

[85] Romano, F., Binder, T., Herdrich, G., Fasoulas, S., and Schoenherr, T., "Air-Intake Design Investigation for an Air-Breathing Electric Propulsion System," *34th IEPC - International Electric Propulsion Conference*, Kobe, Japan, October 2015.

[86] Schwarz, S. E. and Oldham, W. G., *Electrical Engineering: An Introduction*, Rinehart & WInston, 1984.

[87] Hopwood, J., "Review of inductively coupled plasmas for plasma processing," *Plasma Sources Science and Technology*, Vol. 1, 1992, pp. 109 – 116.

[88] Lho, T., Hershkowitz, N., Miller, J., Steer, W., and Kim, G. H., "Azimuthally Symmetric Pseudosurface and Helicon Wave Propogation in an Inductively Coupled Plasma at Low Magnetic Field," *Physics of Plasmas*, Vol. 5, No. 9, May 1998, pp. 3135 – 3142.

[89] Association of German Engineers, *VDI - Heat Transfer Technical Handbook (German)*, Springer, Duesseldorf, Germany, 2013.

[90] Chadwick, A. R., Herdrich, G., Kim, M., Dally, B., and Hertel, J., "Impact of Dielectric Separation on Transition Point and Accessible Flow Enthalpy of Inductive Plasmas," *Space Propulsion 2016*, 2016, 3125078.

[91] Janocha, T., *Wall temperature measurements in an inductively heated plasma generator (German)*, Master's thesis, Institute for Space Systems, University of Stuttgart, 2015.

[92] "Ultra Precise RTD Sensors for Industrial Applications," website, 2016.

[93] Tempil, 2901 Hamilton Boulevard, South Plainfield, New Jersey, *Thermax ® Irreversible Temperature Recording Strips*, 2016.

[94] Kager GmbH, *TMC Temperature Indicators (German)*, 2016.

[95] Boehrk, H. and Auweter-Kurtz, M., "Thrust Measurement of the Hybrid Electric Thruster TIHTUS by a Baffle Plate," *Journal of Propulsion and Power*, Vol. 25, No. 3, May-June 2009, pp. 729–736.

[96] ME-Messsysteme GmbH, *KD40s Force Sensor*, 2017, Technical manual.

[97] Karrer, N., Hofer-Noser, P., Herdrich, G., and Auweter-Kurtz, M., "Isolated Current Probe for Continuous Monitoring of AC Currents of High Amplitude and High Frequency," *European Power Electronics Conference*, France, September 2003.

[98] Thorlabs GmbH, *DET210 - High-speed Silicon Detector*, Newton, NJ, 2005, Rev E.

[99] Projekt Elektronic GmbH, *Teslameter FM 302 for AS-active-probes*, Berlin, Germany, 2016.

[100] Bakshi, U. A. and Bakshi, A. V., *Electromagnetic Fields*, Technical Publications, 2008.

[101] Rection Design, San Diego, *CHEMKIN 10112*, 2011.

[102] Bauder, U., Majid, A., Fertig, M., and Auweter-Kurtz, M., "Improvement and Extension of the Loosely Coupled Navier-Stokes Code SINA to Different Gases," *10th AIAA/ASME Joint Thermophysics and Heat Transfer Conference*, 2010, AIAA-2010-4518.

[103] Bauder, U., Herdrich, G., Fasoulas, S., and Auweter-Kurtz, M., "Modeling of a DC-RF PlasmathPlasma with the Navier-Stokes Code SINA," *33rd International Electric Propulsion Conference*, 2013, IEPC-2013-324.

[104] McBride, B. J., Gordon, S., and Reno, M. A., "Coefficients for Calculating Thermodynamic and Transport Properties of Individual Species," Tech. rep., NASA, 1993.

[105] Go, D. B., "Intermediate Heat Transfer - Course Notes," University of Notre Dame.

[106] Devoto, R. S., "Transport coefficients of ionized argon," *The Physics of Fluids*, Vol. 16, No. 5, May 1973, pp. 616–623.

[107] Baeva, M., Kozakov, R., Gorchakov, S., and Uhrlandt, D., "Two-temperature chchemical non-equilibrium modeling of tratransfer arcs," *Plasma Sources Science and Technology*, Vol. 21, No. 5, 2012, pp. 1–13, doi:10.1088/0963-0252/21/5/055027.

[108] Stewart, I. M., *Experimental and Theoretical Studies of the Argon Pre-Breakdown Discharge*, Ph.D. thesis, University of New England, 1995.

[109] Min, T. T., *Computational Studies of Electron Transport and Reaction Rate MModel for Argon Plasma*, Ph.D. thesis, University of Texas at Austin, 2010.

[110] Gudmundsson, J. T., Alami, J., and Helmersson, U., "Spatial and temporal behavior of the plasma parameters in a pulsed magnetron discharge," *Surface and Coatings Technology*, Vol. 161, No. 2-3, 2002, pp. 249–256.

[111] Hagelaar, G. J. M. and Pitchford, L. C., "Solving the Boltzmann equation to obtain electron transport coefficients and rate coefficients for fluid models," *Plasma Sources Science and Technology*, Vol. 14, No. 4, 2005, pp. 722–733, doi:10.1088/0963-0252/14/4/011.

[112] Yamabe, C., Buckman, S. J., and Phelps, A. V., "Measurement of free-free emission form low-energy-electron collisions with Ar," *Physical Review A: Atomic, Molecular, and Optical Physics*, Vol. 27, No. 3, 1983, pp. 1345 – 1352.

[113] Jeffus, L., *Welding and Metal Fabrication*, Cengage Learning, 2011.

[114] Chadwick, A. R., Herdrich, G., Kim, M. K., and Dally, B., "Transient Electromagnetic Behaviour in Inductive Oxygen and Argon-Oxygen Plasmas," *Plasma Sources Science and Technology*, Vol. 25, No. 6, 2016, doi:10.1088/0963-0252/25/6/065025.

[115] Lenzner, S., *Numerical Analysis of Flow Phenomena in an Inductive Heated Plasma Sources (German)*, Ph.D. thesis, Institute for Space Systems, University of Stuttgart, 2000.

[116] Sleziona, C., *High Enthalpy Flows for Space Applications (German)*, Ph.D. thesis, Institute for Space Systems, University of Stuttgart, 1998.

[117] Linstrom, P. J. and Mallard, W. G., editors, *NIST Chemistry WebBook, NIST Standard Reference Database Number 69*, National Institute of Standards and Technology, Gaithersberg, MD, 2017, doi:10.18434/T4D303.

[118] Zakarian, A., "Bond Dissociation Energies," University of California Santa Barbara.

[119] "FLUIDAT," (online software), 2017.